TECHNISCHE UNIVERSITÄT WIEN

DISSERTATION

qBOUNCE : Ramsey Spectroscopy Using Gravitationally Bound Quantum States Of Neutrons

Ausgeführt zum Zwecke der Erlangung des akademischen Grades
eines Doktors der Naturwissenschaften
unter der Leitung von

Univ.Prof. Dipl.-Phys. Dr.rer.nat. Hartmut Abele
141
Atominstitut
unter Mitwirkung von
Dr. Tobias Jenke
vom Institut Laue-Langevin, Grenoble

eingereicht an der Technischen Universität Wien
Fakultät für Physik

von

Jakob Micko
1225153
Herbeckstraße 75/7/4 1180 Wien

May 15, 2023

Abstract

qBounce uses Ultra Cold Neutrons (UCNs) in a mechanical spectrometer using Ramseys method of separated oscillating fields to investigate gravity. The UCNs are trapped by gravity on the surface of mirrors leading to discrete quantum states. By oscillating the mirrors transitions between these states can be induced. Using this method, called Gravity Resonance Spectroscopy (GRS), measurements of the local acceleration for the bound neutron have been performed. This acceleration includes, in addition to gravity, all other interactions that influence the neutron inside the experiment. During this PhD the acceleration of the Earth was determined with the relative precision of $\delta g/g \approx 1 \cdot 10^{-5}$. The improvement from the previous best GRS measurement with the Rabi method gives $\sigma g_{\mathrm{Rabi}}/\sigma g_{\mathrm{Ramsey}} \approx 42$. For the transition $|1\rangle \rightarrow |6\rangle$ the absolute energy resolution of $\Delta E \approx 2.6 \times 10^{-16}\,\mathrm{eV}$ was measured with qBOUNCE with unprecedented precision. A measurement using a spin dependent detector could show that neutrons with the spin parallel and anti parallel to g have the same acceleration with a relative precision of $\delta g/g \approx 6.3 \cdot 10^{-4}$. An offset from the expected value of g determined by a falling corner cube measurement of $(g_{\mathrm{measured}} - g_{\mathrm{cornercube}})/\sigma = 7.43$ was found and an in depth analysis of systematic effects was performed, inlcuding numerical simulations. The neutron represents an almost ideal test mass, has no charge and a low polarizability when compared to also neutral atoms. This limits the influence of Van der Waals forces on the bound states. The experiment is located and has been performed at the PF2 beamline at the Institut Laue-Langevin in Grenoble and after 2018, where the first proof of principle of this Ramsey type GRS was published, this thesis was performed.

Abstract

qBounce verwendet Ultra Cold Neutrons (UCNs) in einem mechanischen Spektrometer, wobei "Ramseys method of separated oscillating fields" verwendet wird um Gravitation zu untersuchen. Die UCNs sind durch Gravitation auf der Oberfläche von Neutronenspielgeln gebunden, was zu diskreten Quantenzuständen führt. Durch die mechanische Oszillation der Spiegel können Übergänge zwischen den Zuständen angeregt werden. Mithilfe dieser Methode, die "Gravity Resonance Spectroscopy" (GRS) genannt wird, wurden Messungen der lokalen Beschleunigung des gebundenen Neutrons. Diese Beschleunigung inkludiert neben Gravitation alle anderen Wechselwirkungen, die das Neutron im Experiment beeinflussen. Im Rahmen dieser Doktorarbeite wurde die Erdbeschleunigung mit einer relativen Genauigkeit von $\delta g/g \approx 1 \cdot 10^{-5}$ gemessen. Die Verbesserung des statistischen Messfehlers im Vergleich zu vorherigen GRS Messungen, die Rabis Methode verwendet haben, ist $\sigma g_{\mathrm{Rabi}}/\sigma g_{\mathrm{Ramsey}} \approx 42$. Der Übergang $|1\rangle \rightarrow |6\rangle$ wurde mit einer noch nicht erreichten absoluten Energieauflösung von $\Delta E \approx 2.6 \times 10^{-16}\,\mathrm{eV}$ mit qBOUNCE gemessen. Eine Messung mit einem Spin abhängigem Detektor konnte zeigen, dass Neutronen, deren Spin parallel bzw. antiparallel zur Erdbeschleunigung g ausgerichtet ist, mit einer relativen Genauigkeit $\delta g/g \approx 6.3 \cdot 10^{-4}$ die selbe Beschleunigung erfahren. Eine Abweichung vom erwarteten Wert von g, der mithilfe einer "falling cornercube" Messung bestimmt wurde, $(g_{\mathrm{measured}} - g_{\mathrm{cornercube}})/\sigma = 7.43$ konnte gefunden werden, und eine detaillierte Analyse der Systematischen Effekte, auch mithilfe numerischer Simulationen, wurde durchgeführt. Das Neutron ist eine fast ideale Testmasse, es hat keine Ladung und eine niedrige elektrische Polarisierbarkeit im Vergleich zu ebenso ungeladenen Atomen. Das limitiert den Einfluss von Van der Waals Kräften auf die gebundenen Zustände. Das Experiment befindet sich am PF2 Strahlplatz am Institut Laue-Langevin in Grenoble und diese Doktorarbeit wurde, nach der ersten Machbarkeitsstudie der Ramsey GRS Methode 2018, durchgeführt.

Contents

Chapter 1

Introduction

In the beginning of the 20th century the foundations of quantum mechanics were laid out by Planck's explanation of black body radiation. The following advances in the theoretical description of the behaviour of microscopic particles and how to interpret these led to a paradigm shift in the understanding of the physical world. Especially the statistical nature of the microscopic world was a surprise. Nevertheless this statistical interpretation remains until today. The success of non relativistic quantum theory of Schrödinger and the work done by Dirac extending the formalism to relativistic particles managed to describe a staggering amount elementary phenomena.

Investigating these effects led to technological improvements giving rise to ever more precise measurements feeding into the refinement of the theory. Subsequently many experiments could, in one way or another, be explained by using the methods of quantum mechanics. The description of particle systems and electromagnetism as quantum fields solidified the fundamental understanding of the quantum world. This culminated in the quantum field theory of Quantum Electrodynamics and later in the Standard Model. The modern understanding of the fundamental particles observed in the Universe has been shaped by the historical success of these theories.

The Standard Model incorporates three of the four known fundamental interactions and describes the microscopic world, the strong force, the weak force and the electromagnetic force and their interactions with matter. Using the methods of quantum field theory within this framework allows the description of all early experiments by fundamental interactions. After improvements in the theoretical tools most experimental results can be explained and the effective description of reality arising from the microscopic description is understood as an effective field theory. Especially the importance of symmetries in the microscopic world giving rise to effective macroscopic interactions has proven to be exceedingly powerful.

Concurrently Einstein's theory of general relativity was able to explain phenomena dominated by gravity that have been observed in astronomy. The rich history of this field was advanced to a point where minute discrepancies could be measured but not explained at the beginning of the 20th century. Famously the perihelion shift of mercury around the Sun could not be explained by Newtonian gravity. This effect remained after sophisticated perturbation techniques using Newtonian gravity were employed without much progress on an explanation. Einstein's general theory of relativity (GR) was able to provide an explanation of this effect. After the observation of the bending of light by the Sun GR was established as a reasonable candidate for a theory of gravity and further experimental confirmations were found. Cosmological observations made it clear that the history of the Universe as a whole and GR as a description of the fourth fundamental force was a valid description overall, albeit with minor caveats. From cosmological observations it was possible to deduce the mass distribution in galaxies and the Universe showing more mass present than can be accounted for by visible stars. Additionally around the turn of this century it was discovered that the expansion of the Universe is accelerating. This can be explained by a free parameter in the Einstein field equations of GR, that was historically controversial.

The invisible mass was named Dark Matter (DM) as a non luminous, massive component of the Universe, whereas the cosmological constant can be included in the total energy of the Universe and has been called Dark Energy (DE). The precise nature of these is unknown but large scale simulations matching these universal components to cosmological observations both in the Universe as a whole and

Table 1.1: UCN pseudo effective potential and cutoff velocities v_c for a few materials from [2].

Substance	U [neV]	v_c [m/s]
^{58}Ni	335	8
Ni	252	6.9
Be	252	6.9
C (graphite, 2.0 g/cm^3)	175	5.8
Cu	165	5.6
Stainless Steel	$\sim$188	$\sim$6.0
Float glass (boron free)	96	4.3
Al	54.1	3.22
H$_2$O (1.0 g/cm^3)	-14.6	-
Ti	-49.7	-

in smaller scale galaxies have been performed and can describe the observations.

Having a successful description of the microscopic world with the standard model and the whole Universe with GR, attempts to unify all four forces in one cohesive theory have been made but thus far inconclusive. In laboratory experiments the standard model alone has been able to describe almost all observations. Since the standard model has been so successful in describing nature in the past DM and DE are believed to also be described by some quantum field theory. In GR they are treated classically but since the gravitational interaction is extraordinarily weak the interactions with the standard model on a microscopic scale have thus far eluded experimentalists. From a theoretical point of view the flexibility of the tools available within quantum field theory should at least be able to describe some form of interaction of DM and DE with "normal" Standard Model matter. Finding quantum systems interacting gravitationally in a significant way has been a challenge in experiments in the past and no connection between gravitationally observed anomalies and quantum experiments has been found.

To investigate this intersection of gravity and quantum mechanics qBOUNCE uses a special type of neutron. In principle a neutron is a simple test particle: they carry no charge, have a very low electrical polarizability , thus being only weakly influenced by any kind of electromagnetic interaction, and crucially have mass.

Neutrons with a very low kinetic energy have a long wavelength and their interaction with matter can be described using an effective optical potential U [1]. The wavelength of these neutrons is much larger than the typical spacing of atoms in matter allowing this effective treatment of the microscopic neutron-nucleus interaction in extended systems. It turns out that most materials in nature have a positive potential so low energy neutrons are reflected on surfaces made of such materials. In tab. 1.1 from [2] an excerpt of a few materials and their corresponding potentials are listed. v_c determines the critical velocity for neutrons, below which all neutrons can be reflected from a surface made of this material since the kinetic energy is below the potential U of the material. Such neutrons are called ultra-cold neutrons (UCNs). They can be stored in material bottles which has been used for the most accurate lifetime measurements to date see the neutron in [3]. Also fundamental properties of the particle such as a hypothetical neutron electric dipole moment are investigated using UCNs.

Using a flat plane as a neutron mirror bound states are be formed on top of a surface: the neutron is reflected by the mirror and is trapped in the gravity potential of the Earth. After the discovery of such gravitationally bound states of neutrons in 2002 in [4] the usefulness of these states was quickly realised. The qBOUNCE collaboration took the view that excitations between gravity eigenstates of the UCNs on top of a mirror can be implemented by mechanically oscillating the mirror. Using this method to investigate gravity states has been termed Gravity Resonance Spectroscopy (GRS).

This was demonstrated in [5] with the experimental details in [6] and for the first time spectroscopic measurements using gravity bound quantum states were performed. The experiment was performed at the Institut Laue-Langevin in Grenoble, France. The source of neutrons is called PF2 and is the strongest continuous flux UCN source in the world. The main principle of the qBOUNCE experiment is as follows:

UCNs are bound on top of a mirror and a second glass plate is placed on top, called an absorber or scatterer. This second plate is made rough so that neutrons interacting with it are scattered, not strictly absorbed. This leads to a loss of neutrons that are close to the scatterer. Neutrons that have a higher energy are in excited states further away from the base mirror and are therefore more readily absorbed. This allows the selection of the ground state by placing the absorber at a height where all but the lowest state is absorbed. This is the same principle that was used in [4] to demonstrate the existence of gravity states. When this whole system is oscillated the neutrons in the ground state are excited to a higher state, which again has a higher probability to interact with the absorber and if an excitation is performed, the transmission of neutrons through the setup is reduced. The transferred energy is $\Delta E = 2\pi\hbar\nu$ where ν is the oscillation frequency of the mirror. By measuring the frequency dependent transmission the energies of the excited states can be inferred. By calculating the expected transition frequency and comparing that to the result from the experiment interactions of the neutron shifting this transition frequency can be checked. In [7] the result of this experiment was used to put limits on dark matter and dark energy scenarios. In general any theoretic model that predicts a shift of the bound states can be examined using GRS.

As an improvement of the sensitivity an upgrade of the system to use Rabis spectroscopic method was realised in 2012 by introducing two state selectors with an oscillating mirror in between. [8] This is completely analogous to Rabis method used in NMR, except that the excitation is completely mechanical and in no way electromagnetic. With this new and improved version new transitions were first observed and constraints on symmetron dark matter were published [9]. To further improve sensitivity the length of the Experiment could be increased. One drawback of Rabis method is the sensitivity to different interaction times. Since the length of the neutron mirror is constant, neutrons with different velocities have different interaction times and it turns out that the resolving power decreases drastically. Because of this the velocity spectrum had to be limited and only a fraction of the total UCN output of PF2 could be used. This low efficiency limits the ability to just increase the length of the setup, where the beam divergence lowers the countrate even more. To circumvent this, historically Rabis method was superseded by Ramseys method of separated oscillating fields for molecular beam NMR experiments. [10] Ramsey was able to show that using the method now named after him, the final result for the transition frequency is less perturbed by a large velocity spread. This has already been suggested in [11, 12] before Rabis method had been implemented with neutrons in qBOUNCE .

The extension of the experiment from the Rabi method to Ramseys method of separated oscillating fields made a complete overhaul of the experimental equipment necessary. After a successful commissioning in 2017 [13] a proof of principle of such GRS measurements using the Ramsey method was presented in 2019 [14]. Since then J. Bosina has performed measurements suggested in [15] to measure the charge of the neutron. After this my PhD work was funded by the ILL to perform high precision measurements using Ramsey's method of separated oscillating fields in the context of GRS to show the full potential of the qBOUNCE experiment in its current realisation and to investigate the future possibilities.

Chapter 2

Theoretical considerations
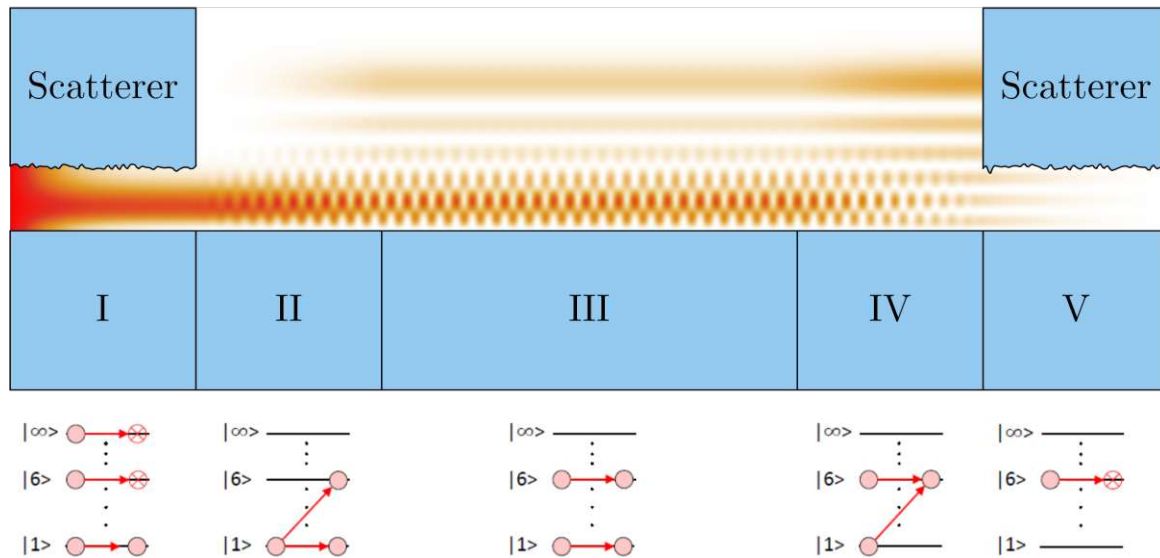
Figure 2.1: Simplified sketch of the qBOUNCE GRS setup. Neutrons enter from the left and exit on the right where a proportional counter tube is used as a detector. Higher neutron density here is shown in red. Sections I is a mirror with a scatterer on top preparing the initial state and V scatterers are placed to scatter neutrons that extend far above the mirror. These are the excited states and are scattered from the system. In section II the neutrons in the ground state (and a small number in the first two excited states) remain. Sections II and IV are the interaction regions and are oscillated at a specific frequency in order to induce a state transition. Here for the transition $|1\rangle \to |6\rangle$. Section III splits the two interaction region completing a basic Ramsey measurement scheme. The amplitude of the oscillations in sec. II and IV has to be tuned to produce a 50/50 superposition of the two contributing states in sec III. This is called a $\pi/2$ excitation. If the excitation in sec. IV is in phase with sec. II the neutrons get excited to the higher state and are scattered by the second scatterer, thus they can not reach the detector on the right. In the bottom a schematic overview of how the state population changes over the five sections making up the qBOUNCE experiment is shown. The red circles in the bottom signify populated states, the arrows transitions and the crossed circles indicate states that get scattered out of the system.

qBOUNCE uses the transmission of neutrons trough the experiment to infer the local value of the acceleration due to gravity. The schematic setup can be seen in fig. 2.1. The symbols in the bottom have the following meaning:

⬤	shows the existence of an occupied state
	multiple occupied states signify a superposition of different states
⊗	shows states that have been occupied but are lost due to scattering
⟶	highlights the evolution of state(s) within one section

The neutrons enter from the left and are shown in red/orange, where red signifies a high neutron density and white a low density. They move through the setup with a tangential velocity to the mirror surface somewhere in the interval $[4; 14]\mathrm{m\,s}^{-1}$. The specific velocity interval and its implications will be discussed in chapters 2.2, 3.3.4, 4.1.5, 4.2.3 and experimental measurements in chapter 5.3.1. The velocity normal to the mirror surface is $\approx 0\mathrm{m\,s}^{-1}$ after section I: any neutrons that have a vertical velocity component are scattered by the scatterer above section I, acting as a state selector. This is described in chapter 2.2. In section II the neutron mirror is oscillating, driving transitions between the bound neutron states, described in chapter 2.4. If the superposition after section II between the two involved states is 50/50, a so called $\pi/2$-flip was performed. Section III is not oscillating and the neutron is propagating without transitions taking place. Section IV is again oscillating and driving the transition again. If a second $\pi/2$ flip was performed the excitation is completed. Finally in section V the neutrons are again passing a mirror scatterer pair, acting as a final state selector.

After section V a neutron counter tube, described in 3.3.2, counts the neutrons passing through the whole assembly. Using this method of mechanically induced transitions of bound neutron states in a spectrometer has been termed Gravity Resonance Spectroscopy (GRS). Depending on the relative phase between section II and section IV, the oscillating sections, a different transmission pattern through the experiment can be observed. This is described in chapter 2.5. To determine the resonance frequency and thus the energy difference between states the transmission at different excitation frequencies and phase offsets between sections II and IV are used: At the frequency of the transition with 0 phase and at π and at the crossing points to left and right of the transition with 0 and π phase. The specific method used is outlined in chapter 2.6 can be seen in fig. 2.14. If the points measured are not centred in the middle of the transition, a characteristic shift of the points can be observed. Using this basic measurement principle, the transition frequencies between different eigenstates is determined which are directly related to the local acceleration due to gravity outlined in detail in the following chapters.

A discussion of systematic effects present in the experiment extending the basic theory outlined in this chapter is given below in chapter 4. Some analytical calculations not strictly necessary for the main points in this chapter are put in appendix A.

2.1   Bound states of neutrons in the gravity potential

In this chapter I will outline the derivation of the basic functions which describe the neutrons in the qBOUNCE experiment. The numerical values of the constants used throughout are given by

$$g = 9.804\,971\,61\,\text{m/s}^2 \text{ [16]}$$
$$\hbar = \frac{h}{2\pi} = \frac{6.626\,070\,15 \times 10^{-34}\,\text{J s}}{2\pi} \text{ [17]}$$
$$m_n = m_i = m_g = 1.674\,927\,498\,04 \times 10^{-27}\,\text{kg [17]}$$
$$e = 1.602\,176\,634 \times 10^{-19}\,\text{C [17]}$$

where g is the local effective acceleration of the Earth, $\hbar$ the reduced Planck constant, m_n, m_i and m_g are the neutron mass, the inertial and the gravitational neutron mass and e the elementary charge. These values are used for numerical definiteness here, errors to these quantities will be discussed later where applicable. In general any physical constant not appearing here has been taken to be the value from [17] unless otherwise stated. In principle m_i and m_g could be treated separately and this will be done as much as possible. When the neutron mass m_n appears the distinction is not important.

2.1.1   Solutions of the Schrödinger equation

The Schrödinger equation for a neutron in the gravity field on the surface of the Earth is given by

$$i\hbar \frac{\partial}{\partial t} \psi(x,y,z,t) = \left(-\frac{\hbar^2}{2m_i} \left(\frac{\partial^2}{\partial x^2} + \frac{\partial^2}{\partial y^2} + \frac{\partial^2}{\partial z^2} \right) + m_g g z + V(x,y,z,t) \right) \psi(x,y,z,t) , \quad (2.1)$$

where V is any additional potential not due to (linearised, Newtonian) gravity. From here on out the positive z-axis is anti parallel to gravity, the x-axis parallel to the neutron flight direction and the y-axis orthogonal to form a right handed coordinate system. If it is assumed that the potential $V(x,y,z,t) = V(z,t)$ then the neutron is unconstrained in the x and y directions and the solutions in these directions can be expanded in plane waves. After separating these out, the problem

$$i\hbar \frac{\partial}{\partial t} \psi(z,t) = \left(-\frac{\hbar^2}{2m_i} \frac{\partial^2}{\partial z^2} + m_g g z + V(z,t) \right) \psi(z,t) , \quad (2.2)$$

remains for the z direction. Introducing the characteristic quantities

$$z_0 = \sqrt[3]{\frac{\hbar^2}{2m_i m_g g}} \approx 5.869\,\mu\text{m} , \quad (2.3)$$

$$E_0 = \sqrt[3]{\frac{\hbar^2 m_g^2 g^2}{2m_i}} \approx 0.602\,\text{peV} , \quad (2.4)$$

$$t_0 = \sqrt[3]{\frac{2m_i \hbar}{m_g^2 g^2}} \approx 1.094\,\text{ms} , \quad (2.5)$$

can be used to simplify the differential equation to

$$it_0 \frac{\partial}{\partial t} \psi(z,t) = \left(-z_0^2 \frac{\partial^2}{\partial z^2} + \frac{z}{z_0} + \frac{V(z,t)}{E_0} \right) \psi(z,t) , \quad (2.6)$$

By introducing dimensionless variables via $t = t_0 t'$, $z = z_0 z'$, $V = E_0 V'$ the dimensionless Schrödinger equation reads

$$i \frac{\partial}{\partial t'} \psi(z',t') = \left(-\frac{\partial^2}{\partial z'^2} + z' + V'(z',t') \right) \psi(z',t') . \quad (2.7)$$
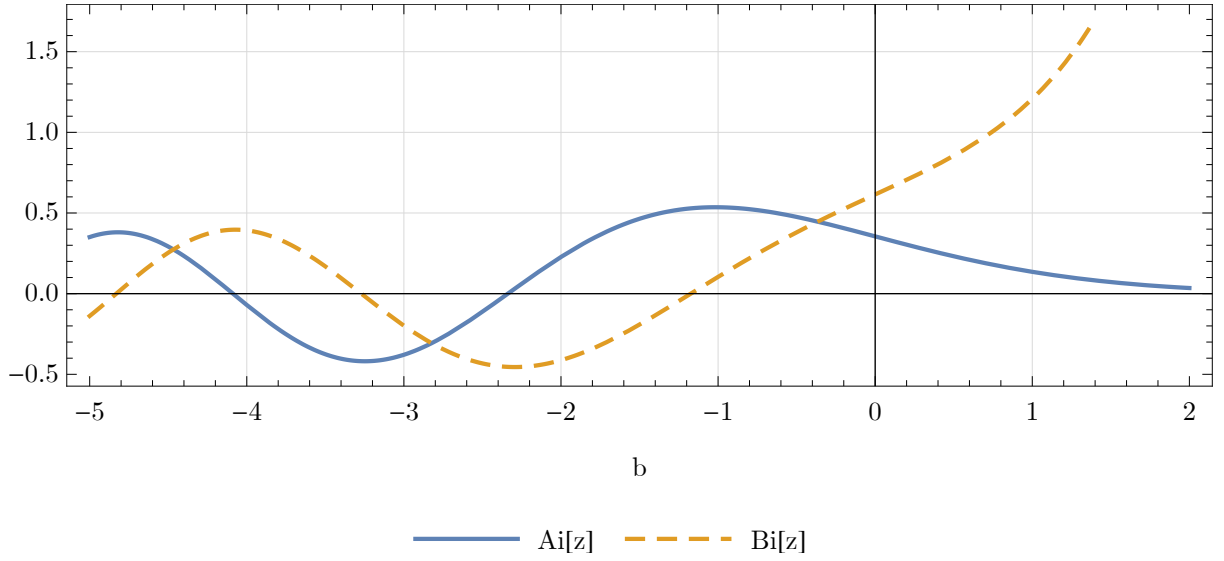
Figure 2.2: The two solutions to the Airy differential equation. Ai(z) converges whereas Bi(z) diverges as z increases to infinity.

For a neutron under the influence of only gravity $V(z, t) = 0 = V'(z, t)$ and the energy eigenfunctions can be found by solving the corresponding time independent Schrödinger equation (after rearranging)

$$
\begin{aligned}
\left(\frac{\partial^2}{\partial z'^2} - (z' - E') \right) \psi(z') &= 0 \,, \\
\hat{=} \left(\frac{\partial^2}{\partial z''^2} - z'' \right) \psi(z'') &= 0 \,,
\end{aligned}
\tag{2.8}
$$

where $z'' = z' - E'$. The second differential equation is known as the Airy equation and the solutions are well known in the literature. The two solutions are known as the Airy functions Ai and Bi. They can be seen in fig. 2.2.

The solution Ai(z) converges for $z \to \infty$ whereas Bi(z) diverges. The first equation is the Airy equation for a shifted argument. For a neutron falling under gravity without boundary condition at infinity only the solution Ai(z) describes bound states and is physically relevant. If the neutron is constrained at a finite position both solutions become relevant, for a discussion see [18].

2.1.2 Eigenenergies and transition frequencies

In the qBOUNCE experiment ultra-cold neutrons are bound on the surface of a (neutron) mirror with a potential $U \approx 100 \, \text{neV}$. As a first approximation, this can be implemented by assuming the neutron wave functions is finite above the mirror and 0 inside/below the mirror. For the mirror surface at $z = 0$ this means that the wave function $\psi(z \leq 0) = 0$ and the solutions are proportional to shifted Airy functions, such that the zeroes coincide with the mirror surface. From equation (2.8) the energy of the neutron can then be calculated.

In fig. 2.3 the first three of the shifted Airy Ai functions can be seen. Calling the n-th zero crossing $\text{AiZ}(n)$ defined by

$$
\text{Ai}\left(\text{AiZ}(n) \right) = 0 \,,
\tag{2.9}
$$

the wave function is given by $\psi_n(z') \sim \text{Ai}(z' + \text{AiZ}(n))$ up to normalisation N_n. From the shifted Airy
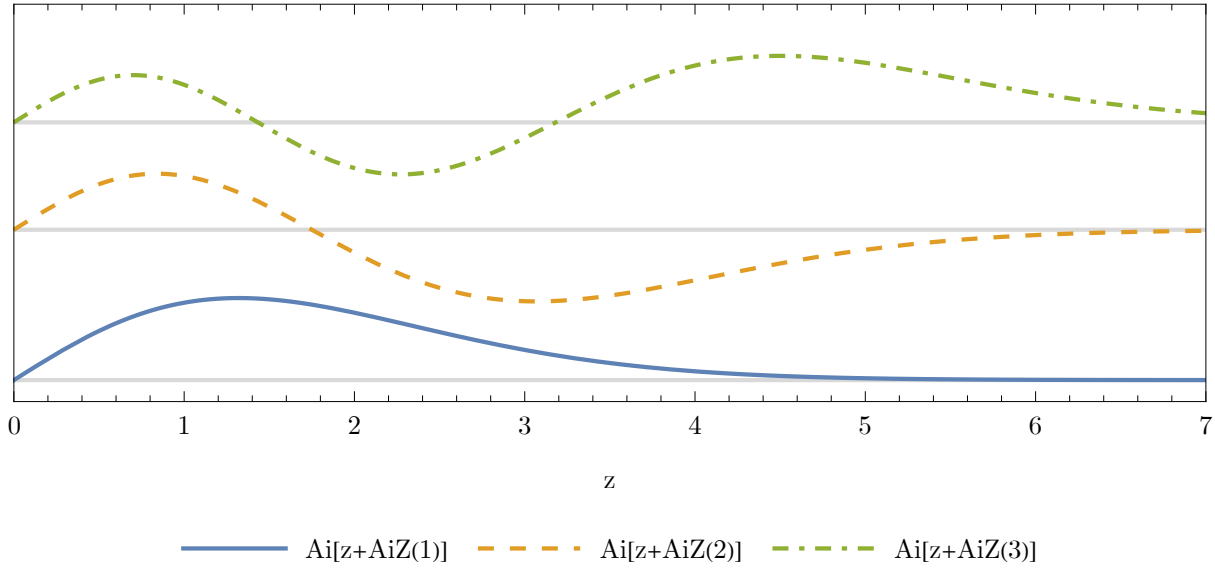
Figure 2.3: Eigenfunction of the Airy differential equation shifted, such that $\psi(0) = 0$.

equation

$$\left(\frac{\partial^2}{\partial z'^2} - (z' - E_n') \right) \psi_n(z') \sim \left(\text{AiZ}(n) + E_n' \right) \text{Ai}\left(z' + \text{AiZ}(n) \right) = 0 \, ,$$

$$E_n = E_0 E_n' = -E_0 \, \text{AiZ}(n) \, , \tag{2.10}$$

the numerical values for the first 10 energies are given in table 2.1 to the precision that is currently reached in the Ramsey experiment.

Table 2.1: Eigenenergies of the first 10 eigenstates. The energies are given to the decimal place needed for the current precision of qBOUNCE .

n	E_n [peV]	n	E_n [peV]
1	1.4065	6	5.4278
2	2.4592	7	6.0399
3	3.3210	8	6.6224
4	4.0827	9	7.1804
5	4.7790	10	7.7174

Here it can be seen that the energies for these states are smaller than the Fermi potential of the mirror by a factor of 10^{-5}. Because of this the approximation that the neutrons do not penetrate the mirrors is a good first approximation.

Nevertheless the potential is not infinite so there are corrections to the energies and the wave functions. In particular there is a finite penetration into the mirror. As a model, a constant potential V_0 inside the mirror and gravity above the mirror is assumed. By the continuity conditions for the wave function required by the Schrödinger equation, $\psi(0^-) = \psi(0^+)$ and $\psi'(0^-) = \psi'(0^+)$, the shifted energies and the penetration depth for the eigenstates can be calculated. For a detailed calculation see appendix B. In figures 2.4 and 2.5 the resulting energy shift and penetration depth can be seen for the first few states.
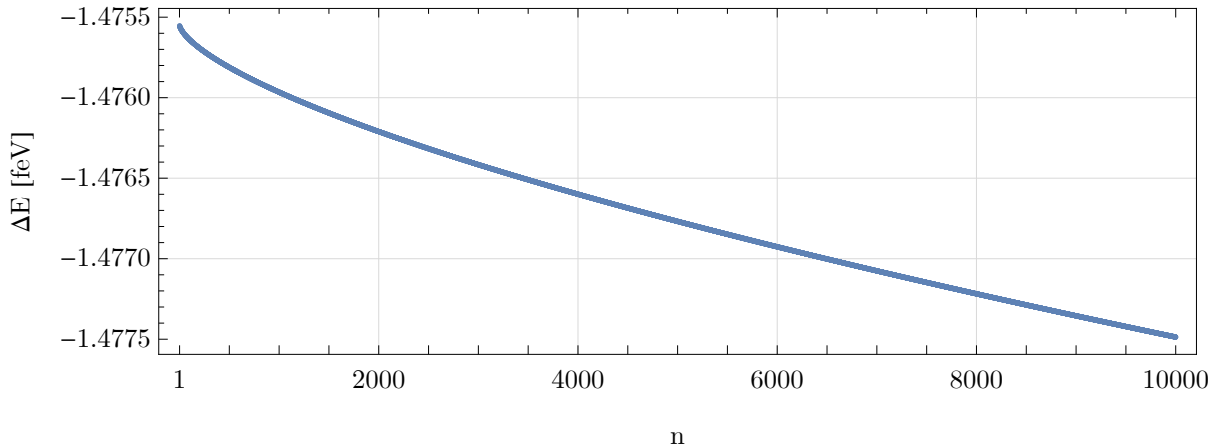
Figure 2.4: Shift of the Eigenenergies induced by a neutron mirror with $V_0 = 100\,\text{neV}$ compared to an infinite potential for the n-th Eigenstate.
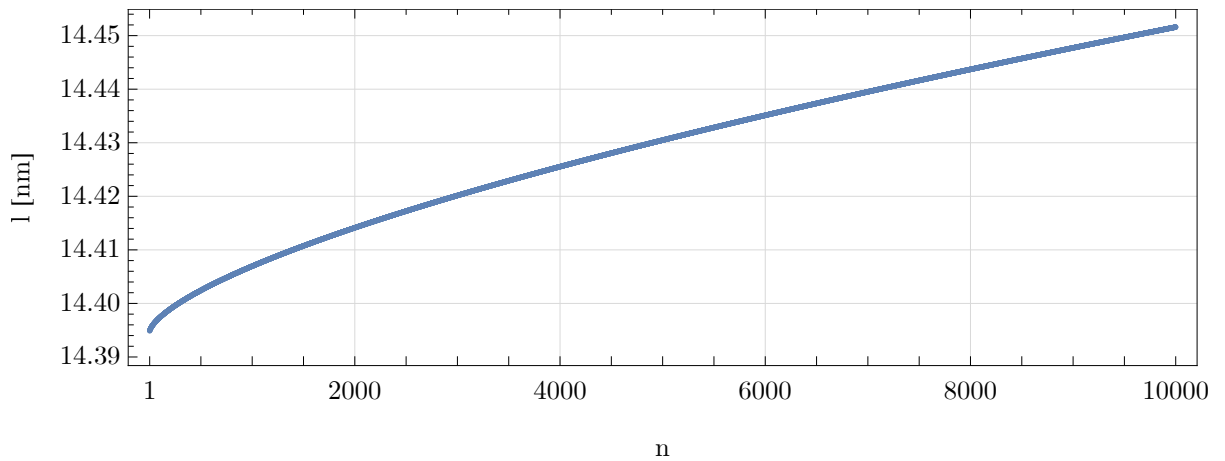
Figure 2.5: Penetration depth into a neutron mirror with $V_0 = 100\,\text{neV}$ for the n-th Eigenstate.

There are two main points resulting from these calculations: firstly the wave function enters multiple nanometres into the mirror surface, which means that the approximation of the mirror using a pseudo potential is valid, since the neutron interacts with hundreds of mirror nuclei [1]. Secondly the energy shifts are almost constant up to very high states. Because of this, transition energies between the states remain unchanged to a very high degree. From the plot the transition $|1\rangle \rightarrow |10000\rangle$ has a shift of $\Delta E \approx -2\,\text{aeV}$. At the current measurement precision this is of no relevance.

2.2 State selection

The ability to prepare and select gravity states of the neutrons is essential to be able to perform GRS experiments. The method we use to select neutrons in the ground state was first used in [4] to show the existence of gravity states for the neutron. Here I will give only a short overview of the basic principle that enables this selection.

In fig. 2.6 the basic schematic can be seen, where the neutron interacts with a mirror scatterer pair. The mirror is a flat glass plane at the bottom, and the scatterer also consists of a piece of glass, not flat but rough, on top. It is at a height of $l \approx 25\,\mu\text{m}$ above the mirror.

The neutrons enter this arrangement. The first process taking place is reflection upon entering the

Figure 2.6: Basic setup for the state selection: The neutron mirror at the bottom and a rough glass plate acting as a scattering surface at the top. The neutrons enter the slit from the left and every interaction of the neutron with the rough glass surface scatters the neutron out of the system.

slit. The overlap of the neutron wave function and the eigenstates under the scatterer can be calculated in principle, but there arise a few problems. First the eigenstates are given by a linea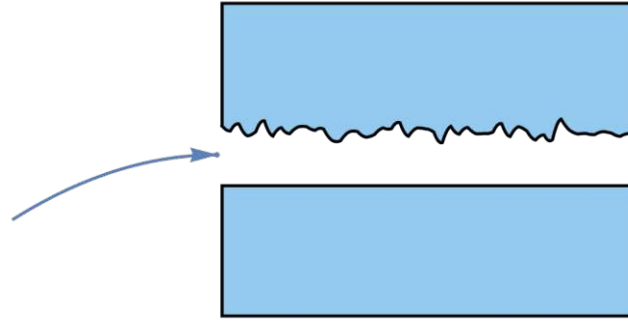r combination of Airy functions that vanish on the mirror surface and on the absorber surface. Since the absorber is rough, which in this context can be viewed as having a random surface structure, the exact geometry and therefore the linear combination can not be modelled. Second the exact wave function entering the slit to use for this purpose is unknown. As was shown in [4] it is reasonable to assume that high energy states under the absorber do not get populated. Once inside the absorber surface becomes dominant. The absorber can be modelled as a perfectly flat plate also with the same potential V_0 as the neutron mirror and with some effective potential V_{abs} on its surface that interacts with the neutrons. This potential encodes all roughness parameters like spikes, valleys as an effective interaction. The neutron wave function is given by the wave function valid for two flat mirrors and the interaction can be calculated perturbatively [18].

A sketch of this whole system can be seen in fig. 2.7 where $|\psi|^2$ for the first three wave functions is plotted. This shows, that the overlap for higher states gets bigger with increasing state number. The probability of scattering on this effective potential is described in [18]. Arguing from the overlap higher states get scattered more often by the absorber. Treating every scattering event as if it completely reshuffles the direction of movement of the neutron, neutrons in a higher state get scattered more often, thus propagating straight through the setup less often. These effects all increase the probability of a neutron that is travelling along its initial path to be in one of the lowest states. In practise it has been shown [9, 13, 19] that only the first three states are able to transmit through the system, all further excited states are highly suppressed. In fig. 2.8 the overlap integral for the first 20 states can be seen. The separation of the mirrors is set to $l = 25\,\mu m$ and the thickness of the slice where the probability is calculated is $d = 3\,\mu m$. This corresponds to the approximate parameters in the experiment and have been optimised over time within the qBOUNCE .

The state selection with the absorber is a complicated velocity dependent effect [20], and in 5.3.1 measurements can be seen that show that this is indeed an experimentally observable effect. The details of the state selection are treated as just given, without going into further calculations here. The important point is that the state preparation and selection is not perfect but that there is always the second state in addition to the ground state. Measurements made in 2019 and before suggest, that the state distribution after one absorber is $\approx (65\%, 25\%, 10\%)$ [13, 19, 21] for the first, second and third state. If more than one state is transmitted this can be treated as a mixed state. As is shown in the next section 2.5 for the two state system, a mixed state can be treated as a pure state with background. If there are more than two states contributing because the state preparation is non ideal this is only valid if the participating transitions are separated far enough, so that the envelopes of their transmission curves do not overlap. In the past a state distribution of $\approx (70\%, 30\%, 0\%)$ has been reported [7]. Current Ramsey measurements presented in 5.3.1 suggest that this reduction of state $|3\rangle$ can be attributed to the lower velocities used in
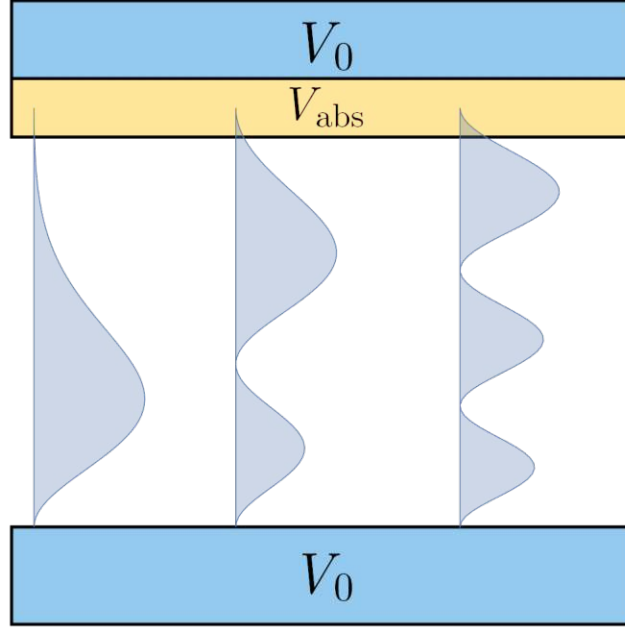
Figure 2.7: Basic setup for the state selection: The neutron mirror at the bottom and a rough glass plate called an absorber at the top. The neutrons enter the slit from the left and every interaction of the neutron with the rough glass surface scatters the neutron out of the system.

the past. As can be seen in the general sketch of the qBOUNCE experiment 2.1 the experiment uses two such absorber sections: one in the beginning for the state preparation and one in the end for final state selection. The transmission through the system is measured, which is mainly the ground state to ground state transition probability for the whole setup. Additional states present are treated as a statistical ensemble in multi state analyses.

2.3 Expectation of position and transition matrix elements

Here I will state the normalisation constants needed for the wave functions, the expectation value $\langle z \rangle$ and the transition matrix element V_{mn}. From chapter 2.1.1 we know that the solution to the time independent Schrödinger equation

$$E_n \psi_n(z) = \hat{H} \psi_n(z) \tag{2.11}$$

is proportional to the rescaled and shifted Airy function $\psi_n(z) = \mathrm{Ai}\left(\frac{z}{z_0} + \mathrm{AiZ}(n)\right)/N_n = \mathrm{Ai}\left(\frac{z}{z_0} - \frac{E_n}{E_0}\right)/N_n$, with eigenenergies E_n with a normalisation constant N_n. The normalisation constant is determined by calculating

$$\int_0^\infty |\psi_n(z)|^2 \mathrm{d}z = 1 = \frac{1}{N^2}\int_0^\infty \mathrm{Ai}\left(\frac{z}{z_0} + \mathrm{AiZ}(n)\right)^2 \mathrm{d}z = \frac{1}{N^2}z_0 \mathrm{Ai}'\left(\mathrm{AiZ}(n)\right)^2, \tag{2.12}$$

which can be evaluated in terms of Airy functions and its derivative by using the Airy equation. This and other integral identities for Airy functions are derived in appendix A. The full time independent eigenfunction and its energy in the linear gravity potential is given by

$$\psi_n(z) = \frac{\mathrm{Ai}\left(\frac{z}{z_0} + \mathrm{AiZ}(n)\right)}{\sqrt{z_0}\mathrm{Ai}'\left(\mathrm{AiZ}(n)\right)}, \ E(n) = -E_0 \mathrm{AiZ}(n) \tag{2.13}$$
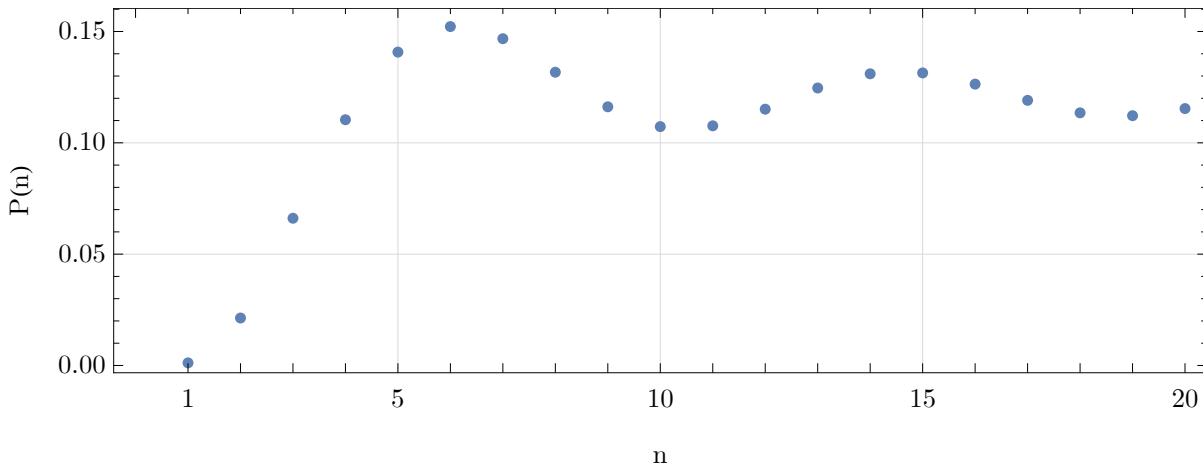
Figure 2.8: The probability $P(n)$ of finding a neutron in state n for a mirror gap of $d = 25\,\mu m$ in the area between 22 and 25 μm. To first order the scattering probability in the absorber can be taken to be proportional to this probability.

with an interesting consequence: the derivative $\psi'_n(0) = 1/\sqrt{z_0^3}$ for all eigenstates. This means that all eigenstates interact in the same way with the surface of the mirror, in particular with small irregularities like scratches or dust. These are likely present in small numbers. For surface interactions extending above 0 this is only approximately true when considering higher states. For small irregularities this can be treated as a state independent loss factor which just lowers the count rate especially when considering only the first three states.

The probability of the first 20 states to be within 5 μm of the mirror surface can be seen in fig. 2.9. The interaction time with a defect of this size is $t \approx 5\,\mu m/v \approx 1.6\,\mu s$, thus the interaction probability is $P \approx tP(z \in [0;5]\,\mu m) \approx 2.5 \times 10^{-7}$. This means that even for moderately sized surface irregularities, the scattering probability is quite low. Typically a single measurement point has 400 neutrons, therefore the probability that none of them scatter on a 5 μm irregularity is $P = (1 - 2.5 \cdot 10^{-7})^{400} \approx 0.9999$. Because of these considerations, the small scale surface properties such as minor scratches do not have to be taken into account. Large mirror defects, such as an oil film over the whole mirror surface is of much more concern. See chapter 5.3.2. Experimentally singular (<10) scratches of the mirror surface produced while cleaning d not effect the neutron count rate at all, although no destructive tests of this were performed.

To calculate the expectation value of the height above the mirror it is convenient to use the Hellmann-Feynman formula [22]

$$\langle \psi |\, \partial_\lambda \hat{H}\, |\psi \rangle = \partial_\lambda E_\lambda \,, \tag{2.14}$$

where λ is any parameter that appears in the Hamilton operator $\hat{H}$. For the case of a free neutron on top of a mirror $\hat{H} \hat{=} -\hbar^2/2/m_i\partial_z^2 + m_g g\hat{z}$. From this it can be easily seen that

$$z_n := \langle n |\, \hat{z}\, |n \rangle = \frac{\partial E_n}{\partial (m_g g)} = \frac{2}{3m_g g} E_n = -\frac{2}{3} z_0 \mathrm{AiZ}(n) \,. \tag{2.15}$$

where 2.4 and 2.10 were used.

For the transition matrix element V_{mn}, which is needed for the oscillating neutron mirrors, see below in chapter 2.4, one arrives at

$$V_{mn} := \int_0^\infty \psi_m(z) \frac{\partial}{\partial z} \psi_n(z) \mathrm{d}z = \frac{m_g g}{E_m - E_n} = \frac{1}{z_0 \left(\mathrm{AiZ}(n) - \mathrm{AiZ}(m) \right)} \,, \tag{2.16}$$

if $m \neq n$ and 0 otherwise. Since the ψ_m describe bound states vanishing at 0 and ∞ the $V_{mn} = -V_{nm}$ are antisymmetric as can be readily seen by partial integration. These are the main results of the appendix
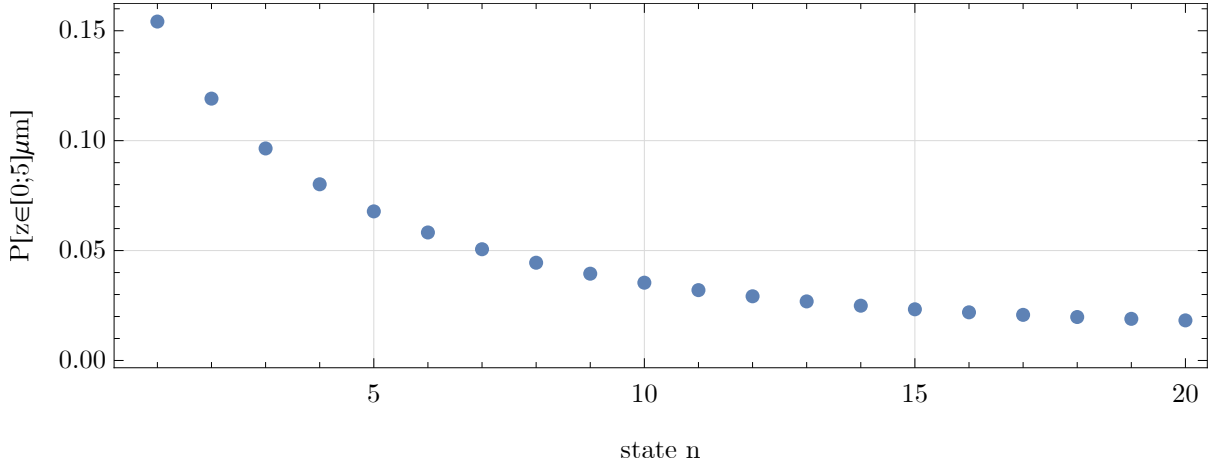
Figure 2.9: The probability $P(z \in [0;5]\mu m)$ of finding a neutron at a height between 0 and 5 µm above the mirror. The interaction probability with particles of this size is $\sim 10^{-7}$

A on integral identities of the Airy functions. There are many ways to derive these identities from the Airy differential equation the approach here was inspired by [23]

2.4 State transitions by oscillating boundary conditions

In order to describe transitions between states the potential $V(z,t)$ in equ. (2.6) is given by $V(z,t) = V_0\Theta(f(t) - z)$, where V_0 is the Fermi potential of the neutron mirror. This describes a moving surface on which the neutron is evolving in time. For the qBOUNCE experiment the mirrors are oscillated with a sinusoidal motion, so $f(t) = a\sin(\omega t + \phi)$, where a, ω and ϕ are the maximum displacement, angular frequency and phase of the mirror surface. In the experiment the quantity $a\omega$ is fixed to a constant value giving rise to symmetric two state transmission curves. Since in the Ramsey setup there are two oscillating sections, we have in principle two different sets of these parameters. Introducing a new coordinate system $\tilde{z} = z - f(t)$, $\tilde{t} = t$, the neutron is described by

$$i\hbar\partial_{\tilde{t}}\psi = -\frac{\hbar^2}{2m_i}\partial_{\tilde{z}}^2\psi + m_g g\tilde{z}\psi + V_0(-\tilde{z})\psi + m_g gf\psi + i\hbar\dot{f}\partial_{\tilde{z}}\psi \ . \tag{2.17}$$

Using the orthonormal time independent eigenfunctions from 2.10 to express $\psi = \sum_n \tilde{C}_n(t)e^{-iE_n t/\hbar}\psi_n$, multiplying by ψ_m and integrating from $z = 0$ to $z = \infty$ results in

$$\dot{\tilde{C}}_m(t) = -i\frac{m_g g}{\hbar}f\tilde{C}_m(t) + \dot{f}(t)\sum_{n=1}^{\infty}V_{mn}e^{i\omega_{mn}t}\tilde{C}_n(t) \ ,$$

$$V_{mn} = \int_0^{\infty}\psi_n(z)\frac{\partial}{\partial z}\psi_m(z)\mathrm{d}z \ . \tag{2.18}$$

Where $\omega_{mn} = (E_m - E_n)\hbar^{-1}$. This is the standard approach used in time dependent perturbation theory e.g. [24]. Equation (2.18) can be further simplified by partial gauge fixing via

$$\tilde{C}_m = e^{-i\frac{m_g g}{\hbar}\int_{t_0}^t f(t')\mathrm{d}t'}C_m \tag{2.19}$$

which results in

$$\dot{C}_m(t) = \dot{f}(t)\sum_{n=1}^{\infty}V_{mn}e^{i\omega_{mn}t}C_n(t) = a\omega\cos(\omega t + \phi)(t)\sum_{n=1}^{\infty}V_{mn}e^{i\omega_{mn}t}C_n(t) \ , \tag{2.20}$$

Table 2.2: Frequencies associated to the transition $|n\rangle \to |m\rangle$ given by $\nu_{mn} = (E_m - E_n)(2\pi\hbar)^{-1}$ for the first 15 states.

n\m	2	3	4	5	6	7	8
1	254.535	462.925	647.101	815.462	972.345	1120.36	1261.21
2		208.39	392.566	560.927	717.81	865.82	1006.68
3			184.176	352.537	509.42	657.431	798.288
4				168.361	325.244	473.255	614.112
5					156.883	304.894	445.751
6						148.011	288.868
7							140.858

n\m	9	10	11	12	13	14	15
1	1396.13	1525.99	1651.48	1773.14	1891.39	2006.58	2119.02
2	1141.59	1271.46	1396.95	1518.6	1636.85	1752.05	1864.48
3	933.203	1063.07	1188.56	1310.21	1428.46	1543.66	1656.09
4	749.027	878.889	1004.38	1126.04	1244.29	1359.48	1471.92
5	580.666	710.528	836.02	957.675	1075.92	1191.12	1303.55
6	423.783	553.645	679.137	800.792	919.042	1034.24	1146.67
7	275.772	405.635	531.126	652.782	771.031	886.227	998.661
8	134.914	264.777	390.268	511.924	630.173	745.369	857.803
9		129.863	255.354	377.01	495.259	610.454	722.889
10			125.492	247.147	365.396	480.592	593.026
11				121.656	239.905	355.1	467.535
12					118.249	233.445	345.879
13						115.195	227.63
14							112.434

where in the last equals sign the qBOUNCE case of $f(t) = a\sin(\omega t + \phi)$ was inserted. This equation describes the evolution of the occupation number for the eigenstates ψ_m, since $|\tilde{C}_m|^2 = |C_m|^2$ for all t. In tab. 2.2 the frequencies $\nu_{mn} = \omega_{mn}(2\pi)^{-1}$ for the first 15 states are given.

2.5 Ramseys Method of separated oscillating fields applied to Gravity Resonance Spectroscopy

As was shown in the previous chapter the special case of the Schrödinger equation with a time dependent boundary condition at the origin can be written as in eq. (2.20) for an arbitrary number of states. Following [24] using time dependent perturbation theory this equation can be viewed as a two state system, where the two states are given by $|p\rangle$ and $|q\rangle$ with occupation numbers $C_p(t)$ and $C_q(t)$. Higher order transitions are treated as perturbations as described below. This simplification gives

$$\begin{pmatrix} \dot{C}_p(t) \\ \dot{C}_q(t) \end{pmatrix} = a\omega\cos(\omega t + \phi) \begin{pmatrix} 0 & V_{pq}e^{i\omega_{pq}t} \\ V_{qp}e^{i\omega_{qp}t} & 0 \end{pmatrix} \begin{pmatrix} C_p(t) \\ C_q(t) \end{pmatrix}, \qquad (2.21)$$

where $V_{pq} = -V_{qp}$ are real and antisymmetric with respect to p and q and it is assumed that $E_p < E_q$ such that $\omega_q - \omega_p = \omega_{qp} > 0$ from here on out. This equation is still not analytically solvable, therefore the so called secular approximation is used [6, 24]. The general idea is this: the cos term contains $e^{i\omega t}$ and $e^{-i\omega t}$. Splitting the cos and combining the off diagonal terms in 2.21 gives

$$\begin{pmatrix} \dot{C}_p(t) \\ \dot{C}_q(t) \end{pmatrix} = \frac{a\omega}{2} \begin{pmatrix} 0 & V_{pq}\left(e^{i((\omega-\omega_{qp})t+\phi)} + e^{-i((\omega+\omega_{qp})t+\phi)}\right) \\ V_{qp}\left(e^{-i((\omega-\omega_{qp})t+\phi)} + e^{i((\omega+\omega_{qp})t+\phi)}\right) & 0 \end{pmatrix} \begin{pmatrix} C_p(t) \\ C_q(t) \end{pmatrix} , \tag{2.22}$$

As $\omega_{qp} > 0$ the terms containing $\pm(\omega + \omega_{qp})$ in the exponent oscillate faster than the $\pm(\omega - \omega_{qp})$. For high transition frequencies ω_{qp} and high excitation frequencies $\omega \approx \omega_{qp}$ the fast oscillating term can be excluded. The fast oscillating term can be included using time dependent perturbation theory and leads to a shift of the transition frequency see e.g. [25, 26]. In the NMR community this is known as the rotating wave approximation, where this approximation has a physical interpretation. Here it is purely mathematical in nature.

Dropping the fast oscillating terms and defining the detuning $\delta = \omega - \omega_{qp}$ and $u = \frac{a\omega V_{pq}}{2}e^{i\phi}$ eq. (2.22) gives

$$\begin{pmatrix} \dot{C}_p(t) \\ \dot{C}_q(t) \end{pmatrix} = \begin{pmatrix} 0 & ue^{i\delta t} \\ -u^*e^{-i\delta t} & 0 \end{pmatrix} \begin{pmatrix} C_p(t) \\ C_q(t) \end{pmatrix} . \tag{2.23}$$

Writing out these equations it is easy to show that

$$\ddot{C}_p - i\delta\dot{C}_p + |u|^2 C_p = 0, \quad C_q = \frac{\dot{C}_p}{u}e^{-i\delta t} . \tag{2.24}$$

With this the solution $C_p(t) = ce^{i\frac{\delta_+}{2}t} + de^{i\frac{\delta_-}{2}t}$, with c, d constant and $\delta_\pm := \delta \pm \sqrt{\delta^2 + 4|u|^2}$ is easily found. $\Omega_R := \sqrt{\delta^2 + 4|u|^2}$ is known as the generalised Rabi frequency. Defining the quantities $\cos(\alpha) := \frac{\delta}{\Omega_R}$ and $\sin(\alpha) := \frac{2|u|}{\Omega_R}$ is useful. Backtracking and expressing everything as a matrix equation for C_p and C_q and also expressing the constants c and d in terms of the occupation numbers at a reference time t_0 $C_p(t_0)$ and $C_q(t_0)$ leads after some work to the general solution

$$\begin{pmatrix} C_p(t) \\ C_q(t) \end{pmatrix} =$$

$$\begin{pmatrix} e^{i(t-t_0)\frac{\delta}{2}}\left(\cos\left((t-t_0)\frac{\Omega_R}{2}\right) - i\cos(\alpha)\sin\left((t-t_0)\frac{\Omega_R}{2}\right)\right) & e^{i(t+t_0)\frac{\delta}{2}+i\phi}\sin(\alpha)\sin\left((t-t_0)\frac{\Omega_R}{2}\right) \\ -e^{-i(t+t_0)\frac{\delta}{2}-i\phi}\sin(\alpha)\sin\left((t-t_0)\frac{\Omega_R}{2}\right) & e^{-i(t-t_0)\frac{\delta}{2}}\left(\cos\left((t-t_0)\frac{\Omega_R}{2}\right) + i\cos(\alpha)\sin\left((t-t_0)\frac{\Omega_R}{2}\right)\right) \end{pmatrix}$$

$$\begin{pmatrix} C_p(t_0) \\ C_q(t_0) \end{pmatrix} . \tag{2.25}$$

It is now convenient to express the quantities in the matrix in polar representation. Defining $a = \sqrt{\cos^2\left((t-t_0)\frac{\Omega_R}{2}\right) + \cos^2(\alpha)\sin^2\left((t-t_0)\frac{\Omega_R}{2}\right)}$ and $b = \sin(\alpha)\sin\left((t-t_0)\frac{\Omega_R}{2}\right)$, with the property $a^2 + b^2 = 1$, which is true because of the unitarity of this time evolution, and $\chi = -\arctan(\cos(\alpha)\frac{\sin((t-t_0)\frac{\Omega_R}{2})}{\cos((t-t_0)\frac{\Omega_R}{2})}) = -\arctan(\cos(\alpha)\tan((t-t_0)\frac{\Omega_R}{2}))$ eq. (2.25) is

$$\begin{pmatrix} C_p(t) \\ C_q(t) \end{pmatrix} = \begin{pmatrix} ae^{i\chi}e^{i\frac{\delta}{2}(t-t_0)} & be^{i\phi}e^{i\frac{\delta}{2}(t+t_0)} \\ -be^{-i\phi}e^{-i\frac{\delta}{2}(t+t_0)} & ae^{-i\chi}e^{-i\frac{\delta}{2}(t-t_0)} \end{pmatrix} \begin{pmatrix} C_p(t_0) \\ C_q(t_0) \end{pmatrix} . \tag{2.26}$$

This is the unitary time evolution for the occupation number for the states $|p\rangle$ and $|q\rangle$. Let the matrix for this time evolution be called $U(t, t_0)$. The probability to be in the state $|p\rangle$ at time t is given by

$$|C_p(t)|^2 = |ae^{i\chi}e^{i\frac{\delta}{2}(t-t_0)}C_p(t_0) + be^{i\phi}e^{i\frac{\delta}{2}(t+t_0)}C_q(t_0)|^2 . \tag{2.27}$$

which is the general form for a so called Rabi transition. In GRS this has been demonstrated in [8, 9]. If now the phase $\varphi = \arg(C_p(t_0)/C_q(t_0))$ between the states at time t_0 is random, such that it has to

be averaged in this equation, this probability simplifies to the incoherent sum

$$
\begin{aligned}
|C_p(t)|^2 &= a^2 \left|C_p\left(t_0\right)\right|^2 + b^2 \left|C_q\left(t_0\right)\right|^2 \\
&= a^2 \left(C_p\left(t_0\right)^2 - \left|C_q\left(t_0\right)\right|^2\right) + \left|C_q\left(t_0\right)\right|^2 .
\end{aligned}
\tag{2.28}
$$

Because the only two facts used for this equation is the averaging over the relative phase in the initial state and the unitarity of the time evolution this can be generalised to an arbitrary unitary time evolution operator $\hat{U}$ for a two state system where a^2 is replaced by $|\langle p|\hat{U}|p\rangle|^2$. This matrix element is of course also the only one contributing if $C_q(t_0) = 0$, which is the case at least approximately for many real world experiments, not for $q\textsc{Bounce}$ though.

For a typical Ramsey type experiment there is a first excitation for time $t = 0$ to $t = \tau$, then a free time evolution from time $t = \tau$ to a time $t = \tau + T$ and then again an excitation time from $t = \tau + T$ to $t = 2\tau + T$. In equation (2.23) these correspond to an excitation with $u = u_1$ for $t \in [0, \tau]$, $u = 0$ for $t \in [\tau, \tau + T]$ and , $u = u_2$ for $t \in [\tau + T, 2\tau + T]$. If $u = 0$ the $C_i(t)$ do not change in time, so that the final state of things at $t = 2\tau + T$ is given by

$$
\begin{pmatrix} C_p(2\tau + T) \\ C_q(2\tau + T) \end{pmatrix} = U_2(2\tau + T, \tau + T)U_1(\tau, 0) \begin{pmatrix} C_p(0) \\ C_q(0) \end{pmatrix}
\tag{2.29}
$$

The subscripts here indicate that all parameters in equation (2.26) for the matrix $U(t, t_0)$ could in general be different for the two excitations. The only quantity of interest at the end is the probability to go from state $|p\rangle$ to $|p\rangle$ which is given by $P(|p\rangle \to |p\rangle) = |C_p(2\tau + T)|^2$, for which only the absolute value squared of the pp entry of this matrix is needed. It is given by

$$
\begin{aligned}
P(|p\rangle \to |p\rangle) &= \\
&= \left| a_1 a_2 e^{i\left(\frac{\delta_1 + \delta_2}{2}\tau + (\chi_1 + \chi_2)\right)} - b_1 b_2 e^{i\left(\left(\frac{\delta_2}{2}(3\tau + 2T) - \frac{\delta_1}{2}\tau\right) + (\phi_2 - \phi_1)\right)} \right|^2 \\
&= \left| a_1 a_2 - b_1 b_2 e^{i\left(\left(\frac{\delta_2}{2}(2\tau + 2T) - 2\frac{\delta_1}{2}\tau\right) - (\chi_1 + \chi_2) + (\phi_2 - \phi_1)\right)} \right|^2 .
\end{aligned}
\tag{2.30}
$$

Using $\Delta\phi = \phi_2 - \phi_1$ and the fact that in a real experiment usually the a's, b's and Ω_R's are optimised to be the same for both excitations, the general formula reduces to

$$
\begin{aligned}
P(|p\rangle \to |p\rangle) &= \left| a^2 - b^2 e^{i(\delta T - 2\chi + \Delta\phi)} \right|^2 \\
&= a^4 + b^4 - 2a^2 b^2 \cos\left(\delta T - 2\chi + \Delta\phi\right) \\
&= 1 - 2a^2 b^2 \left(1 + \cos\left(\delta T - 2\chi + \Delta\phi\right)\right) .
\end{aligned}
\tag{2.31}
$$

Averaging over $\Delta\phi$ in eq. (2.30) one arrives at the formula for the mean μ of the Ramsey curve, and setting the exponential to 1 and -1 respectively gives the function for the upper ϵ_+ and lower bound ϵ_- of the envelope.

$$
\begin{aligned}
\epsilon_+ &= (a_1 a_2 + b_1 b_2)^2 \\
\mu &= (a_1 a_2)^2 + (b_1 b_2)^2 \\
\epsilon_- &= (a_1 a_2 - b_1 b_2)^2
\end{aligned}
\tag{2.32}
$$

A complete solution with envelope can be seen in fig. 2.10[1].

A helpful special case of 2.30 is obtained by setting $\delta_1 = \delta_2 = 0$.

$$
\begin{aligned}
P(|p\rangle \to |p\rangle) &= \left| a_1 a_2 - b_1 b_2 e^{i\Delta\phi} \right|^2 \\
&= \left| \cos\left(\frac{\tau}{2} V_{pq} a\omega_1\right) \cos\left(\frac{\tau}{2} V_{pq} a\omega_2\right) - \sin\left(\frac{\tau}{2} V_{pq} a\omega_1\right) \sin\left(\frac{\tau}{2} V_{pq} a\omega_2\right) e^{i\Delta\phi} \right|^2 \\
&= \begin{cases} \cos^2\left(\frac{\tau}{2} V_{pq}\left(a\omega_1 + a\omega_2\right)\right), & \Delta\phi = 0 \\ \cos^2\left(\frac{\tau}{2} V_{pq}\left(a\omega_1 - a\omega_2\right)\right), & \Delta\phi = \pi \end{cases} .
\end{aligned}
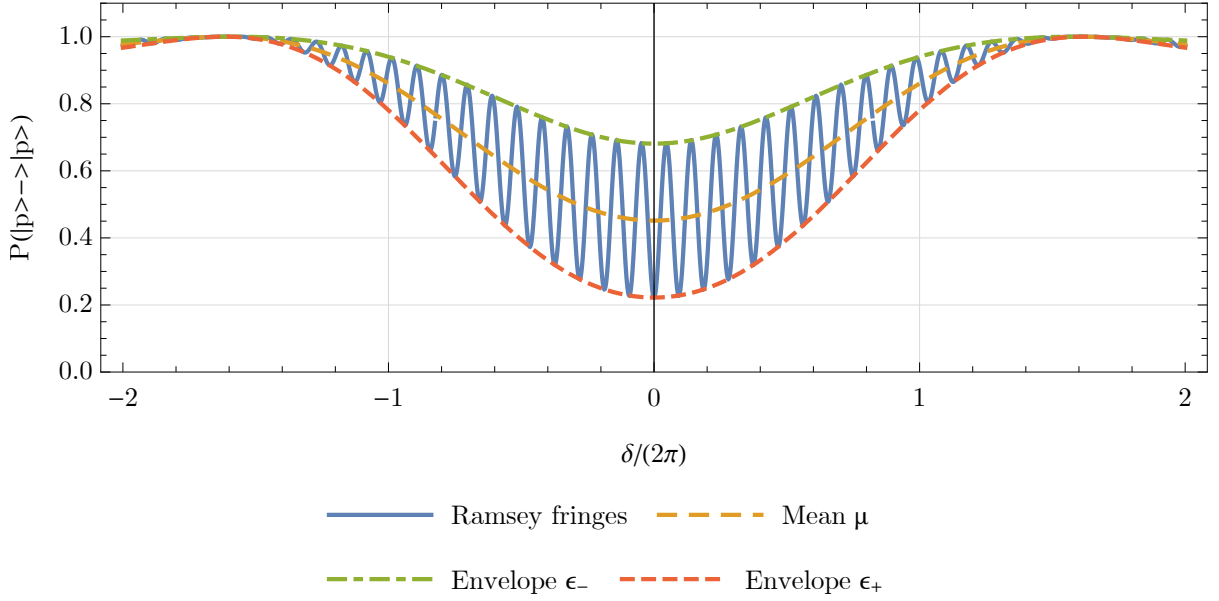\tag{2.33}
$$

---

[1] creepy mouth plot

Figure 2.10: The complete Ramsey transition curve from eq. (2.30), showing the mean and the envelope form eq. (2.32) with arbitrary parameters $T = 7$ and $\tau = 1$, $u_1 = 1.4$ and $u_2 = 0.4$.

With this systematic checks on the oscillation strength can be performed. For the zero phase case the sum of the two oscillation velocities $a\omega_i$ can be tuned to achieve a minimum in the probability. Then the π phase can be used to check whether or not the two oscillation velocities are the same. Since this is a $\cos^2$ term this is not very sensitive but it's a rough sanity check to see very large deviations from expectations.

It is interesting to expand the parameters in equation (2.31) around $\delta = 0$, which shows the basic properties of the Ramsey curve at resonance. The parameter definitions are repeated here for convenience

$$u = \frac{a\omega V_{pq}}{2}e^{i\phi}, \ \delta = \omega - \omega_{qp} = 2\pi(\nu - \nu_0), \ \Omega_R = \sqrt{\delta^2 + 4|u|^2}$$

$$\cos(\alpha) = \frac{\delta}{\Omega_R}, \ \sin(\alpha) = \frac{2|u|}{\Omega_R}$$

$$a = \sqrt{\cos^2\left((t - t_0)\frac{\Omega_R}{2}\right) + \cos^2(\alpha)\sin^2\left((t - t_0)\frac{\Omega_R}{2}\right)}$$

$$b = \sin(\alpha)\sin\left((t - t_0)\frac{\Omega_R}{2}\right)$$

$$\chi = -\arctan(\cos(\alpha)\frac{\sin((t - t_0)\frac{\Omega_R}{2})}{\cos((t - t_0)\frac{\Omega_R}{2})}) = -\arctan(\cos(\alpha)\tan((t - t_0)\frac{\Omega_R}{2})) \ ,$$

(2.34)

where all quantities here could have different values for the two different oscillating sections as is the case in (2.30). ν_0 is the transition frequency between the two states. The expansion around $\delta = 0$ gives

$$2a^2 b^2 \approx 2\cos(|u|\tau)^2\sin(|u|\tau)^2 + \mathcal{O}(\delta^2) \ ,$$

$$2\chi \approx -\frac{\tan(|u|\tau)}{|u|}\delta + \mathcal{O}(\delta^3) \ ,$$

(2.35)

and to this order

$$P(|p\rangle \to |p\rangle) = 1 - 2\cos(|u|\tau)^2\sin(|u|\tau)^2\left(1 + \cos\left(\delta\left(T + \frac{\tan(|u|\tau)}{|u|}\right) + \Delta\phi\right)\right) \ .$$
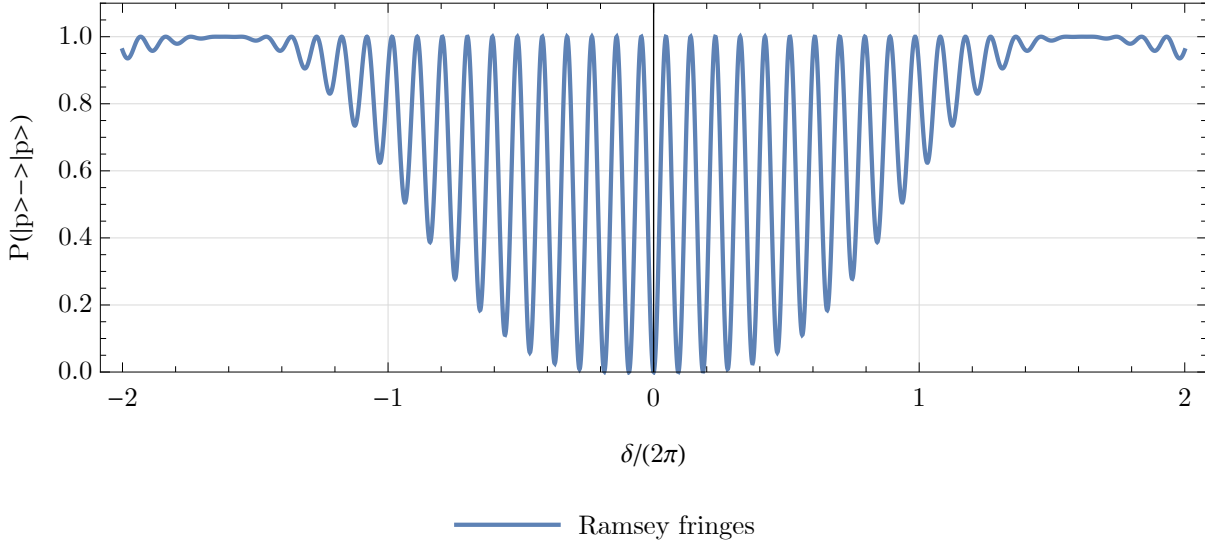
(2.36)

Figure 2.11: The Ramsey transition curve with parameters $T = 10$ and $\tau = 0.6$ with two $\frac{\pi}{2}$ flips.

From this it can be seen that the full width at half maximum w_ν in Hz is given by

$$w_\nu = \frac{1}{2\left(T + \frac{\tan(|u|\tau)}{|u|}\right)} \ . \tag{2.37}$$

In the case of an ideal excitation the probability to remain in state $|p\rangle$ at $\delta = 0$ is zero which is achieved by $|u| = \frac{\pi}{4\tau}$. This is known as a $\frac{\pi}{2}$-flip, resulting in

$$
\begin{aligned}
P(|p\rangle \to |p\rangle) &= \frac{1}{2}\left(1 - \cos\left(\delta\left(T + \tau\frac{4}{\pi}\right) + \Delta\phi\right)\right) \\
&= \frac{1}{2}\left(1 - \cos\left(\frac{\pi(\nu - \nu_0)}{w_\nu} + \Delta\phi\right)\right) \ , \\
w_\nu &= \frac{1}{2\left(T + \tau\frac{4}{\pi}\right)} \ , \\
a\omega &= \frac{\pi}{2V_{pq}\tau} \ .
\end{aligned}
\tag{2.38}
$$

In fig. 2.12 the central fringes of fig. 2.11 can be seen together with this cosine approximation. This approximation can be used to estimate the width of the central fringe.   If the relative phase between the two oscillating mirrors is a linear function of the detuning $\Delta\phi = (T + \tau\frac{4}{\pi})f\delta$ the width is given by

$$w_\nu^f = \frac{1}{2(T + \tau\frac{4}{\pi})(1 + f)} = \frac{w_\nu}{1 + f} \ . \tag{2.39}$$

Any choice for $\Delta\phi$ leaves the envelope invariant as can be seen in fig. 2.13.

Now the question for the validity of this calculation using the secular approximation has to be answered. The worst case of the secular approximation is given for the transition $|1\rangle \to |2\rangle$, where $\omega_{21} \approx 1600$. As will be shown in 4.1.2 the transition frequency gets shifted by a small amount, which is known as the Bloch-Siegert shift in NMR. In an electromagnetic Ramsey experiment the effect can be turned on and off by changing the way of electromagnetic excitation. For a magnetic field rotating perpendicular to the quantisation axis in the xy-plane with constant field magnitude the interaction Hamiltonian is given by a matrix similar to (2.23)
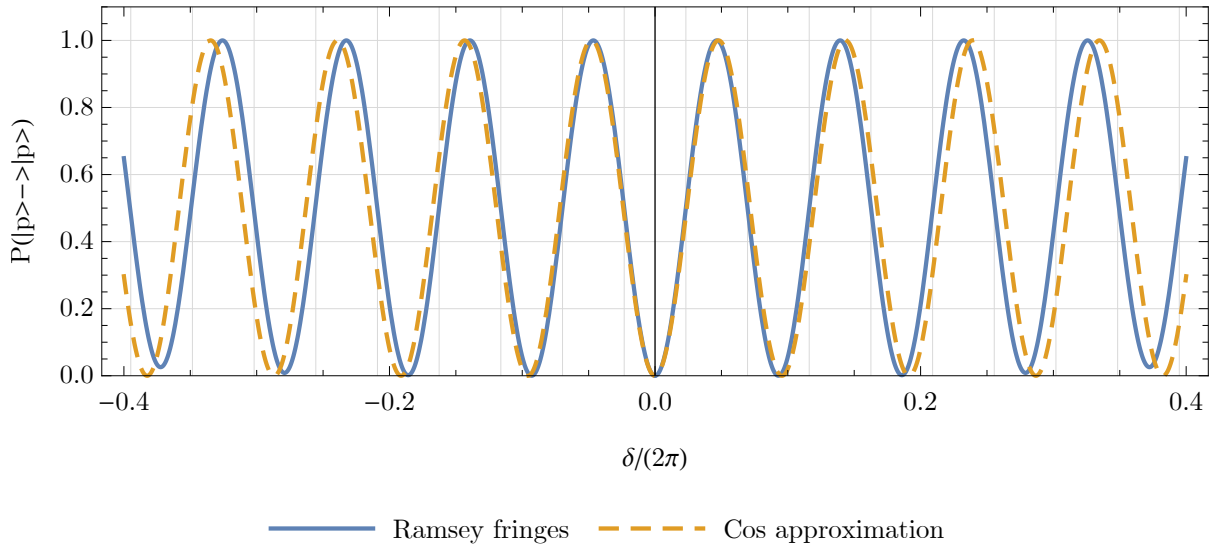
Figure 2.12: The Ramsey transition curve around the central fringe together with the cosine approximation (2.38) with the same parameters as fig. 2.11 and the vertical grid lines are spaced according to eq. (2.37).
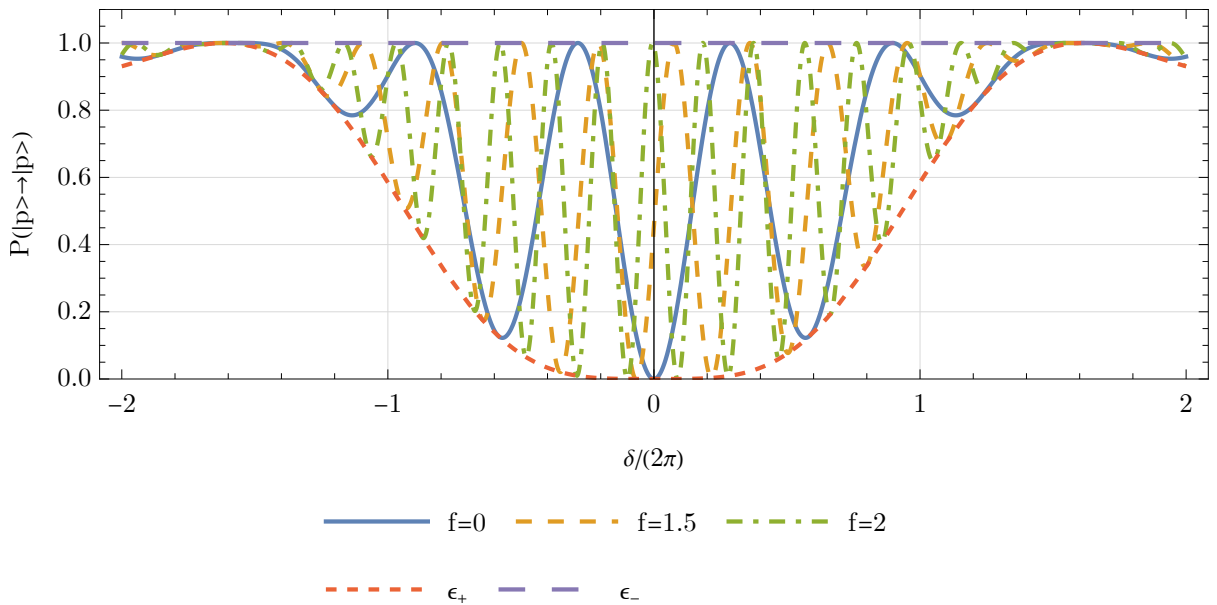
Figure 2.13: The Ramsey pattern for a relative phase between the two excitations $\Delta\phi = (T + \tau\frac{4}{\pi})f\delta$. Such a phase does not change the shape of the envelope $\epsilon_\pm$, but the exact location of the minimum can be shifted by differing amounts. Only in the f=0 case no absolute shift in the minimum is observable highlighting the importance of the control over the phase.

$$B\left(\cos(\delta t)\sigma_x + \sin(\delta t)\sigma_y\right) =$$
$$\begin{pmatrix} 0 & B\left(\cos(\delta t) - i\sin(\delta t)\right) \\ B\left(\cos(\delta t) + i\sin(\delta t)\right) & 0 \end{pmatrix} = \begin{pmatrix} 0 & Be^{-i\delta t} \\ Be^{i\delta t} & 0 \end{pmatrix}, \tag{2.40}$$

where σ_x and σ_y are the Pauli matrices. For a magnetic field oscillating only in the x direction the equation equivalent to (2.21) with cos terms. So by rotating the magnetic field a direct compensation for this shift is possible.

For qBOUNCE the effect is always present. Additionally there is the question of the two state approximation. The first few transition frequencies are given by tab. 2.2. With a width of $w_\nu \approx 8\,\mathrm{Hz}$ the central fringes seem to be separated far enough when starting from the first or second state. Higher order effects lead to a shift in GRS in general. If this is relevant at the current measurement accuracy will be discussed in more detail in chapter 4.1.

2.6 Error estimation

In order to choose a measurement strategy the expected error for a measurement can be obtained. Here the general method is illustrated using the cosine approximation (2.38), but the general approach also works for the full Ramsey solution, albeit with significant equation manipulation. As is known from statistics [27] the quantity

$$\chi^2 = \sum_{i=1}^{N} \frac{(y_i - f(x_i|a_k))^2}{\sigma_i^2}, \tag{2.41}$$

where y_i are the measured data with N data points in total, σ_i are the known standard deviations of the measurements y_i and $f(x_i|a_k)$ is the model compared to the data at coordinates x_i with parameters a_k, where $k \in \{1, 2, ..., K\}$ such that there are K parameters in total, follows a χ^2-distribution with $N - K$ degrees of freedom if each of the y_i follows a normal distribution. This is only valid if the model describes the true data. Conversely this can be interpreted as the χ^2-distribution for the parameters a_k. It can be shown [27] that if the a_k follow a multivariate normal distribution with covariance matrix $\mathbf{C}$ the quantity

$$\chi^2 = \left(\mathbf{a} - \mu_{a_k}\right)^T \mathbf{C}^{-1} \left(\mathbf{a} - \mu_{a_k}\right) \tag{2.42}$$

follow a χ^2 distribution with K degrees of freedom, where μ_{a_k} is the vector of means of the a_k. In order to find the parameters a_k in (2.41) the a_k are chosen to produce the minimum of the χ^2 quantity. This means

$$\partial_l \chi^2 = -2 \sum_{i=1}^{N} \frac{(y_i - f(x_i|a_k))}{\sigma_i^2} \partial_l f(x_i|a_k) = 0 \tag{2.43}$$

where $\partial_l = \frac{\partial}{\partial a_l}$. To extract $\mathbf{C}^{-1}$ χ^2 has to be expanded to second order

$$\partial_m \partial_l \chi^2 = 2 \sum_{i=1}^{N} \left(\frac{1}{\sigma_i^2} \left(\partial_m f(x_i|a_k)\right) \left(\partial_l f(x_i|a_k)\right) - \frac{(y_i - f(x_i|a_k))}{\sigma_i^2} \partial_m \partial_l f(x_i|a_k) \right)$$
$$= 2\mathbf{C}_{ml}^{-1} \tag{2.44}$$

Further simplification of this is possible if the model f is linear in the parameters a_k. Using the model (2.38) to estimate ν_0 and w_ν the covariance matrix can be directly calculated from (2.44) but the final equation is too extensive to show here in full.

By inverting this the covariance matrix can be found and the error estimates can be given for a specific measurement scheme. qBOUNCE has decided on the following scheme to determine the transition frequency of a single transition. Three points one at ν_0 one at $\nu_0 + w_\nu/2$ and one at $\nu_0 - w_\nu/2$ with $\Delta\phi = 0°$ and then the same frequency points with $\Delta\phi = 180°$ are taken. Since the ν_0 and w_ν are not known theoretical estimates are used to set the values in the experiment. Using $g \approx 9.805$ gives
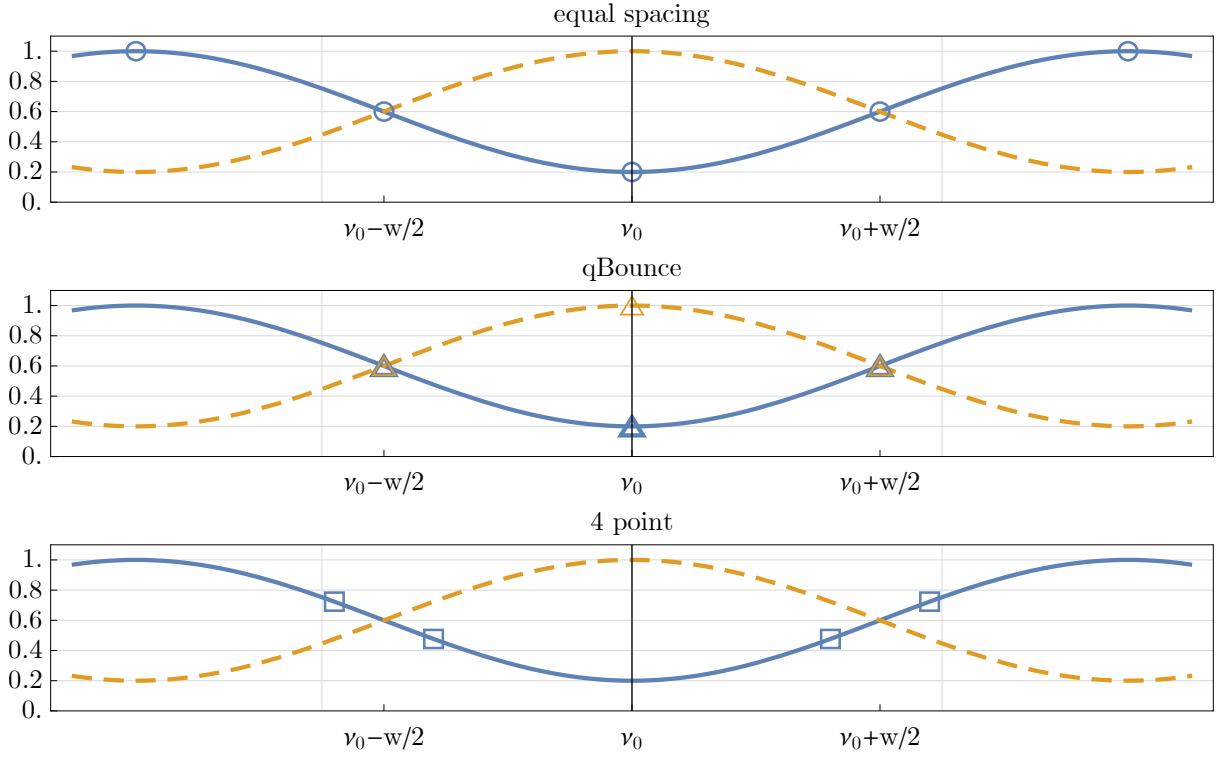
Figure 2.14: Different measurement schemes to investigate a Ramsey resonance curve. The currently used strategy for GRS measurements is shown in the second plot.

$\nu_{16} = 972.345\text{Hz}$ as an initial guess for all $|1\rangle \rightarrow |6\rangle$ measurements, where the measured value of g was used. For the w_ν the measured velocity spectrum is convolved with the Ramsey theory function to calculate the expected width. This has been sufficiently accurate. In a long running experiment focusing purely on measuring these six points, the values for ν_0 and w_ν could be iteratively tuned after each 6 point cycle, but this has not been done to avoid any unwanted bias introduced by the choice of new parameters, since the experiment has been used now for the first time to take precision measurements and systematics are still under investigation. Furthermore the time spent at each point can be varied in order to give different weights to the parameters. Measuring only at $\nu_0 \pm w_\nu/2$ would give the smallest frequency error, but then there would be no evidence that there is a transition at all since they would all lie at the same value. In fig. 2.14 three methods are shown for the simplified model

$$P = 1 - \frac{\kappa}{2}\left(1 + \cos\left(\frac{\pi}{w}\left(\nu - \nu_0\right) + \phi\right)\right) \tag{2.45}$$

with a drop of κ from the maximum, a width w and a transition frequency of ν_0. The three ways to sample points is shown as square, circular and triangle points. The circles are points spaced equally from $-w$ to $+w$, here with 5 points, this was used by J. Bosina [21] for multiple measurements. The triangles show the current measurement program used by qBOUNCE . And finally the squares represent the so called "four-point method" which uses two points at the points of highest slope to the left and to the right of the transition.

To compare these methods equation (2.45) can be evaluated in (2.44). The general scaling for all models is $\sigma^2 \sim N^{-1}$ where N is the number of neutrons in each measurement point. The different methods have slightly different properties: The four-point method has a small offset around the central value where the measurement error has to be small enough in order to be able to find the transition frequency. Furthermore, if $\kappa \neq 1$ there is a large correlation between κ and w.

In the limit of a perfect experiment the qBOUNCE method gives the same error on the transition

frequency, but there is no correlation between κ and w. Removing the points in the central fringe and only measuring in the slopes gives the same result, where the error in κ increases.

For the equal spacing method there is again a correlation between κ and w, and there is a scaling with the number of measurement points. In order to get to the same error estimate for ν_0 as with the other two methods, more intermediate points have to be added. This is expected since many points are not close to the points of highest slope. The calculated covariance matrices can be seen in (2.46)-(2.48), where $\kappa = 0.9$, $w = 8\,\text{Hz}$, the offset for the four-point method was set to $\pm w/10 = \pm 0.8\,\text{Hz}$ and ν_0 is at the center of the chosen points. In principle, once the location of the transition is sufficiently known, the measurement points can be chosen such that this is the case in a real experiment. In a real experiment the contrast $\kappa < 1$ since any detection mechanism has some background even with perfect excitation.

$$\mathbf{C}_{4-point} = \frac{1}{N} \begin{pmatrix} 2.205 & 0. & 0. \\ 0. & 61.093 & -7.317 \\ 0. & -7.317 & 1.056 \end{pmatrix} \tag{2.46}$$

$$\mathbf{C}_{qBounce} = \frac{1}{N} \begin{pmatrix} 2.422 & 0. & 0. \\ 0. & 9.687 & 0. \\ 0. & 0. & 0.01 \end{pmatrix} \tag{2.47}$$

$$\mathbf{C}_{5equalpoints} = \frac{1}{N} \begin{pmatrix} 4.843 & 0. & 0. \\ 0. & 19.694 & -0.057 \\ 0. & -0.057 & 0.01 \end{pmatrix} \tag{2.48}$$

In the limiting case of no separation of the slope points in the four point method the error for ν_0 and w is the same as for the qBOUNCE method.

These results are encouraging, the method used by qBOUNCE optimises a measurement scheme where the location and the contrast of the transmission function have to be measured. This is intrinsic to the experimental setup since control over the initial state preparation and multi state transitions can not be asserted to an extent to eliminate the κ from the fit. The only caveat is that the phases between the excitation regions needs to be adjusted, which is not a problem in the qBOUNCE setting but might be difficult in other experimental Ramsey implementations. The total number of neutrons measured is the number of measurement points for each method multiplied by N where in the qBOUNCE case the central two points can be omitted once the contrast of the measurement is not important any more, without loss of precision for the transition frequency.

Chapter 3

Setup

3.1 The UCN & VCN Facility PF2 At ILL

The current qBOUNCE experiment is located at the Instrument PF2 at the ILL since 2016 at the UCN beam. [28] In fig. 3.1 the general setup of PF2 can be seen. The reactor provides thermal neutrons to a volume of liquid deuterium. This liquid deuterium thermalises the neutrons to $\approx 24\,\mathrm{K}$. From there the neutrons go up and follow the so called vertical guide. This neutron guide is the section of a large circle. Neutrons that are too fast can not follow the bend and end up leaving the neutron guide. Slower neutrons are reflected at the guide walls and encounter a split. One of the beams continues directly to the VCN cabin, which provides Very Cold Neutrons with a velocity of about $50\,\mathrm{m\,s^{-1}}$. The other path leads to the so called Steyerl Turbine. [1, 2, 29] The neutrons hit blades with a velocity of about $25\,\mathrm{m\,s^{-1}}$, where they are reflected, and end up with a velocity of $\approx 8\,\mathrm{m\,s^{-1}}$. The bulk of these neutrons is directed towards one of the three beam ports EDM, UCN, MAM. This is done with a moveable piece of neutron guide. Finally there is the test beam, it has access to the turbine directly and provides a low flux sourced from the neutron background in the turbine. The derived neutron flux over the velocity can be seen in fig. 3.2

This design provides the highest possible UCN flux to the beam ports, but it has the disadvantage that only one beam port at a time can receive neutrons. Because of this experiments request neutrons in a time-shared mode between all active experiments. PF2 then provides logic signals to the experiments to control the experimental logic. This is done via the ILL software NOMAD that is used to control all Instruments at the ILL.
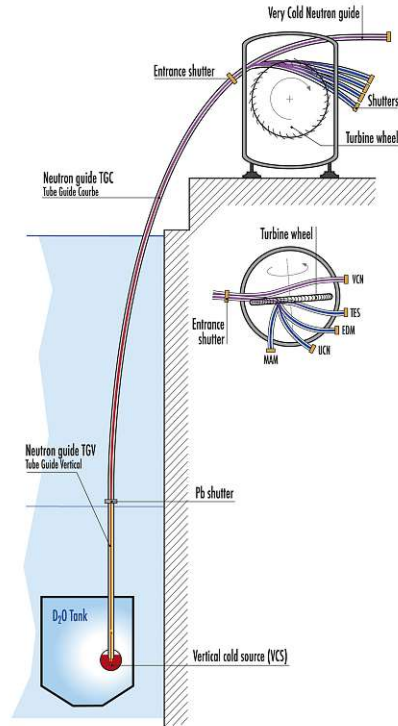

Figure 3.1: Schematic overview of the PF2 instrument. [28]

3.2 Experimental Platform of the qBOUNCE Setup

3.2.1 Vacuum chamber

The vacuum chamber in qBOUNCE was purpose built for the Ramsey experiment. First of all, the length of the setup ($> 1\,\mathrm{m}$) necessitates a large granite table, which has a precision ground surface. The second

velocity spectra of PF2 beam ports

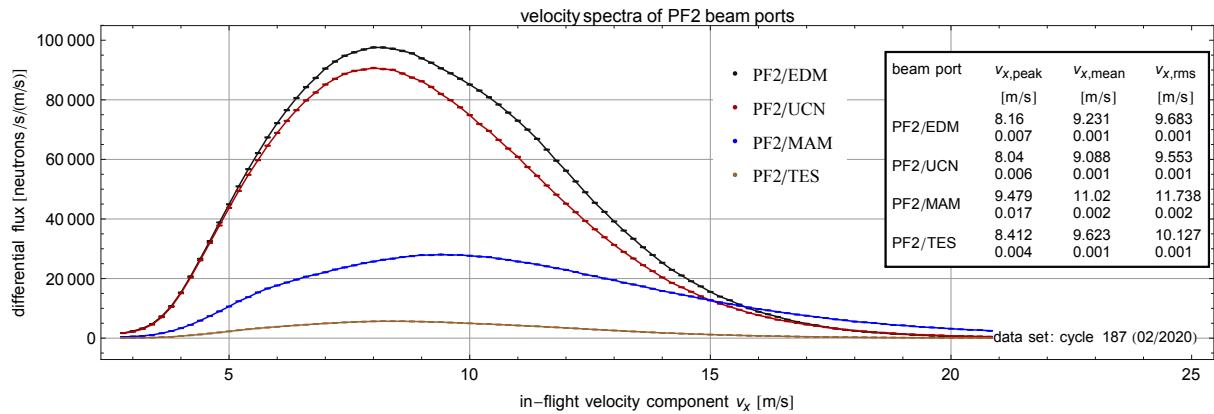| beam port	$v_{x,peak}$ [m/s]	$v_{x,mean}$ [m/s]	$v_{x,rms}$ [m/s]
PF2/EDM	8.16 0.007	9.231 0.001	9.683 0.001
PF2/UCN	8.04 0.006	9.088 0.001	9.553 0.001
PF2/MAM	9.479 0.017	11.02 0.002	11.738 0.002
PF2/TES	8.412 0.004	9.623 0.001	10.127 0.001

data set: cycle 187 (02/2020)

Figure 3.2: Differential neutron flux for the different output ports of the PF2 instrument. [30] qBOUNCE is located at the UCN port with the lowest mean velocity at PF2. The integrated flux is $\approx 650\,\text{kn/s}$ for the UCN beam.

purpose is to provide magnetic shielding. Because of this the chamber is clad with a double layered μ-Metal shielding that provides a shielding factor of ≈ 80 this is described further in section 3.3.3. The vacuum that can be reached is $\lesssim 10^{-5}$ mbar. The vacuum chamber is described in great detail in [13]. For UCN beam type experiments a better vacuum is not needed as has been demonstrated in [31] within the qBOUNCE vacuum chamber. Although this was not a high precision experiment, the count rate through air at $p < 10\,\text{mbar}$ was determined to be indistinguishable from the count rate at $p \approx 1 \times 10^{-5}$ mbar for a flight length of $l_p \approx 670\,\text{mm}$. Since the setup has a total length from the end of the beam tube to the neutron detector of $l \approx 1.1\,\text{m}$ the neutron losses at 5×10^{-5} mbar can be neglected for the most part. There is one caveat to this, the state preparation. Since the absorbers are made of rough glass plates, air gets trapped in the ridges and diffuses out only very slowly after pumping. In measurements the zero rate has been observed directly after pumping and it was shown that the rate increases over a time of $\approx 1\,\text{h}$ after the pressure in the chamber was already stationary. Therefore after pumping the chamber, a sufficiently long settling time of $t \approx 3\,\text{h}$ was taken into account. In typical measurement runs for the qBOUNCE setup the chamber is closed for weeks at a time, so this is not a very restricting problem. For future iterations of Ramsey GRS the pressure might become an important part of the experiment, necessitating better control.

3.2.2 Levelling of the experiment

The whole experiment is set up on a granite table that is flat to within $1\,\mu\text{m}$ over the whole surface. The surface of the granite has to be aligned with the local gravitational acceleration $\overrightarrow{g}$ This is done by a two fold mechanism. First the absolute alignment is achieved by using a calibrated water level that has a measuring accuracy of $10\,\mu\text{rad}$. This water level is used as the absolute reference. To eliminate drifts from this position, there is a two axis angle sensor mounted to the granite. This is used to monitor the current tilt of the whole granite and to correct for unavoidable drifts. The granite is tilted by three piezos underneath. The piezos are controlled by a PID controller to regulate the offset of the granite from the initial values to zero. With this the surface of the granite is stable to a few nrad. A measurement of the pitch and tilt angles can be seen in fig. 3.3.
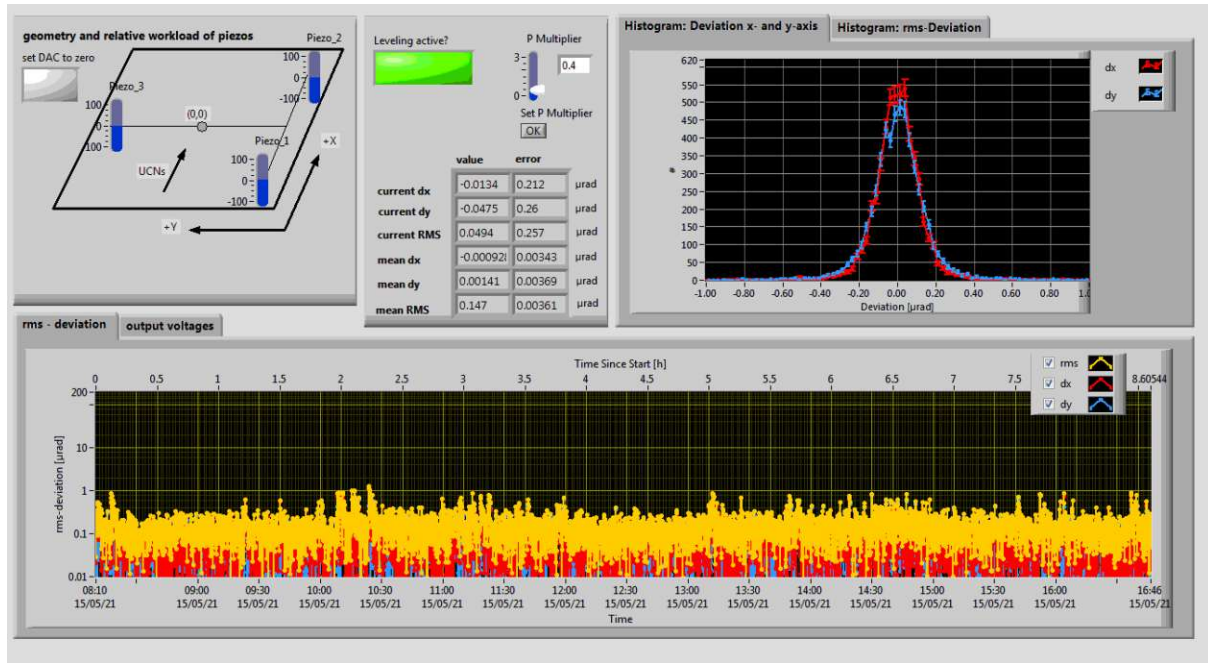
Figure 3.3: Sample measurement of the tilt sensor which aligns the whole experiment. In the top tight the time histogram of the angle deviation can be seen, in the bottom the individual measurements. The spikes seen at 10:15 are due to people walking in the reactor hall.

This shows that the final deviation from the zero point is on average $\approx 1\,\mathrm{nrad}$ in each direction over a 7 hour time period, indicating a small offset from the set zero point. For a single measurement point the standard deviation is $\approx 100\,\mathrm{nrad}$ A few features of this data has to be highlighted. During the day there are works going on in the reactor and with other experiments, therefore the granite levelling system deviates more from the mean. If there is heavy machinery moved around (like forklifts, large vacuum chambers or lead weights) the whole floor of the reactor building tilts more than can be corrected just by the piezos. If this happens the measurement has to be stopped and the mounting points of the vacuum chamber are adjusted such that the correction angle is in range again for the piezos. In the past this had to be done once or twice per year.

A deviation α from perfect alignment would lead to a systematic decrease of the effective acceleration of the neutron. The acceleration onto the neutron mirror is given by $g' = g_0 \cos(\alpha) \approx g_0 \left(1 - \alpha^2/2\right)$ which is smaller than the actual value of g. In addition there would be an acceleration parallel to the mirror which is $a_p = g_0 \sin(\alpha) \approx g_0 \alpha$. Using the worst case of $10\,\mu\mathrm{rad}$ gives $g' \approx g_0 \left(1 - 0.5 \cdot 10^{-10}\right)$. The acceleration parallel to the mirror is $a_p \approx g_0 \cdot 10^{-5}$. This acceleration changes the velocity of the neutron over the neutron mirrors. Because of this the interaction with the oscillating mirrors is slightly modified but since the effect is small and the velocity spectrum used in the setup spans a large interval of $v \in [4; 14]\mathrm{m\,s^{-1}}$ this is negligible. Similar as outlined in 4.2.3 the acceleration parallel to the mirror surface leads to a change of the centrifugal and Coriolis acceleration terms but the change in velocity, $\Delta v \approx 0.1 \cdot 1 \times 10^{-4}\,\mathrm{m\,s^{-1}}$ where 0.1 is the approximate flight time of a neutron across the setup and $1 \times 10^{-4}\,\mathrm{m\,s^{-1}}$ is $g_0 \cdot 10^{-5}$. This is very small compared to the base velocity. Thus a misalignment of the neutron mirrors has no significant impact on the current qBOUNCE experiment.

3.3   Ramsey Spectroscopy Setup

In this section I will describe the experimental effort that has to be taken for a measurement to be performed. This includes all necessary information that has to be determined in order to be able to choose the measurement points for a Ramsey GRS measurement as well as systematic checks that have been
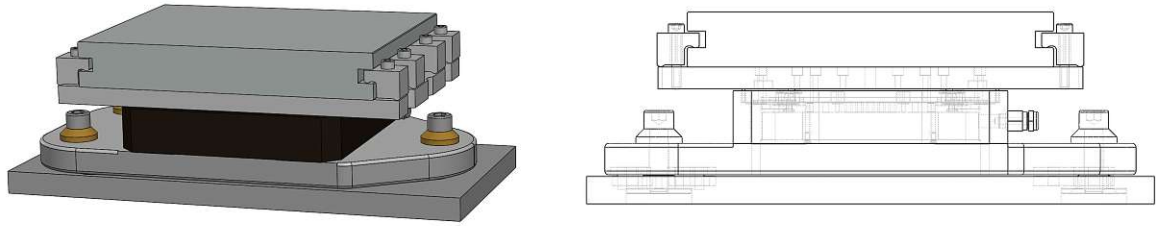
Figure 3.4: Stage for one mirror section from [13]. The five elements are visible from bottom to top: the baseplate mounted to the granite, the spacer plate for height adjustment, the piezo stage in black, the mirror holder plate and neutron mirror. With the clamps on the left and right holding the mirror in place.

performed and the limitations that were found in the last three years (2019-2021). Detailed descriptions of the whole setup can further be found in [13] and [21].

3.3.1 Neutron mirrors and holders

The neutron mirrors are flat Bk-7 glass slates that are ground to a measured radius of curvature of > 2.8 km. Further details can be found in [13]. They are mounted to a multiple elements stage shown in fig. 3.4. There is a baseplate on the bottom with a plate on top, where rubber spacers are placed. This allows for small range height adjustment for rough alignment. On top of this there are piezo stages, detailed in 3.3.5. On the piezo stage there is an aluminium plate to which the neutron mirror is fastened using clamps either side of the neutron flight path. The mirrors for sec I and V have holes to include stand-offs used for clamping down the absorbers. The mirrors are coated with an aluminium layer with a thickness of about $d \approx 120(12)$ nm and a protective scratch layer of SiO_2 with a thickness of $\approx 180(15)$ nm. The aluminium layer is used to reflect the interferometer beams that are used for monitoring the oscillations of the mirror surfaces. Sections I, II, IV and V have a nominal length of $l \approx 152$ mm and section III $l \approx 340$ mm. On top of sections I and V the absorbers are placed. Details of the mechanical construction of this can be found in [8, 13, 21].

This general construction led to an unfortunate side effect. There is space for 9 rubber spacers and a detailed investigation by [32] showed that the oscillation of section II and IV have a mechanical resonance at around $\nu \approx 650$ Hz when using 6 of the standard spacers. This has been remedied by using all 9 spaces with higher stiffness spacers, which pushed the resonance higher than 1100 Hz. This increased the phase stability of the oscillation and the mechanical stability of the whole system. Finally tension screws were installed to allow further tensioning of the rubber spacers without changing the height of the system. This allows for future tuning of the mechanical Eigenresonances without disturbing the alignment.

In the past there has been discussion of surface waves induced by forced mechanical oscillations of neutron mirrors. To exclude the influence of this a finite element analysis for the Bk-7 material with the true geometry as in fig. 3.4 and the clamps modelled as boundary conditions (fixed supports). The calculation was performed by Dr. Frederic Thomas from the Projects and Calculations Office of the ILL using Ansys 2022 R2. This resulted in tab. 3.1 for the Eigenmode frequencies of the first six modes.

This shows that the lowest mode is far away from any frequency used by the current qBOUNCE experiment. When addressing a transition, the mirrors are moved at $\nu \approx 1$ kHz with a displacement $a \approx 0.6$ μm. The response spectrum simulation results are shown in fig 3.5. This simulation shows that for the transition $|1\rangle \rightarrow |6\rangle$ any additional deformation of the mirror from eigenmodes can be ignored. When addressing a transition close to the eigenmodes in the future this geometrical effect should be reconsidered.

Table 3.1: Frequencies of the first few eigenmodes of the mirror geometry used in qBOUNCE . [33]

Mode	Frequency [Hz]
1	1757.7
2	2918.9
3	3862.0
4	3967.6
5	4723.4
6	6005.0
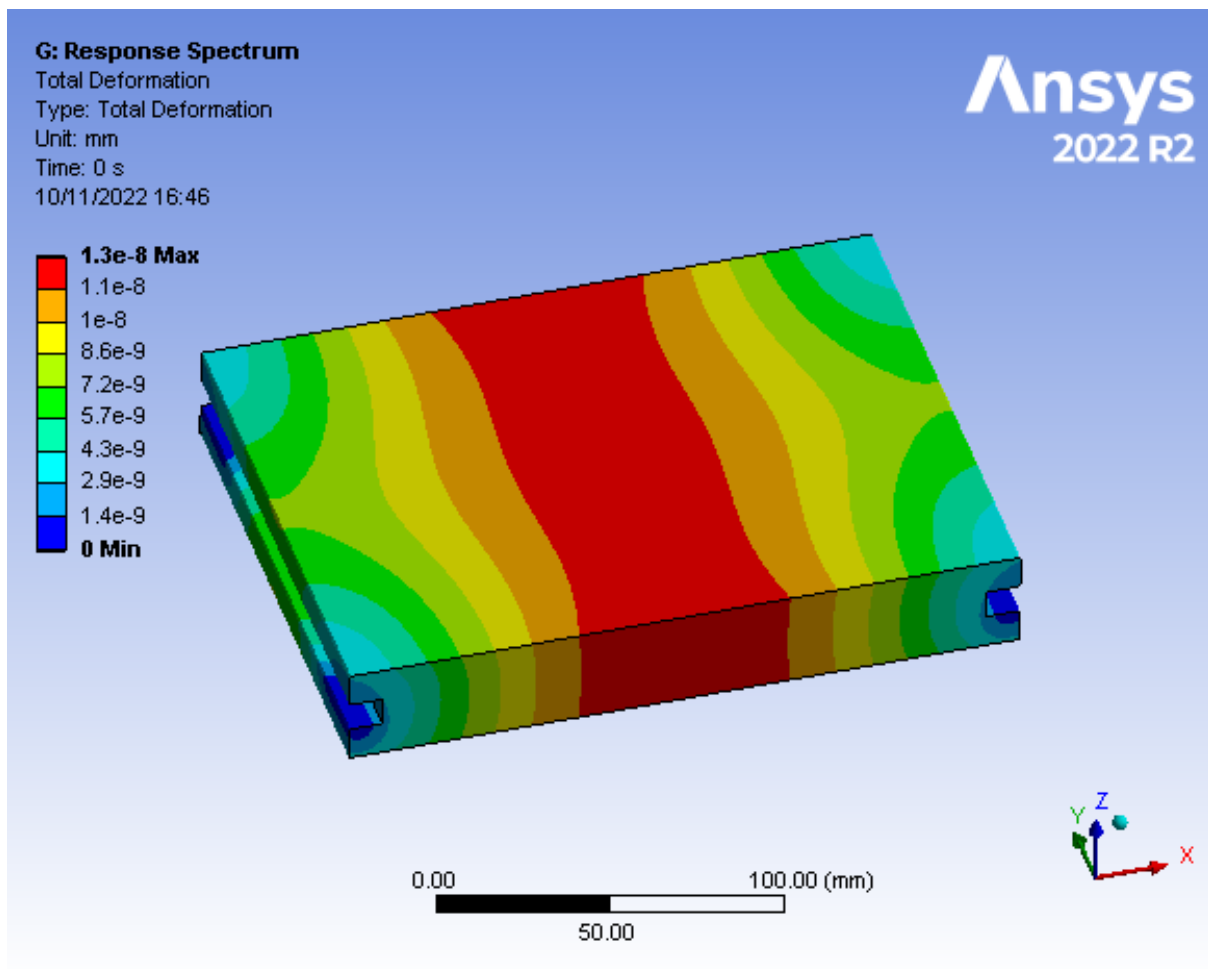
Figure 3.5: Deformation of the mirror surface when exciting an oscillation with frequency $\nu = 1\,\mathrm{kHz}$ and a displacement $a = 0.6\,\mu\mathrm{m}$ resulting in a maximum deformation from the oscillation $13\,\mathrm{pm}$, i.e. below the range of deformation that structural mechanics can address. In other words, the response spectrum analysis shows that one can neglect the deformation induced by the oscillation..[33]
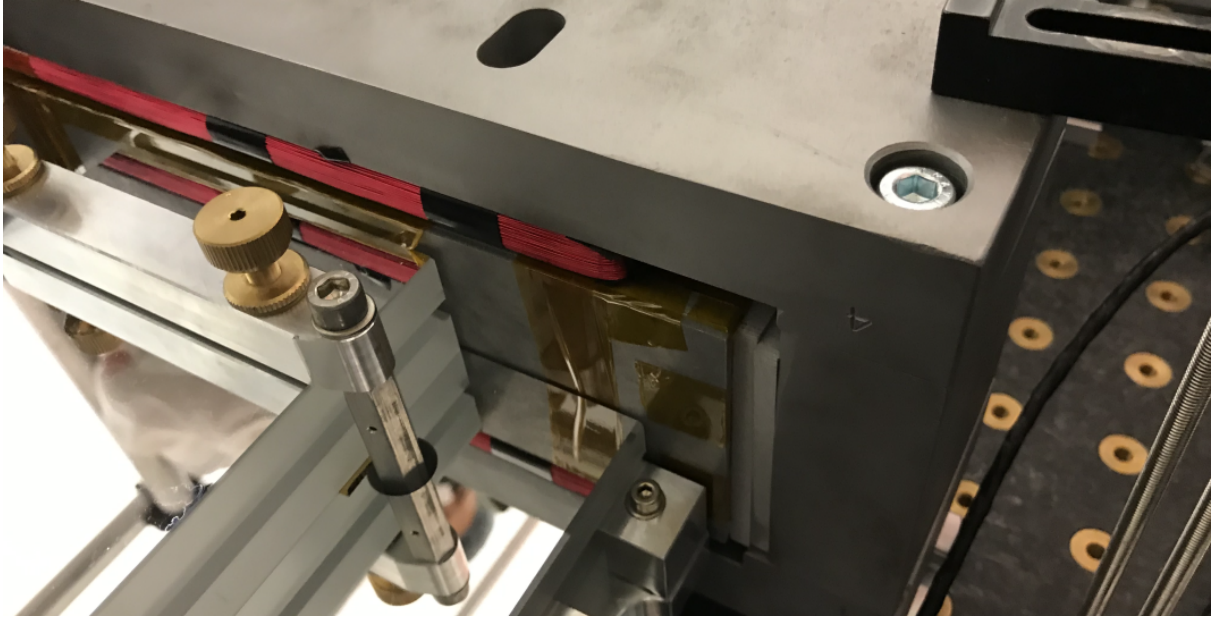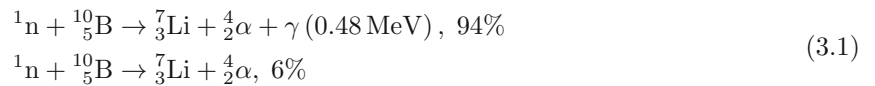
Figure 3.6: Spin dependent detector as installed for the spin dependent measurements.

3.3.2 Detector

The detector used by qBOUNCE was developed in group and has been optimised over the last 10 years [34, 35, 36]. The detector is a proportional counter with an entrance window using ^{10}B to convert neutrons to ions via the reactions

$$
\begin{aligned}
^{1}\text{n} + {}^{10}_{5}\text{B} &\rightarrow {}^{7}_{3}\text{Li} + {}^{4}_{2}\alpha + \gamma \,(0.48\,\text{MeV})\,,\ 94\% \\
^{1}\text{n} + {}^{10}_{5}\text{B} &\rightarrow {}^{7}_{3}\text{Li} + {}^{4}_{2}\alpha,\ 6\%
\end{aligned}
\tag{3.1}
$$

where 94% and 6% are the probabilities of the reaction. One of the generated α or Li ions then ionises the ArCO$_2$ mixture inside the detector. The optimisations over the years have resulted in an UCN detector with a total background count rate $r_{bg} \approx 5 \times 10^{-4}$ cps, meaning including electronic noise and the environment inside the reactor hall at PF2 while the reactor is operational. The exact value depends among other things on the gas mixture and reactor power and temperature. These quantities can change from one cycle to the next so the background is measured and used for the final rate calculation for each cycle separately as outlined in 5. Also [21] has separate analyses for more settings.

For the spin dependent detector the basic construction is the same, where the ^{10}B foil is also coated with Fe. This detector is placed inside an iron yoke with two magnetic coils. In fig. 3.6 the coil is visible in red. There is another coil at the bottom. By energising these the iron coating is magnetised and only one spin component is transmitted and detected. The characterisation and result of the polarisation efficiency of this detector is outlined in appendix C a detailed description and analysis of the measurements can be found in [37]. The product of the polariser and detector polarisability is $P_{\text{det}}P_{\text{pol}} \approx 0.78$ with a cut-off velocity of $v_{\text{cutoff}} \approx 7.7\,\text{m\,s}^{-1}$. This cuts out more than half of the spectrum as shown in fig. 3.11. In addition approximately half the neutrons will be discarded again by the spin selection. As will be shown in chapter 5.4.2 this leads to a base rate of $r \approx 3$ mcps and very long measurement times.

3.3.3 Magnetic field

Neutrons have no electric charge, but they have a magnetic moment. This is widely used for magnetic interactions and scattering as well as nEDM experiments. In case of qBOUNCE the magnetic moment is a property that has to be carefully managed in order to limit the influence on the experimental result.
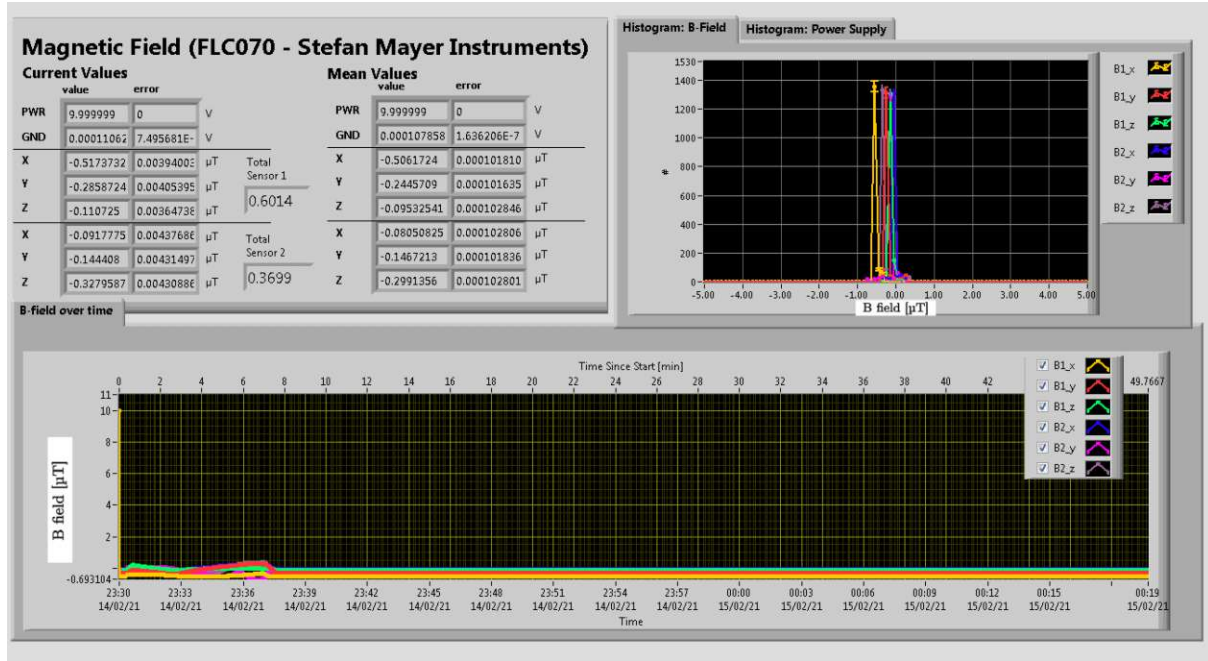
Figure 3.7: Bfield measurements during a measurement. The changing field at the beginning are due to the mapping of the Bfield sensors through the experiment.

In general the interaction of the magnetic moment $\hat{\mu}$ with a magnetic field B is given by

$$\hat{H}_{\mathrm{B}} = -\hat{\mu} \cdot B\left(\mathbf{r}\right) \approx -\hat{\mu} \cdot B\left(\mathbf{0}\right) - \mathbf{r} \cdot \hat{\mu} \cdot \nabla B\left(\mathbf{0}\right) \tag{3.2}$$

where the expansion in the last equation is valid close to $\mathbf{r} = 0$. For the z component this equation this gives an additional linear potential

$$\hat{H}_{\mathrm{B}} = -\hat{\mu} \cdot B\left(\mathbf{r}\right) \approx -\hat{\mu} \cdot B(0) - \hat{z}\hat{\mu} \cdot \partial_z B\left(0\right) \tag{3.3}$$

which is indistinguishable to a change in g in GRS. The details of this are discussed in 4.1.3. To limit the effect of any unwanted magnetic field, the vacuum chamber has been constructed with a two layer μ-metal shielding with a shielding factor of ≈ 80 of the Earths magnetic field. [13]. The magnetic field inside the chamber during the experiment is monitored using two FLC070 three axis flux gate sensors by Stefan Mayer Instruments. The static magnetic field is $B \approx 0.6\,\mu\text{T}$ and the highest value measured across a movement range of $\approx 30\,\text{cm}$ is $B_{\max} \approx 1\,\mu\text{T}$ as is shown in fig. 3.7. The varying field in the beginning of the measurement is the movement of the gantry for the capacitive sensors described in 3.3.6 for the mirror alignment. The sensors are located next to the neutron mirrors. The histogram in 3.7 shows all measurements for this dataset with a statistical summary in the table on the left. The current values of the two magnetic field sensors is shown in "Total Sensor 1/2". The two sensors are mounted at a distance in x of about $d \approx 30\,\text{cm}$ and they show comparable values for the magnetic field.

For investigations of a spin dependent change in the local acceleration of the neutrons qBOUNCE has two rectangular Helmholtz coils inside the chamber to apply a constant magnetic field. These have been used to set up a constant field of $\approx 100\,\mu\text{T}$ and GRS was performed in this field using a detector with a polariser in front [6]. The results can be found in 5.4.2.
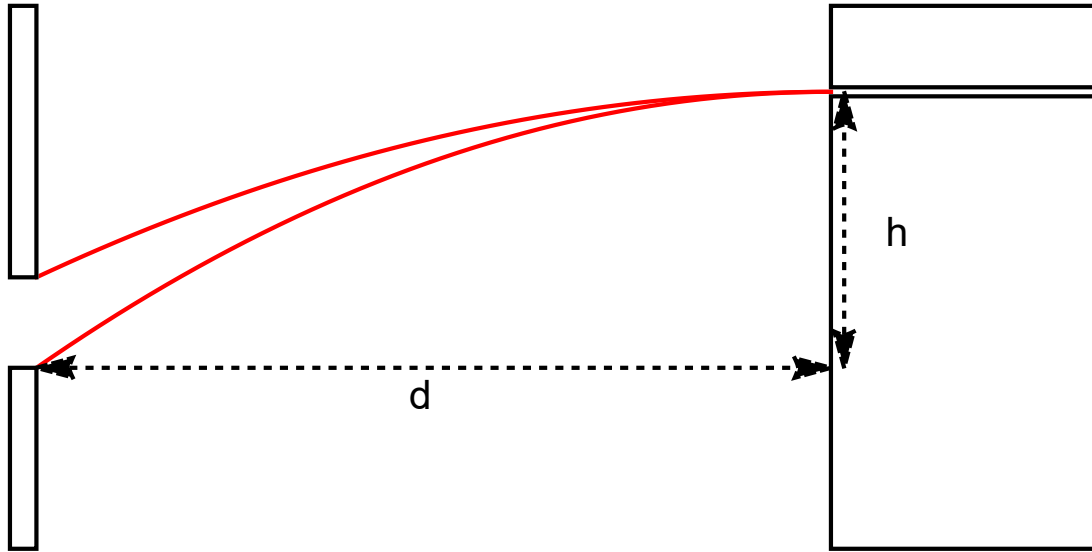
Figure 3.8: Basic setup for the determination of the velocity spectrum. This was previously used and described in [6, 8, 13]

3.3.4 Velocity Spectrum

To determine the velocity spectrum inside the experiment you can use two fundamentally different methods. Firstly the direct method, where you set the velocity interval and then the neutron flux through the experiment is measured. Doing this for a large value of subintervals gives you an estimation of the velocity spectrum. The second way is to measure the integral rate through the setup and determining the neutron rate corresponding to a certain slit height through subtraction. In 2019 the first method was use, whereas in the first cycle of 2020 the second method was used. This measurement was done since the beam guides were modified and maintenance of the Steyerl turbine at PF2 was performed in between these cycles. The basic setup used for these measurements can be seen in fig. 3.8. For a neutron traveling a distance d from the slit to the mirror, where the parabola has its vertex at the start of the mirror absorber pair and at a height h the flight parabola is given by

$$
\begin{aligned}
x\left(t\right) &= v_x t \ , \\
z\left(x\right) &= x\left(2d - x\right)\frac{h}{d^2} \ , \\
\Rightarrow z\left(t\right) &= t\left(2d - v_x t\right)\frac{h v_x}{d^2} = \frac{2h v_x}{d}t - \frac{h v_x^2}{d^2}t^2 \ .
\end{aligned}
\tag{3.4}
$$

Comparing with $z\left(t\right) = v_z t - g t^2/2$ gives

$$
v_x = d\sqrt{\frac{g}{2h}} \ ,
\tag{3.5}
$$

where in the setup $d = 159(1)\,\text{mm}$. The slit aperture and the state selector were placed behind each other, with an absolute height of the mirror surface at $h = 110.00(1)\,\text{mm}$, a slit height of $100\,\mu\text{m}$, and the detector was placed directly behind. Then the slit width was set to the height corresponding to e.g. [4;14] m/s. The neutron count rate was recorded. After that the lower blade of the slit was set up for [5;14] m/s, and so on. These measurements can be seen in fig. 3.9.

Bayes analysis

To determine the neutron rate for a specific velocity, the fact

$$r(a,b) = \int_a^b \rho(v)\mathrm{d}v = \int_a^c \rho(v)\mathrm{d}v - \int_b^c \rho(v)\mathrm{d}v, \tag{3.6}$$

was used. From this the quantity $\rho(v)$ can be estimated. In a simplistic first approach simply the difference of the measured rates divided by the velocity interval was used. The errors were then calculated using the standard sum of squares error propagation. The result of this can be seen in fig. 3.10 in blue. This naive approach is unsatisfying because it is clearly wrong. The first measurement point in 3.9 is lower than the second measurement point, this giving a negative value for the first point in 3.10.

To deal with this a statistically sound approach is provided by Bayes theorem. Assuming two independent measurements of neutron rates for two different velocity intervals r_a and r_b, with measurement times t_a and t_b and measured numbers of neutron n_a and n_b the likelihood for the observation of these events is given by

$$L(r_a, r_b | n_a, t_a, n_b, t_b) = \frac{(r_a t_a)^{n_a} e^{-r_a t_a}}{n_a!} \frac{(r_b t_b)^{n_b} e^{-r_b t_b}}{n_b!} \tag{3.7}$$

now reasonable assumptions about the parameters r_a and r_b have to be encoded in priors. Firstly both r_a and r_b have to be positive and secondly $r_a - r_b$ has to also be positive, provided the velocity interval for r_b is a subset of the interval for r_a. The full likelihood is now given by

$$L(r_a, r_b | n_a, t_a, n_b, t_b) = \frac{(r_a t_a)^{n_a} e^{-r_a t_a}}{n_a!} \frac{(r_b t_b)^{n_b} e^{-r_b t_b}}{n_b!} \Theta(r_a)\Theta(r_b)\Theta(r_a - r_b), \tag{3.8}$$

where Θ is the Heaviside step function. Introducing the new variable pair $x = r_a + r_b$, $y = r_a - r_b$ the likelihood is now

$$L(x, y | n_a, t_a, n_b, t_b) = \frac{1}{2} \frac{\left(\left(\frac{x+y}{2}\right) t_a\right)^{n_a} e^{-\left(\frac{x+y}{2}\right)t_a}}{n_a!} \frac{\left(\left(\frac{x-y}{2}\right) t_b\right)^{n_b} e^{-\left(\frac{x-y}{2}\right)t_b}}{n_b!} \Theta\left(\frac{x+y}{2}\right)\Theta\left(\frac{x-y}{2}\right)\Theta(y), \tag{3.9}$$

from which the parameter y can be estimated, which is the quantity of interest. By integrating out the variable x the posterior probability density for the parameter y can be obtained. From this, asymmetric errors can be obtained by choosing a constant probability density such that the integrated probability is $\sim 68\%$. Evaluating the measurements using this approach leads to modified expectations and asymmetric errors for the differential spectrum. The result can be seen in fig. 3.10 in orange. This shows that this correction influences mostly the first measurement point, all other points yield basically the same result as in the naive case. In table 3.2 the estimates and errors of the naive and the Bayes approach are compared.

Determination from first principles

For the use in the velocity averaging of the transition probability one has to sample the velocity distribution at multiple points. It is not easy to see which part of the velocity spectrum contributes how much to the final shape of the measured transition curve. Therefore it would be nice to have a simple model of the velocity spectrum. There are a few valid approaches that could be used for this: firstly just interpolating the measured rates to sample the spectrum at not measured values. A second approach would be to simply make a guess for a distribution. For example the general expectation would be some form of Maxwell-Boltzmann distribution, since the neutrons start out in thermal equilibrium with a moderator. The details of this are not clear, since geometric effects are very complicated in this case. Not even the correct dimensionality for the problem can be given, since the scattering of neutrons into the state selector is very sensitive to any velocity in the z direction. On the other hand the neutrons are much less constrained in x and y, so the space dimension should be a value between 2 and 3. In addition, the effect of the turbine is a scattering of neutrons to a lower velocity, but this scattering is not in any thermal equilibrium. It is simply elastic scattering off of the blades inside the turbine. Because of this it would be expected that a standard Maxwell-Boltzmann distribution can not be used for this purpose.

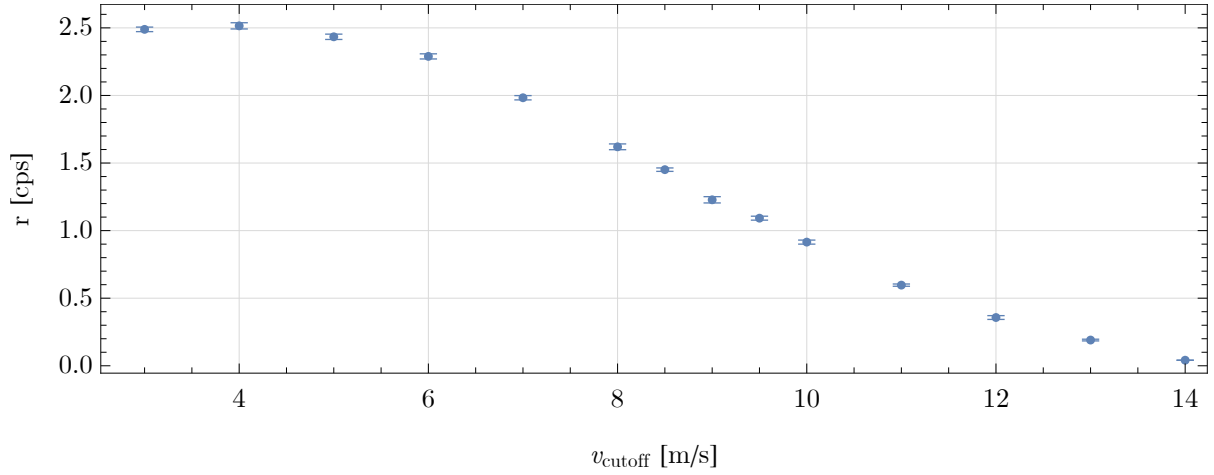Figure 3.9: Measured integral neutron transmission where the lower slit aperture is set to v_{cutoff} and the upper aperture to $14\,\mathrm{m\,s^{-1}}$
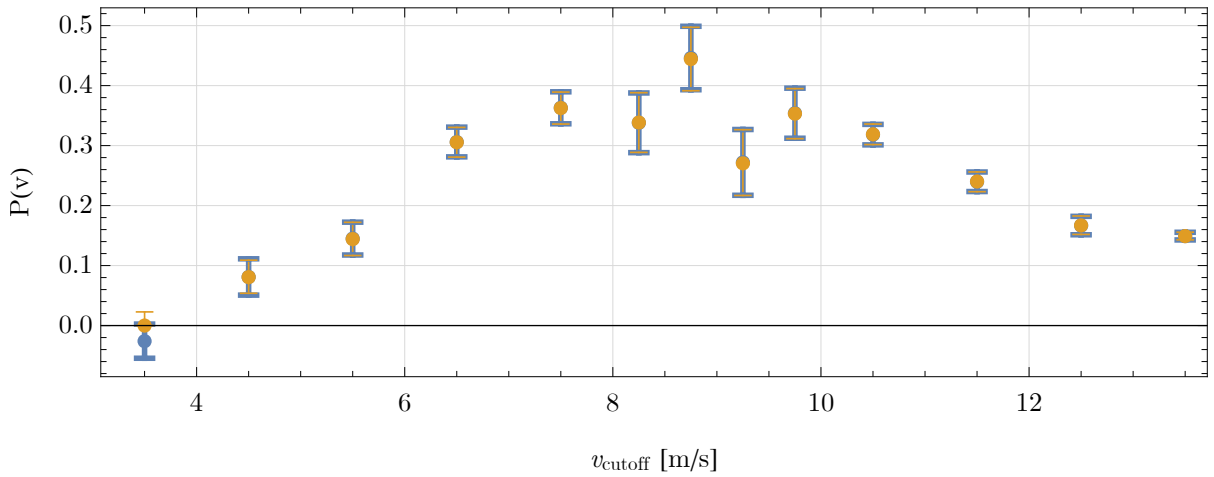

Figure 3.10: Resulting velocity spectrum from the integral measurement. In blue the result by naively subtracting different velocity measurements, in orange the result for the Bayes approach, correcting mostly the first point in the spectrum.

Table 3.2: Comparison of the result for the velocity spectrum using the naive approach and Bayes analysis.

v_{cutoff}	P(v) [naive]	P(v) [Bayes]
3.5	$-0.026(28)$	$0._{-0.}^{+0.023}$
4.5	$0.081(30)$	$0.081_{-0.027}^{+0.028}$
5.5	$0.145(27)$	$0.144_{-0.027}^{+0.028}$
6.5	$0.306(25)$	$0.306_{-0.025}^{+0.025}$
7.5	$0.363(27)$	$0.363_{-0.027}^{+0.027}$
8.25	$0.338(50)$	$0.338_{-0.05}^{+0.05}$
8.75	$0.446(53)$	$0.444_{-0.053}^{+0.053}$
9.25	$0.272(55)$	$0.27_{-0.054}^{+0.056}$
9.75	$0.354(42)$	$0.353_{-0.042}^{+0.042}$
10.5	$0.318(17)$	$0.319_{-0.017}^{+0.017}$
11.5	$0.240(16)$	$0.24_{-0.017}^{+0.016}$
12.5	$0.167(15)$	$0.167_{-0.015}^{+0.016}$
13.5	$0.149(6)$	$0.149_{-0.006}^{+0.007}$

Table 3.3: Results of a fit of a χ distribution and a Maxwell-Boltzmann distribution to the velocity spectrum. Statistically they are compatible, the data is not enough to differentiate between the two.

Model	v_0	N	d	b
Maxwell-Boltzmann	$2.790(426)\,\mathrm{m\,s^{-1}}$	0.030	2	$4.131(312)\,\mathrm{m\,s^{-1}}$
χ-like	$3.347(902)\,\mathrm{m\,s^{-1}}$	0.055	$1.704(759)\,\mathrm{m\,s^{-1}}$	$3.977(234)\,\mathrm{m\,s^{-1}}$

Nevertheless, keeping with the general idea of this, one possible function for the velocity distribution is given by

$$\rho(v - v_0 | N, d, b) = N(v - v_0)^d e^{-(v-v0)^2/(2b^2)} \Theta(v - v_0)\,, \tag{3.10}$$

where N, d, b and v_0 are the parameters that can be determined by a fit to the measured rates. This is a (shifted) χ distribution with $d+1$ degrees of freedom. For $d = 2$ this corresponds to a Maxwell-Boltzmann distribution. Fitting a χ and a Maxwell-Boltzmann distribution gives for the parameters tab. 3.3.
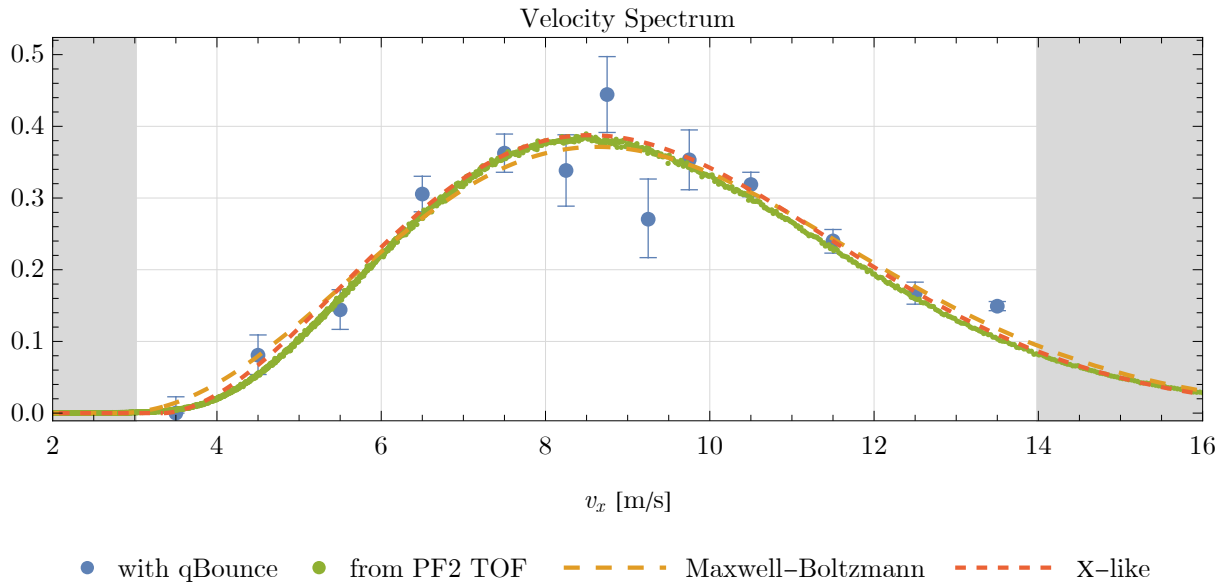
Figure 3.11: Velocity spectrum from measurements with qBOUNCE and from the PF2 tof spectrum in green. Fits for a χ-distribution and the Maxwell-Boltzmann distribution. The velocities in gray are cut off by the velocity blades. The specific interval used can be found in the corresponding sections to the measurement and changes for different measurements.

Another approach is to infer the spectrum directly from the spectrum of the turbine. This spectrum was determined by the PF2 instrument responsibles in the beginning of 2020 via a time of flight measurement and can be seen in fig. 3.2. Now the assumption that the probability per unit time to scatter inside the absorber is constant leads to an exponential decay. Using the transmission time $t = l/v$ and transforming to a probability distribution in v gives

$$\rho(v, a, v_0) = a \frac{e^{-v_0/v}}{v^2} \rho_0(v) \tag{3.11}$$

This prefers slow neutrons and suppresses fast neutrons. The proportionality constants can be determined again by a fit to the data. The three different approaches can be seen in fig. 3.11.

These results show that a naive approach is relatively straight forward for obtaining the measured spectrum. Statistically the measurement can not be used to differentiate between the two models since both result in a similar velocity distribution. For practicality reasons the modified Maxwell-Boltzmann result is used, since it gives a simple function for the spectrum. Numerical determination of the spectrum can be used from the TOF data, but gives no additional benefit. As will be shown in 3.5.2 the shape of the velocity spectrum does not need to be taken into account because the Ramsey transmission curve for the qBOUNCE experiment in its current realisation is very insensitive to the exact details. The main parameter of importance is the mean velocity, which determines the width of the fringe. All other effects seem to be of higher order. A more detailed analysis including the finite slit width was done in [8, 38]. A full quantum mechanical analysis of the scattering and determination of the velocity spectrum is given in [20].

3.3.5 Nano positioning stages for neutron mirrors

The neutron mirrors in qBOUNCE have to be aligned at the edges as close as possible. To do this it is necessary to be able to dynamically move the neutron mirrors. Furthermore the induced oscillations in section II and IV need to be applied. This is done using three axis positioning stages by Physik Instrumente (PI). The specific models used are from the P-5X8.TCD range of 3 axis piezo scanners where X gives the range $X = 2 : 200\,\mu m$ $X = 1 : 100\,\mu m$ and $X = 5 : 50\,\mu m$. They are rated for a push force of of $F_z \approx 50\,N$ and a pull force of of $F_z \approx 40\,N$. Depending on the range they have different intrinsic mechanical resonances with a load of 2.5 kg, with $\nu_{200\,\mu m} \approx 130\,Hz$, $\nu_{100\,\mu m} \approx 200\,Hz$, $\nu_{50\,\mu m} \approx 245\,Hz$. The whole mirror and holder combination has a weight of $m \approx 3\,kg$ and the vibration frequencies are $\approx 1\,kHz$. Because of this we use P-558 table for sec II and IV. They have the highest intrinsic stiffness. For an oscillation of the form $z(t) = a\sin(\omega t)$ the maximum acceleration is given by $\ddot{z}_{max} = a\omega^2$. For a typical $a \approx 0.5\,\mu m$ and $\omega \approx 2\pi 1000 s^{-1}$ used in qBOUNCE we have a maximum force of $F_{max} = 3\,kg \cdot \ddot{z}_{max} \approx 59\,N$.

Since we are using the piezos outside their intended range the oscillations were tested with different piezo stages with the conclusion that stiffer works better for our application. Because of this ageing is most likely accelerated and stability is not a given and has to be checked for each oscillation frequency. The active feedback of the piezo controllers is set up to allow the target oscillation without inducing additional PID ringing. This is done with the software provided by PI where intrinsic oscillation frequencies can be damped from the positioning PID. There are frequency transitions that can be addressed better and others not at all. The rough adjustment plate has up to 9 elastomer springs [39, 40] that compress to allow for height adjustment as described in 3.3.1. This introduces additional resonance frequencies in the system that have an effect on the stability of the PID. The stiffness of these rubber feet was chosen to be as high as possible to not disturb the intended frequency range. The 50 μm PI tables are able to compensate for this. While testing the oscillations it turned out that the piezo tables with higher ranges are not able to provide the necessary oscillation strength to address the transition $|1\rangle \rightarrow |6\rangle$ while working against the mounting rubber feet. Because of this section IV was replaced with a new 50 μm piezo stage. Additional tests were carried out to test the sensitivity to mirror alignment on the stage itself. To this end the mirror was placed 1 cm off the piezo axis and oscillations were induced. This did not have any measurable effect on the oscillation behaviour of the system.

3.3.6 Position measurement system for the mirrors

To provide accurate alignment of the neutron mirrors, their positions have to be checked. To do this capacitive sensors are positioned to the sides of the neutron flight path and on an additional reference mirror [41]. They are mounted to a linear stage [42] and can move across the mirrors in order to align the mirror positions to be parallel and without steps with respect to each other. They measure the height by measuring the capacitance between a sensor plate and the surface of the mirror indicated in 3.13 as dashed black lines. During the measurement campaigns in 2020 and 2021 there were 9 sensors installed as indicated in fig. 3.12.
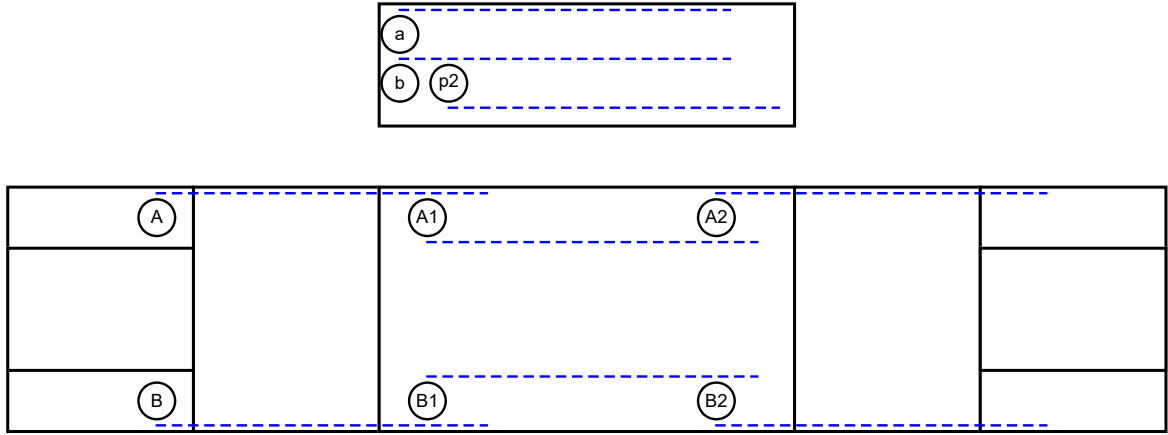
Figure 3.12: Layout of the capacitive sensors, the dashed blue lines indicate their movement range.

All capacitive measurements are relative to a reference point. This point is in general arbitrary, but all other height measurements are relative to this reference point. In the experiment this reference point is chosen at the left most point in fig. 3.12. The reference sensors are then used to correct for intrinsic movement of the mounting assembly and the linear stage. There are two separate corrections, first the height deviation and second the tilts of the whole assembly. A simplified sketch of this can be seen in fig. 3.13. If the reference mirror is perfectly flat, the reference sensors are supposed to be at the height indicated by the dotted line. Because of the movement of the MiCos stage the sensors have a different distance to the surface. To correct the measurement of sensor A, which is above an arbitrarily tilted mirror, firstly the height of sensor a z'_a is subtracted from all measurements resulting in the height corrected values $z''_A = z'_A - z'_a$ and $z''_b = z'_b - z'_a$ and $z''_a = z'_a - z'_a = 0$. Next the tilt angle is corrected by combining sensors a and b. The final corrected heights are given by

$$z_a = z''_a + z''_b \frac{0}{dab} = 0$$
$$z_b = z''_b + z''_b \frac{-dab}{dab} = 0 \tag{3.12}$$
$$z_A = z''_A + (z''_b) \frac{daA}{dab}$$

The sign in the equation for z_b stems from the fact that the sensors A and b are on different sides of the reference sensor a used as the height reference. This correction only corrects for tilt in one axis. To correct for tilt in the other axis a sensor in the orthogonal direction is used in a similar way. The result for sensor A is given by

$$z_A = z''_A + z''_b \frac{daA}{dab} + z''_{p2} \frac{dbA}{dap2} \tag{3.13}$$

and can be repeated for all sensors installed, taking care to choose the sign of the tilt correction in the right way. This z correction is equivalent to a rotation around the x- and y-directions to linear order in the rotation angles. In the xy-plane a rotation would lead to a shift of the position linear in the rotation angle, which is not the case here. An additional effect comes from the fact that the capacitance also changes with the tilt of the sensor. This results in a slope of $\neq 1$ of measured vs. actual distance and was eliminated by aligning the capacitive sensors. The whole correction procedure for the capacitive sensors can be found in more detail in [21].
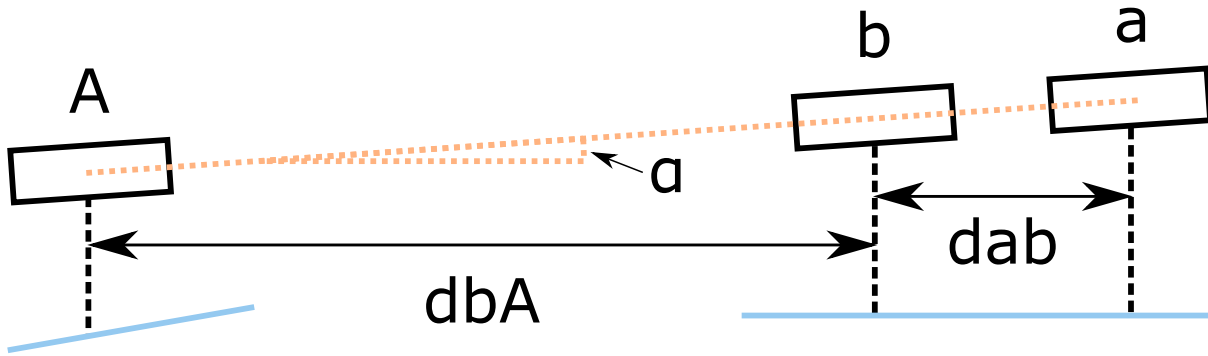
Figure 3.13: Sketch for the correction of a capsens measurement. The sensors b and a are above a fixed reference mirror. The sensor A is rigidly connected to a and b, but their whole holder could be tilted. This tilt angle α can be calculated from the height measurements of a and b. Then the sensor height A can be corrected to calculate the mirror position below A.

3.3.7   Step Control

For the alignment of the mirrors the capacitive sensors are moved along their whole movement range and the surface of the mirror is calculated. As a simple model a plane could be assumed, but the measured values from the height sensors do not follow straight lines. because of this a polynomial of second order is used. To avoid over fitting the degree is not made any higher. since there are only two measurement lines, the degree in the y direction can not be chosen to be higher than 1. The measurements of the capacitive sensors are given by $(x_k, y_k, z_k)^T$. The fit to the surface is done with a weighted least squares fit to a two dimensional surface in 3D space. The height z is given by

$$z(x, y) = \sum_{ij} a_{ij} x^i y^j \tag{3.14}$$

from this the weighted square deviation is calculated via

$$L = \sum_k \frac{\left(z_k - \sum_{ij} a_{ij} x_k^i y_k^j\right)^2}{\sigma_k^2} \tag{3.15}$$

where the index k ranges over all measurement points. The parameters a_{ij} are now chosen such that this quantity is the minimum. Requiring

$$\partial_{a_{lm}} L = -2 \sum_k \left(z_k - \sum_{ij} a_{ij} x_k^i y_k^j\right) \frac{x_k^l y_k^m}{\sigma_k^2} \overset{!}{=} 0$$

$$\Rightarrow \sum_{ij} \sum_k \frac{x_k^l y_k^m x_k^i y_k^j}{\sigma_k^2} a_{ij} = \sum_k \frac{z_k x_k^l y_k^m}{\sigma_k^2} =$$

$$= \sum_{ij} M^{lm,ij} a_{ij} = z^{lm} \tag{3.16}$$

$$M^{lm,ij} = \sum_k \frac{x_k^l y_k^m x_k^i y_k^j}{\sigma_k^2}$$

$$z^{lm} = \sum_k \frac{z_k x_k^l y_k^m}{\sigma_k^2}$$

where $M^{lm,ij}$ can be viewed as a matrix with (multi) indices (lm) and (ij). From this point of view the a_{ij} can be calculated via simple matrix inversion

$$a_{ij} = \sum_{lm} \left(M^{-1}\right)_{ij,lm} z^{lm}$$
$$\sum_{lm} \left(M^{-1}\right)_{ij,lm} M^{lm,no} = \delta_i^n \delta_j^o \tag{3.17}$$

These equations show that the a_{ij} are uniquely determined, so there is one extremal point in the space of possible a_{ij}. In equation 3.15 it can be seen that $L > 0$ and is unbound as the $|a_{ij}| \to \infty$. Therefore the extremal point has to be a global minimum.

Such a fit can be repeated for every mirror, such that the complete mirror geometry is reconstructed. Of course local deviations in between the capacitive sensors can not be reproduced. From the basic surface function the pitch α and roll β angles and the average height $\bar{z}$ can be calculated via

$$\bar{z} = \frac{\int_m z(x,y) \, dx \, dy}{\int_m dx \, dy}$$
$$\tan(\alpha) = \frac{dz}{dx} \approx \alpha \tag{3.18}$$
$$\tan(\beta) = \frac{dz}{dy} \approx \beta$$

where m is the mirror with the appropriate xy ranges. To avoid losses and unwanted transitions as much as possible two criteria have to be fulfilled: First there should be no height differences between the mirrors and second the edges of two mirrors that are next to each other have to be aligned. As described in sec. 3.3.5 the piezo stages can rotate around the x and y direction as well as change the height. Since the mirrors are not flat the alignment can not be achieved directly. First the average height $\bar{z}$ might be different than the actual height at the edge(s). This is the case especially for section II. This problem can be corrected by introducing an offset to the height which can be determined for every mirror. Secondly the roll angle is not unique. Since the surface is a polynomial in x, the roll angle of the starting edge and the ending edge are in general different. Because of this the best one can do is to align the edges of adjacent mirrors, without consideration of a possible twist. And lastly the pitch angle is also a function of the xy position of the table. This can be solved by averaging the height at the edges and calculating an effective pitch angle and using this for alignment.

The polynomial used for the correction was of the form

$$z(x,y) = a_{0,0} + a_{1,0}x + a_{0,1}y + a_{2,0}x^2 + a_{1,1}xy, \tag{3.19}$$

because the mirrors seem to be curved in the flight direction by measurements with the capacitive sensors. In the y direction, there are only two measurement points, so the highest possible degree of a polynomial is 1 in that direction. In principle higher order polynomials are possible but not necessary in practise and could lead to over fitting.

The first step in correcting the measured data is to subtract the height of sensor b in order to get the overall shift in height. After this has been corrected the heights of the sensor a and $p2$ are a measure of the tilt angle, and directly proportional to the height correction for the sensors over the main neutron mirrors. In order to correct the main sensors, the distances in daB and daA have been measured to within $\approx 0.1\,\mathrm{mm}$. From this the final corrected heights above the mirrors can be determined. The coordinate system is chosen such that the x axis starts at the left edge in fig. 3.12. Now the Offsets have to be determined for the sensors $A1$, $A2$, $B1$ and $B2$. Section I is aligned by hand to $h = 110.00(1)\,\mathrm{mm}$ relative to the surface of the granite table and never moved. This is used as the absolute reference height to which everything else is aligned. Therefore the sensors A and B are used as reference sensors. To correct $A1$, first the overlapping measurements in x of A and $A1$ are selected and a fit to the measured surface is performed for both sensors. From this the average height of $A1$ can be shifted as to correspond to the average height of A in this section. The averaging is necessary, since the measurements do not agree with each other as can be seen in fig. 3.14.
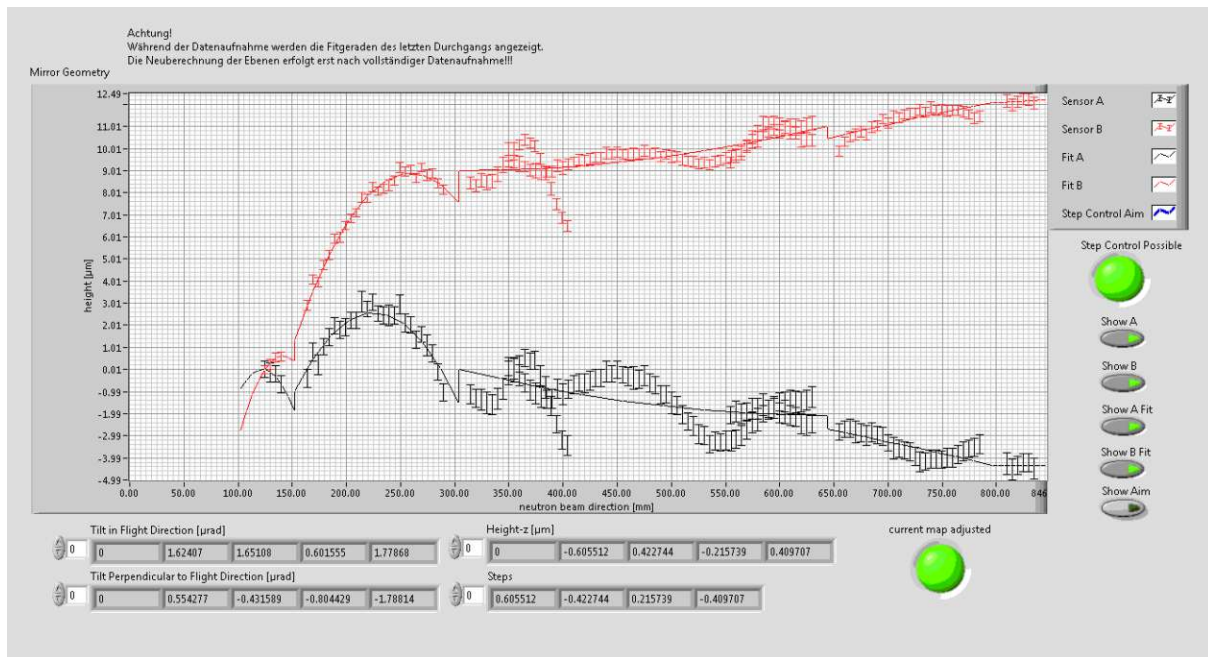
Figure 3.14: Example of a correction map used for mirror alignment. From this the steps between mirrors are corrected and a reference to adjust for temperature drift is taken.

The reason for this discrepancy is not known, a plausible cause is a difference in wire tension of the two sensors, leading to a different measurement response. Exchanging the sensors installed in positions A and $A1$ does not change the picture, so it is independent of the sensor but instead position (on the gantry) dependent. Since the sensors A and $A1$ lead to drastically different surface estimates even when they are above the same mirror parts it is also unlikely to be a real surface feature. The sensors A and B are furthest away from the vacuum feed through, therefore the cables have a higher tension in general than the cables for the other sensors which could, in part, explain the effect. Another possibility is a different cable path and therefore interference by capacitive coupling for the different sensors along the gantry. Modification of the mounting and to the ground connection layout in the setup was not able to change this general behaviour.

Now sensor $A2$ can be shifted with the corrected dataset for $A1$ and the measurement line B can be reconstructed in a similar fashion resulting in the dataset for the complete surface of all mirrors. An example for the result of this can be seen in fig. 3.14. The x range is split in separate mirrors, and the least squares polynomial fit for each surface is displayed as a solid line. The main reason for using a second order polynomial in x is the measured shape of section II. There is a clear trend towards a paraboloid shape that can not be reproduced by a simple planar fit. In addition, an overall twist from the fit is observed, indicated by the non parallel lines of the final surface functions, which can be introduced by an interplay of the actual shapes of the reference mirror and the experimental mirrors and their relative alignment as well as the previously mentioned capacitive sensor effects. The error for the absolute height from $x = 0$ m to $x = 0.948$ m, i.e. the whole length for all five regions has been measured to be accurate to within $\Delta z < 2$ μm. The final absolute error is likely on the order of ≈ 5 μm when including the global surface of the granite table used for the measurements. The step size between the sections was determined to be $\Delta z < 0.5$ μm using the linear gages described in [21]. With an improved reference system this overall procedure can be used for more accurate alignment in the future.

3.3.8 Frequency standard

We introduced an atomic clock in September 2020 to the equipment. This was done to eliminate all systematic errors that could arise from equipment that generates an intrinsic frequency. The two main sources for these errors are the interferometer and the function generator providing the signal to the

piezo tables. It is an SRS FS740 10 MHz GPS Frequency Reference [43] with a Rubidium time standard. It has a calibrated frequency standard with a 10^{-12} short term stability. Due to the location inside the reactor building it is not possible to synchronise the clock with GPS satellites. A second atomic clock from the PANEDM collaboration was used as a comparison device. This clock is usually synchronised to the GPS satellite time standard and was moved to the qBOUNCE experiment to take a direct comparison measurement. The FS740 has a direct BNC input for frequency measurements. The 10 MHz output of the PANEDM clock was fed into this port and the frequency was determined. The relative error from this measurement was $\delta = (\nu_{\text{panedm}} - \nu_{q\text{Bounce}})/\nu_{\text{panedm}} \approx 10^{-10}$. This is the absolute systematic error that is introduced into the system from the clock. As was shown in 3.3.9 this is orders of magnitudes less than the accuracy to which the oscillations can be measured. In addition the resolution of the function generator is 1 mHz which is $\Delta\nu/\nu > 10^{-6}$ for the frequencies used in the current GRS for the transition $|1\rangle \rightarrow |6\rangle$.

3.3.9 Optical oscillation monitoring

There are two laser interferometers mounted in qBOUNCE which fulfil two different purposes. The first one is called the "internal" interferometer. It is mounted on the granite table inside the chamber and therefore is influenced by the oscillations of the mirrors. There is a linear stage that can move the mirrors that reflect the laser beams. This can be used to move the interferometer beams over the whole setup to characterise the vibrations of the mirrors. This was done in order to exclude the possibility of higher order oscillations of the piezo stages see [13]. This is only possible for a limited number of oscillation settings since there are mechanical vibrations present in the setup. If the mirrors oscillate with a mechanical resonance of a mirror holder, the mirror oscillates at the same frequency as the neutron mirror. This shifts the measured phase of the mirror surface. This effect has been investigated by [32, 44].

To perform Ramsey like measurements it is crucial to be able to determine the frequency and the phase of section II and sec. IV as precisely as possible. Therefore a second interferometer was installed, which is mounted to the vacuum chamber and not the granite. This has been explained in [13]. Because of the independent mounting of this second interferometer it decouples from the oscillation of the neutron mirrors and it can be used to measure the frequency and the phase of the oscillating mirrors independently. This is necessary to exclude systematic errors when setting up the oscillations. In case there is some mechanical resonance influencing the granite or any other system used during a Ramsey measurement, the external interferometer is able to correct for this.

The interferometer is triggered by a signal generated by a Tektronix AFG. The sampling frequency used was 10 kHz to sample the movements of the mirror surface. An example for a measured signal from the external interferometer can be seen in fig 3.15. The oscillation frequency here was $\nu \approx 1$ kHz.

As can be seen from the raw signal there is a high amplitude signal present with a low frequency. In addition there is an intrinsic oscillator that provides a signal even without a moving target mirror, causing a slight beating in the main signal in figure 3.15. The full frequency response is shown in figure 3.16 where the internal oscillator and low frequency noise is present. Because of these unwanted signals in the data, the raw signal is filtered with a bandpass filter. After this the resulting signal was analysed with a sine fit and the amplitude is extracted. As was shown in chapter 2.5 the relevant part of the system is not quite the oscillation amplitude a but the oscillation velocity $a\omega$. From the result of the sine fit, this velocity can be extracted from the measured signal. This is done for both oscillating mirrors. The phase between section II and IV is then determined. This is done by calculating the best fit frequency of both combined signals and extracting the phase offset at that frequency. This has to be done since the fits for the two signals never agree perfectly, but the phase has to be determined at the same frequency for both mirrors. Tests within the setup have shown that these differences can be on the order of 20° if the frequency is off by a few mHz. This can be readily checked, since in that case there is a large offset between the function generator setting and the measured phase offset. Overall at the combined best fit frequency the setting of the function generator and the measured phase offset from the interferometer agree to within $\pm 0.5°$. This has been checked at every oscillation frequency. There are frequencies, especially close to the mechanical resonances of the mirror sandwich, where the phase is much less stable. These frequencies have been excluded from measurements for now, since the settings can not be maintained. This was one of the practical reasons to change the main transition from $|1\rangle \rightarrow |4\rangle$ to $|1\rangle \rightarrow |6\rangle$.
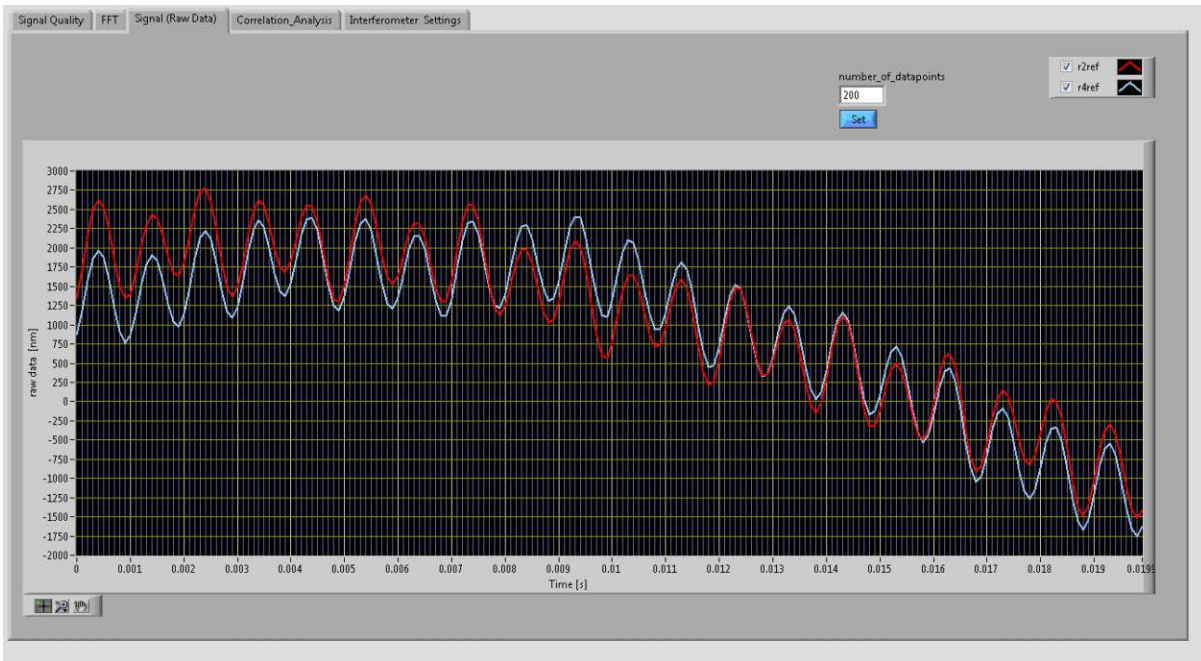
Figure 3.15: Raw data output from the external SIOS interferometer used to monitor the oscillations. This interferometer is decoupled from the experimental baseplate. A large amplitude vibration can be seen by the overall drift, and the internal reference mirror can be observed by the slight beating of the $\approx 1\,\text{kHz}$ signal.
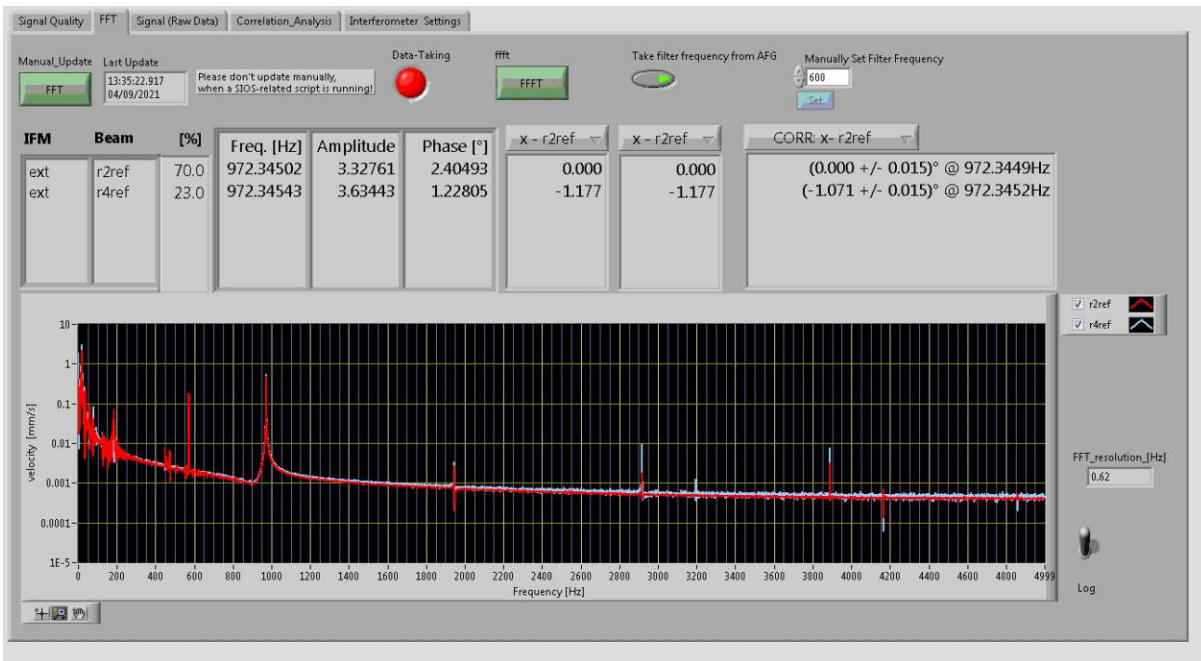

Figure 3.16: Fourier transform of the measured sine curve. The peak at $\nu \approx 972.345\,\text{Hz}$ are the oscillating mirrors. At $560\,\text{Hz}$ the internal reference mirror of the interferometer is shown. The high amplitude signals at low frequencies are due to background vibrations and lead to the large scale oscillations in 3.15.

3.3.10 Arbitrary Function Generator

There are two function generators providing the main signals necessary for the *q*BOUNCE experiment. They are both Tektronix 3102 [45] function generators, one bought in 2010 and the other in 2017. The first one provides the two piezo tables of section II and section IV with the sine signals for the oscillation. The second one is used to generate the sampling frequency for the interferometers. This is done because the SIOS interferometer uses an intrinsic sample rate that can not be changed arbitrarily. Care has to be taken to select a multiple of the base frequency of the SIOS clock. This can be a source of error, because the SIOS can not provide feedback to the measurement program which frequency is really set. To avoid this, the AFG generates a clock with the desired frequency. They are both locked to the Rb clock. With this the frequency can be set to within $\approx 10^{-6}$ at $f \approx 1\,\mathrm{kHz}$, limited by the $1\,\mathrm{mHz}$ resolution of the function generator.

3.4 Control Logic

3.4.1 Requesting Neutrons

To start a measurement neutrons are requested and the turbine provides a veto signal once it is ready to move to the UCN beam port. Furthermore it provides logic signals which can be configured to provide control of the experiment. Within *q*BOUNCE there are multiple distinct stages that determine the proceeding of the experiment. The general configuration of these signals can be seen in fig. 3.17. Each subsection has a specific purpose in the experiment. The logic signals generally control the following aspects: S1 activates the vibration of the mirrors, S2 gates the detector for actual measurements vs background, S3 signifies the start of the veto signal, S4 separates background from actual neutron measurements with the detector and S5 signifies the time after the measurement.

Filling

The turbine provides a veto signal and S3 goes from low to high. After ≈ 5 s the capacitive sensors take a measurement and adjust the mirror positions to account for temperature drift. In the first cycle the mirror position is recorded and used as a reference setting for all future settings (only for sections II and IV). The turbine moves the switcher to the UCN beam port.

Cleaning

S1 goes from low to high, which activates the output of the function generator so the mirrors start to oscillate. Also the CapSens start taking measurements every 15 seconds to be able to observe a temperature drift over time.These measurements are potentially much less accurate than the ones in the filling stage, but can be used for a characterisation of the drift. This is because these measurements also take place while the sections oscillate to address a transition. Neutrons start to arrive at the detector, but they are neither counted as "real" measurement neutrons, nor as "background" neutrons because S4 is active. This timeslot is necessary for the mirrors to reach a stable oscillation state and for the relatively slow neutrons to propagate through the whole setup. After ≈ 7 s the interferometer takes a reference measurement to check that the mirrors are oscillating and the settings (amplitudes and phases) of sec II and IV are correct.

Storing

S2 goes from low to high and S4 from high to low. S2 gates the detector so it adds the neutrons to the "real" measured rate. The CapSens keep measuring while S1 is high.

Storing A and Storing B

Neutrons are still arriving at the detector but they are counted as background. The outputs of the function generator are turned off. The oscillations of the mirrors die down and they return to their starting positions.
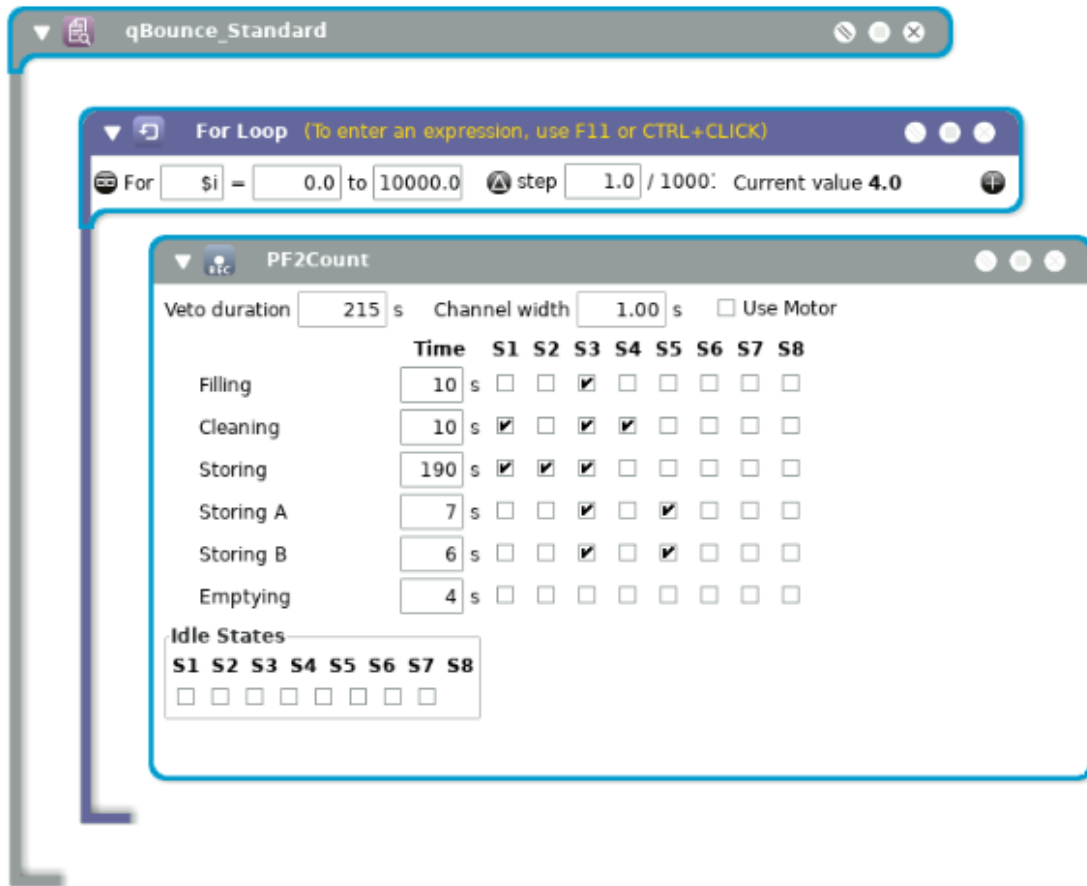
Figure 3.17: PF2 logic signals controlling the experiment during the shared mode of the neutron beam under which PF2 operates.

Figure 3.18: Example of the parameters used for the function generator. These are calibrated and then used to program the measurement devices.

Emptying

The logic signals S3 and S4 go from high to low. This is done to provide a S3 signal that is low in case no other experiment is requesting neutrons. If this were not included, the signal S3 might not go low (depending on the timing of the logic signals vs ADC timing of LabView). This would cause the CapSens correction in the Filling stage to not work for some cycles, since it is triggered by a S3 low to high transition.

3.4.2 Measurement Queue

The main measurements of qBOUNCE are controlled by the LabView script measurement_queue.vi. In general it works in multiple stages to set all parameters of function generators and to control specific events described in sec. 3.4.1. It operates by importing a table from a file that contains information for a specific measurement point. It sets the function generator frequency, voltages for channel 1 and channel 2, whether or not the function generator should be turned on during measurements, the standard deviation for the measurement, the phase between the two sinusoidal voltage outputs and the direction for the guide field in case spin dependent measurements are taken. The settings are obtained by tuning the output of the function generator in such a way that the desired oscillation amplitude and phase is reached. For example, if you want to oscillate the mirrors at $\nu = 972.345$ Hz with a maximum velocity $a\omega = 3$ mm/s and a phase $\varphi = 0$ ˚, you set up the function generator voltages and phase in such a way that the interferometer measures the desired oscillations of the mirrors. These settings are then added to a text file. This calibration step is automated with a script that automatically adds the necessary information to the file with the measurement table. It also adds additional information such as target vs. measured velocities and phases. Two examples of this can be seen in fig. 3.18.

Each measurements starts out with a map of the whole setup that calculates the steps between mirrors and minimises them. This is described in ch. 3.3.7. After this, a reference measurement is taken with the capacitive sensors, to adjust for temperature drifts of the piezo stages before the following cycles. Then the experiment waits for a veto signal from the turbine as described in the previous section 3.4.1. When the veto signal is high, there is a 10 second delay in which the capacitive sensor measurement is taken to correct a possible drift from the reference measurement. After that the neutron mirrors start oscillating (if the afg_via_veto flag is set) and the PF2 timing runs through. After the veto signal goes low again, the function generator is turned off, therefore turning off the mirror oscillation. Then the neutron detector is stopped until the veto signal is high again and the whole process repeats.

This whole process is repeated until the measurement error of the neutron count rate is lower than the set value from the table file. Afterwards the measurement is written to file and the function generator is set to the next values in the queue table file, and the whole process starts again from the step control script. A flow chart of this whole procedure can be found in fig. 3.19. After the initial calibration of the desired measurement points was performed and has been added to the queuefile the experiment runs automatically. This system is stable enough to run unsupervised for at least 3 weeks.
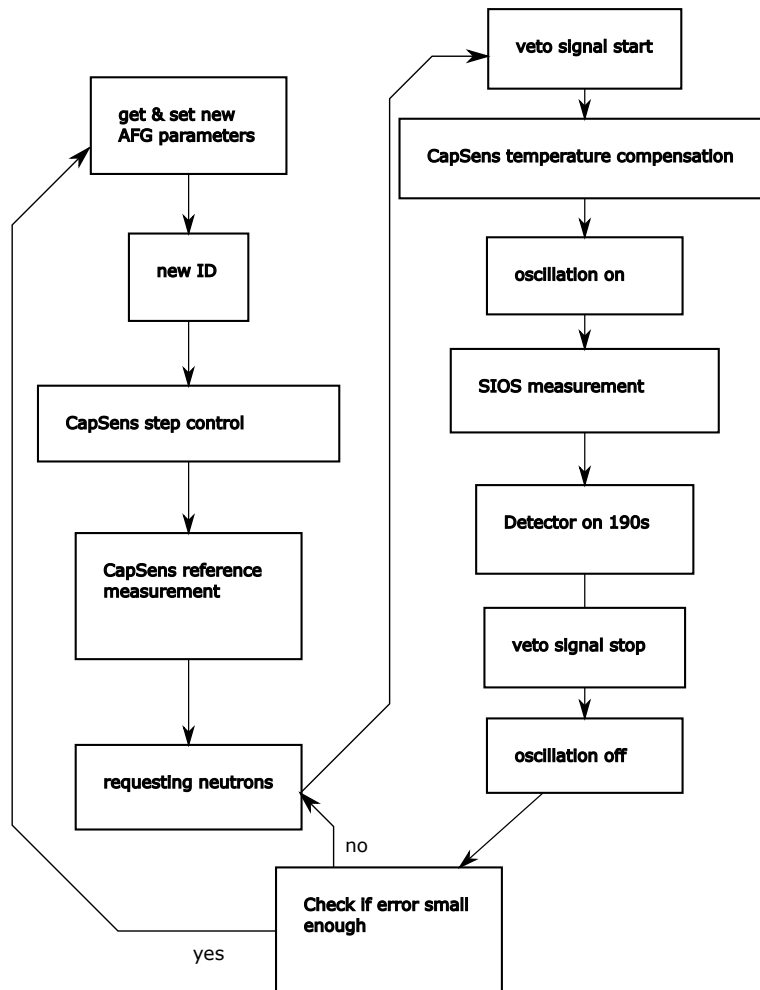
Figure 3.19: Measurement flowchart which steps happen during the measurement period.
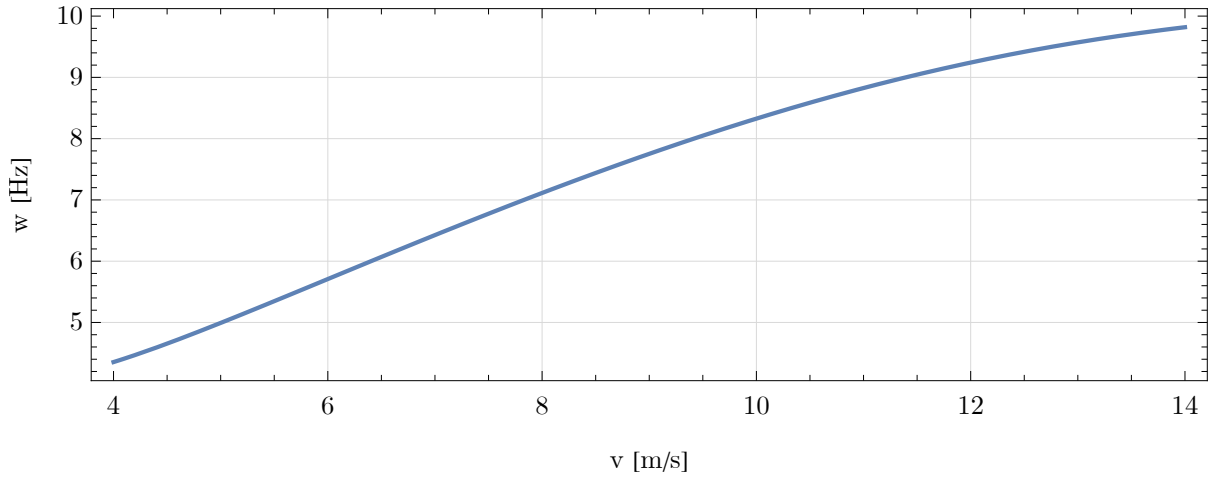
Figure 3.20: Full width at half maximum for the transition between two states.

3.5 Measurement Strategy

3.5.1 Expected $a\omega$ for a $\pi/2$-flip

Since the velocity spectrum is not know sufficiently well, the theoretical vibration strength for a $\frac{\pi}{2}$-pulse can not be determined. Therefore it is determined by increasing the oscillation strength $a\omega$ of the mirrors at the transition frequency. This would result in theoretical curves that can be seen in 3.21 for different velocities. The lines not reaching 0 result from the velocity averaging, whereas the ones going to 0 are from using only the mean velocity. The averaging lowers the contrast of the interference and changes the location of the optimal $a\omega$ for larger velocity intervals. The transmission recovers when the phase between section II and section IV is set to 180°. The ideal curve seen in this plot is spoiled by introducing multiple states. Including 30 gravity states leads to a decrease of the 180° curve for higher vibration strengths. This can be heuristically explained by higher order transitions in addition to the targeted one. In addition to that a non ideal vibration of the mirrors can be inferred from the failure of the recovery at 180°. In addition to that the recovery shows that the propagation of the neutron wave function along the mirror is a coherent evolution of the wave function. The recovery of the wave function is a purely quantum mechanical phenomenon which can not be explained by classical bouncing point particles. This has been shown by Montecarlo simulations in [13]. This also clearly shows that the coherence of the neutron wave function in GRS states can be preserved over a macroscopic distance of $\approx 1\,\mathrm{m}$ or a time of $t = \frac{1}{10} = 0.1\,\mathrm{s}$.

3.5.2 Width of a Ramsey fringe

From the theoretical function for the Ramsey transition given in 2.38 the full width at half maximum (minimum) for the velocity averaged transmission can be calculated. Starting out with the formula for the width

$$w = \frac{1}{2\left(T + \frac{\pi}{4}\tau\right)} = \frac{v}{2\left(l_{III} + \frac{\pi}{4}l_{II}\right)} \ , \tag{3.20}$$

and averaging it with the velocity distribution $\rho(v)$ from 3.11 the expected width is determined by the mean velocity $\bar{v}$.

$$\bar{w} = \frac{\bar{v}}{2\left(l_{III} + \frac{\pi}{4}l_{II}\right)} \tag{3.21}$$

which allows us to determine the expected points of the highest slope of the transition curve. In particular this also shows that the width of the Ramsey curve is determined solely by the velocity spectrum and the lengths of the section and not by the transition that is addressed. In principle a higher relative
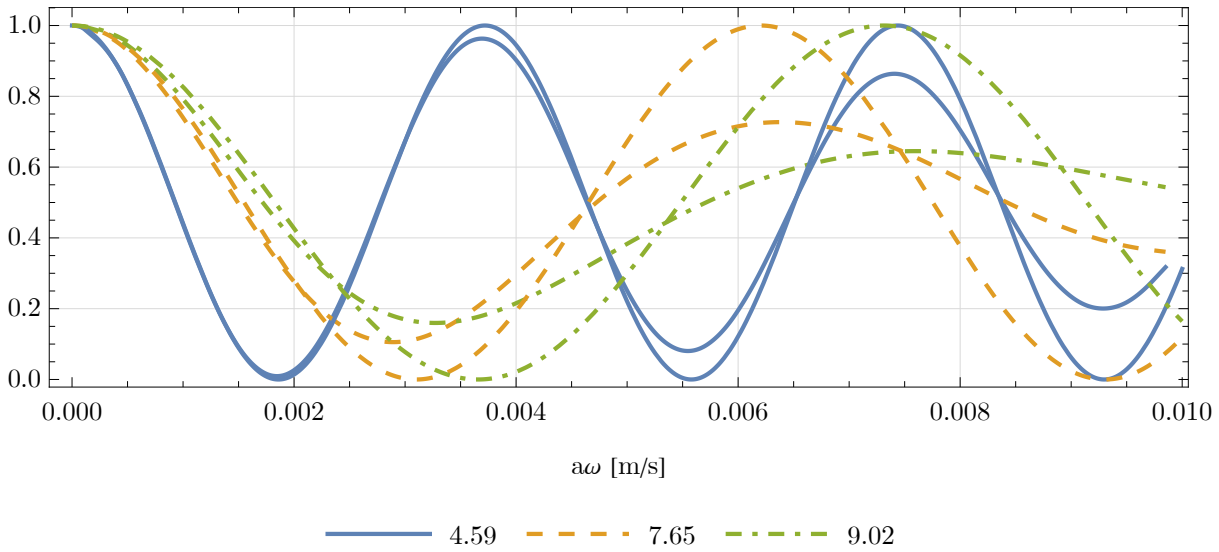
Figure 3.21: Velocity averaged transmission function with dependence on the vibration strength. In the legend the mean velocity for the different curves is given. The curves going to 0 are the non velocity averaged curves where the mean velocity was used.

accuracy could be achieved by simply addressing a higher transition. In practise this is not possible since the piezos can not oscillate at arbitrarily high frequencies. The system has been shown to be able to reach frequencies up to $\approx 1\,\text{kHz}$. In the third cycle in 2021 the transition $|2\rangle \to |8\rangle$ has been successfully addressed, which has a theoretical transition frequency of $1006\,\text{kHz}$. Higher oscillation frequencies were not tested, since the power consumption of the piezos increases as the oscillation frequency goes up. This causes the piezos to overheat and to shut down. Historically it was observed that this happens with $\approx 60\,\text{W}$ within one 190 second measurement interval. The power at $1\,\text{kHz}$ was $P \approx 52\,\text{W}$ and higher oscillations were not tested.

3.5.3   Contrast of a Ramsey fringe

Similar to the width, the depth of the Ramsey curve can be estimated. This is not as straight forward as in the case of the width, since the drop in the Ramsey curve is given by a complex function. I use the term contrast for the value

$$c = \frac{r_{max} - r_{min}}{r_{max}} \ . \tag{3.22}$$

This gives the percentage drop from the maximum possible value of 1. At resonance the value of the Ramsey curve for the transmission probability can be calculated from 2.36 for a single velocity.

$$P(|p\rangle \to |p\rangle) = \cos\left(a\omega V \tau\right)^2 = \cos\left(a\omega V \frac{0.152}{v}\right)^2 \tag{3.23}$$

where τ is again the interaction time, for $q\textsc{Bounce}$ $\tau = 0.152/v$ since the length of the interaction region is $0.152\,\text{m}$. The comparison of the single velocity case with the averaged case can be seen in 3.21.

This shows a few important features: The vibration strength for the ideal excitation (highest drop in count rate) does depend on the velocity interval used. The height of the minimum changes by $\approx 10\,\%$ over the whole measured velocity spectrum. Comparing the single velocity function with the velocity averaged function shows that the oscillations with increasing vibration velocity $a\omega$ decreases from the initial value of 1. This decreases the achievable contrast for the theory function with increasing vibration strength. This is intuitively clear, since more and more single velocity curves contribute and their phases at a single point drifts apart the higher the vibration strength. Ideally one is in the first minimum to

get the highest drop in count rate. Because of this the necessary vibration strength is measured with the experiment. In addition the achievable accuracy for a transition frequency depends on the drop in count rate, so this parameter can be optimised to reach the highest final accuracy. The result of such a velocity averaging can be seen in fig. 3.21. This function describes the ideally achievable contrast.

3.5.4 Transitions

In order to address a specific transition, multiple components have to be set up. The vibration strength for the $\pi/2$-flip in the ramsey case, the frequency for the specific transition and the phases between section II and IV. After that, in order to follow the central idea of the qBOUNCE measurement scheme described in chapter 2.6, the width of the transition needs to be known. For this the theoretically calculated width has to be used, since in the beginning the precise width of the transition is not known. This is because the theory giving the width and amplitude in the two state case is only an approximation. In practise it turns out that the theoretical width is a rather good approximation for the real width and therefore not much tuning has to be done. For measurements of a single transition frequency using the 6-point method these values can be tuned to give optimal statistics.

As a general approach the parameters of a measurement are chosen by first calculating the frequency of a transition from 2.10 with the values from 2.1. The width of a general transition from 3.5.2 is used to calculate the width of the resonance. This has to be done only once for each velocity setting. If the velocity blades are not changed, this width is the same for all possible transitions (with the exception of multi state effects). The vibration strength can be calculated from (2.38) with the mean velocity.

This are the reference parameters for the $a\omega$ sweep. In the measurement oscillation strength $a\omega$ is increased from 0 to the calculated value at the theoretical transition frequency in order to determine the optimal vibration strength, if possible. After this is done, the optimal strength is fixed and the frequencies are set up in a grid with a step size of the half width at half maximum. For a single transition there are points in the center and in the right and left slope of the Ramsey fringe, each with 0° and 180°. Repeatedly measuring these six points leads to the highest measurement accuracy. The measurement time can be optimised, since the center of the fringe contains no information of the position of the fringe, whereas the slopes do not contain much information about the drop. If only the slopes were measured, there would be no confirmation that the fringe actually exists since all points lie at the same measurement rate. If only the center is measured, only the height of the dip is known but not the position. Therefore both are necessary and in an ideal case, emphasis is put on the slopes to get the highest possible accuracy.

Since in fact we do not know the precise position of a possible transition, the theory values from the two state system are used. All deviations from this are due to effects not present in the naive two state secular approximation. When doing a frequency sweep, one never has to worry to miss a transition: the transition width between gravity states is independent of the neutron states, or energies, used in the transition with a $\pi/2$ flip. Therefore if the frequency grid is smaller than half the width, no transition of GRS states will be missed. This is particularly useful for investigating "new" physics. The parameter probed is the coupling strength V that determines the properties of the transition, which is for pure linear gravity independent of frequency.

Introducing any specific model for the relationship between wave function and coupling of the states in GRS via $V_{pq} = \int \psi_p \partial_z \psi_q \mathrm{d}z = \frac{\hbar^2}{2m_n(E_q - E_p)} \left(\psi_p'(0)\psi_q'(0) + \frac{\hbar^2}{2m_n} \int \psi_p \psi_q \partial_z V(z)\mathrm{d}z \right)$ from the general result A.10, with the states determined by the potential $V(z)$, these quantities are related. With this models can be readily excluded from given measurements. In principle the experiment does not have to be modified to investigate different models, only the specific frequencies and vibration amplitudes for a measurement may vary. GRS investigates all models of bound states equally and not one specific model exclusively. This concludes the discussion of the general experiment and systematic effects are investigated in the next chapter.

Chapter 4

Systematic Effects

The results of the measurements presented in chapter 5 highlighted the importance of an in depth analysis of systematic effects. During this thesis the analysis of the systematic effects was done to identify potential problems with the current experiment. Numerical simulations were performed to include all effects arising from the large number of states in the system. They can be broadly grouped in two classes: shifts that arise from the way the experiment is performed and second shifts that are gravity based. They are fundamentally present in the way the neutrons perceive gravity. For example an experimental shift is a phase offset between section II and IV. A gravity based shift is induced by the fact that the experiment is located on the surface of a rotating ball.

4.1 Experimental systematic shifts of the transition frequency

In the rotating-wave/secular approximation the shape of the Ramsey transition curve is symmetric with respect to the resonance frequency. There are a number of effects that can shift the resonance frequency, some are easy to calculate, others need extensive numerical treatment. Here I will discuss experimental effects that are caused by the design of the qBOUNCE experiment. They can be controlled in some way, at least in principle, by changing parameters of the experiment.

4.1.1 Phase offset $\Delta\phi$

As follows from equation 2.31 a phase shift $\Delta\phi$ between the two oscillating sections results in a direct shift of the transition frequency. Close to an ideal $\pi/2$ flip this can be simplified and it follows from 2.36 that the shifted point ν_1 of lowest transition probability is given by

$$
\begin{aligned}
P(|p\rangle \to |p\rangle) &= \frac{1}{2}\left(1 - \cos\left(\frac{\pi(\nu - \nu_0)}{w_\nu} + \Delta\phi\right)\right) \\
&= \frac{1}{2}\left(1 - \cos\left(\frac{\pi}{w_\nu}\left(\nu - \left(\nu_0 - \frac{w_\nu}{\pi}\Delta\phi\right)\right)\right)\right) \\
&= \frac{1}{2}\left(1 - \cos\left(\frac{\pi}{w_\nu}(\nu - \nu_1)\right)\right),
\end{aligned}
\tag{4.1}
$$

$$
\nu_1 = \nu_0 - \delta\nu = \nu_0 - \frac{w_\nu}{\pi}\Delta\phi = \nu_0 - \frac{w_\nu}{180}\Delta\phi_{[deg]},
\tag{4.2}
$$

where $\delta\nu$ is the shift induced by the phase offset which is linear in $\Delta\phi$ and $\Delta\phi_{[deg]}$ is the phase shift in degrees. To minimize this effect the relative phase of the oscillating mirrors is calibrated and monitored with an external interferometer described in 3.3.9. The width $w_\nu \approx 8\,\mathrm{Hz}$ so this direct shift of the transition frequency is given by

$$
\delta\nu \approx \frac{8}{180}\Delta\phi_{[deg]} \approx 4.44 \cdot 10^{-2}\Delta\phi_{[deg]}.
\tag{4.3}
$$

This shift of the frequency is independent of ν_0, so a constant offset of the phase can be excluded by comparing the transition frequencies of different transitions. If they are shifted by the same amount, this is evidence for a constant offset of the applied phase.

The measurement of the phase offset is one of the most crucial points for the ability of the Ramsey method to perform well and to give absolute frequency measurements. If this phase drifts over time or is not well determined, the measurements are not trivial to interpret, if not impossible. For an uniformly distributed $\Delta\phi$ one measures the mean of the Ramsey curve as was discussed in section 2.5. If the phase is an arbitrary function with frequency any curve inside the envelope can be obtained in the frequency sweep. For the phase stability in the actual experiment a stability of $\approx \pm 0.94°$ was observed. This leads to a shift in frequency of $\delta\nu \approx 4.26 \times 10^{-2}\,\text{Hz}$. This value varies from point to point. Some frequency points were much less stable, which is a limiting factor when addressing a certain frequency range. The transition $|1\rangle \to |5\rangle$ was close to a mechanical resonance of the system and the phase was very unstable and destructive amplification of the mirror oscillation occurred.

4.1.2 Bloch Siegert shift

In the derivation of the formula for the transmission curve with Ramseys method one major simplification was made. The excitation of the states $f(t) = a\sin\left(a\omega t + \phi\right)$ was simplified to $f(t) \approx \frac{a}{2}e^{\pm(\omega t + \phi)}$. This leads to a shift in the calculated transition frequency. For NMR Ramsey this is known as the Bloch-Siegert shift. For electromagnetic excitations this "shift" can be eliminated by rotating the magnetic field. In GRS this is not possible since the mirror surface necessarily follows a real sine curve. Starting from equation (2.22) and introducing new variables $C_p(t) = e^{i\frac{\delta}{2}t}C'_p(t)$, $C_q(t) = e^{-i\frac{\delta}{2}t}C'_q(t)$ gives

$$\begin{pmatrix} \dot{C}'_p(t) \\ \dot{C}'_q(t) \end{pmatrix} = \left(\begin{pmatrix} i\frac{\delta}{2} & V_{pq}e^{-i\phi} \\ -V_{pq}e^{i\phi} & -i\frac{\delta}{2} \end{pmatrix} + \begin{pmatrix} 0 & V_{pq}e^{i\phi}e^{2i\omega t} \\ -V_{pq}e^{-i\phi}e^{-2i\omega t} & 0 \end{pmatrix} \right) \begin{pmatrix} C'_p(t) \\ C'_q(t) \end{pmatrix} , \qquad (4.4)$$

Ignoring the time dependent matrix on the right leads to the rotating-wave/secular approximation used before in the derivation of the Ramsey curve. The second part oscillates with 2ω. This additional term leads to a modification of the transition probabilities derived from the idealised case. The detailed derivation of this was done by Bloch and Siegert [46] for the case of a Rabi transition.

In the case of Ramseys method of separated oscillating fields, the shift is modified and can be found in [25, 26]. Shirley gives a transcendental function for determining the detuning δ as

$$\frac{\tan(\frac{\delta}{2}T)}{T} \left(1 + \frac{\tan\left(\frac{a\omega V_{pq}}{2}\tau\right)}{\frac{a\omega V_{pq}}{2}T} \right) = -\frac{\delta}{a\omega V_{pq}T} \tan\left(\frac{a\omega V_{pq}}{2}\tau\right) + \frac{a\omega V_{pq}}{4\omega_{qp}T} \tan\left(\frac{a\omega V_{pq}}{2}\tau\right) \qquad (4.5)$$

In the reference, the formula is simplified for the conditions given in many beam type Ramsey experiments, which can then be solved analytically. For qBOUNCE this is not at all the case, and the transition frequency has to be found by numerical solution of (4.5). The resulting shift can be seen in fig. 4.1 for different velocities and transitions.

This illustrates two different effects: The shift gets smaller for a higher transition frequency i.e. higher Δn in the transition $|n\rangle \to |n + \Delta n\rangle$, because the secular approximation gets better with higher frequency and second it decreases with increasing neutron velocity, which can be viewed as increasing with increasing interaction time.

To verify the numerical calculations in the next chapter a two state system with a cosine excitation was simulated using the n-state algorithm. In general this system can be integrated numerically which shows that the shift of the numerical calculation does not agree with the given formula. Changing the neutron velocity in the numerical simulation produces a fast oscillating shift of the transition frequency obtained from an experiment. This has been noted previously in [47]. In a complete analysis an average over a multitude of velocities is performed, reducing the overall effect of this. In [47] there is another subtle effect concerning the initial phase of the two oscillating sections is outlined. In the qBOUNCE experiment, the oscillation of section II is given by $a\sin\left(\omega t + \phi_{II}\right)$ and for section IV by $a\sin\left(\omega t + \phi_{II} + \Delta\phi\right)$. In the case of the rotating wave approximation in eq. 2.30 the only relevant parameter is $\Delta\phi = \phi_{II} + \Delta\phi - \phi_{II}$ and the initial phase ϕ_{II} drops out. In effect the initial phase in the rotating secular approximation
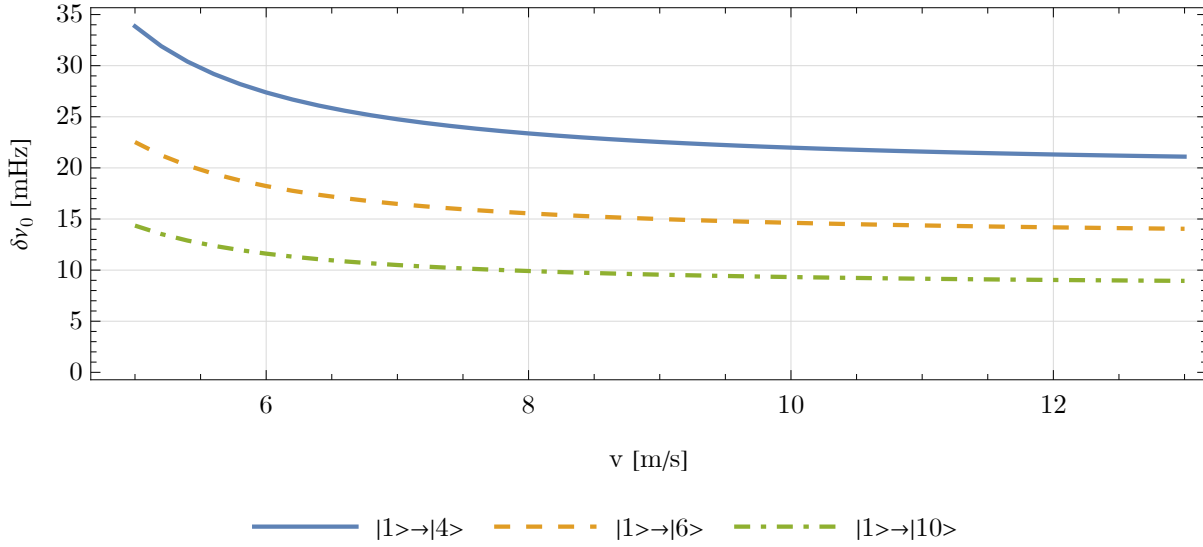
Figure 4.1: Shift of the transition frequency due to the Bloch Siegert Shift from [25] For different velocities and different transitions for constant oscillation strength.

is a global phase that can be disregarded. This is not the case any more for the sine excitation. In fig. 4.1.5 the transmission probability for different velocities with different initial phases can be seen. This behaviour is highly complicated and depends also on the number of states used in the calculation. The initial phase of the neutron mirror can not be controlled, so the initial phase is random. Since the neutron rate is $\sim 3 \times 10^{-2}$ cps in a constant beam, whereas the oscillation frequency is $\sim 1\,\mathrm{kHz}$ the phase of the mirrors when a neutron arrives can be treated as uniformly distributed. Numerical results for a qBOUNCE like system are performed in 4.1.5, where the effect of an averaging over the phase and the velocity can be seen in fig. 4.12. An extended discussion for the more general case including state selection and background vibrations can be found in ch. 4.1.6. The order of magnitude obtained from (4.5) is correct, but the direction is dependent on other effects. Therefore the formula can be used as a rough estimation tool but not for precise predictions.

4.1.3 Magnetic fields

The qBOUNCE experiment is inside a μ-metal shielded vacuum chamber, therefore the background magnetic field is suppressed, see ch. 3.3.3. In general the Hamiltonian of the system gains an additional magnetic interaction term

$$\hat{V}_B = \hat{\mu} \cdot \mathbf{B} \approx \hat{\mu} \cdot \mathbf{B}\,(0) + (\hat{\mu} \cdot \nabla \mathbf{B}\,(0)) \cdot \mathbf{r} \,, \tag{4.6}$$

where $\hat{\mu}$ is the magnetic moment of the neutron and the last equality is the linearisation at the origin. The first part is a constant shift that does not influence the space part of the wave function. In general the x and y components of the magnetic field gradient lead to an acceleration of the neutron tangential to the mirror. This shifts the velocity spectrum slightly. Since the oscillation parameters are tuned for an optimal excitation this would only be observable when comparing to the zero field case. The z component $(\hat{\mu} \cdot \partial_z \mathbf{B}\,(0))\,z$ contributes to the wave function in z direction and modifies the gravity potential $m_g g z$ to

$$\hat{V}_{g+B} = m_g g z + (\hat{\mu} \cdot \partial_z \mathbf{B}\,(0))\,z = m_g \left(g + \left(\frac{\hat{\mu} \cdot \partial_z \mathbf{B}}{m_g}\,(0) \right) \right) z \tag{4.7}$$

which is an effective shift of g. For a magnetic field in z this gives a modification of g

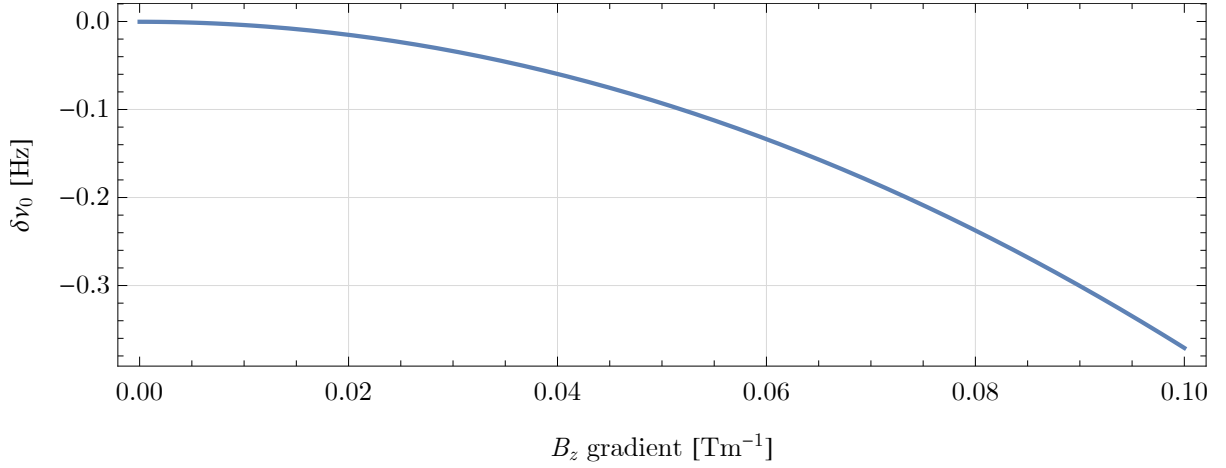$$g' = g \pm 5.74\,\partial_z \mathbf{B}_z \,, \tag{4.8}$$

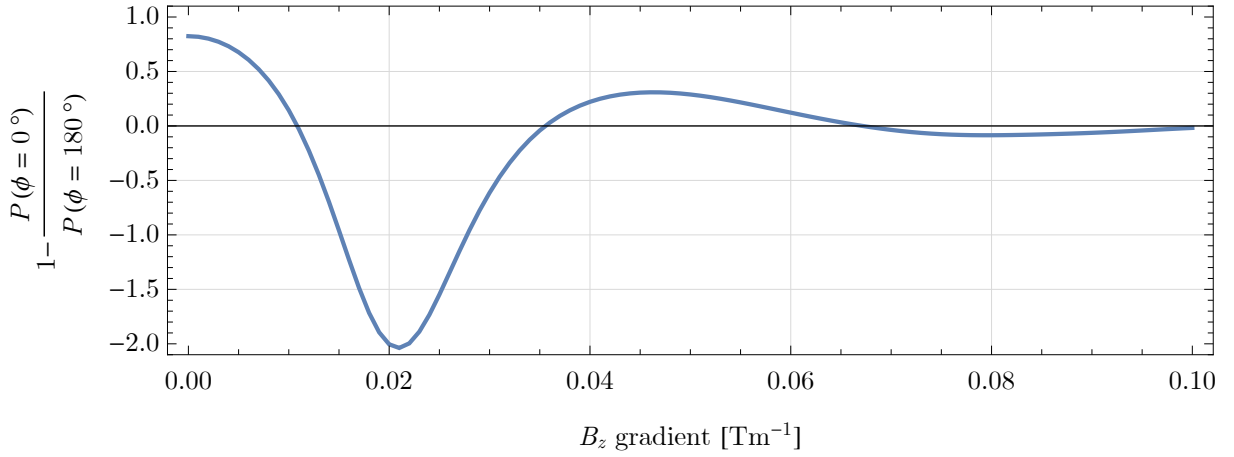Figure 4.2: Calculated shift in the transition frequency for an unpolarised neutron beam.

Figure 4.3: Calculated contrast $1 - \frac{P(\phi=0)}{P(\phi=\pi)}$ for an unpolarised neutron beam. For specific values of $\partial_z B_z$ the Ramsey curves for $\phi = 0$ and $\phi = \pi$ flip as seen in 4.5.

a very large effect. qBOUNCE uses unpolarised neutrons, so in general the transmission curve measured is an incoherent sum of the two spin directions. This leads to an effective shift of the transition frequency shown in fig. 4.2. This effective shift is in the negative direction for any magnetic field configuration. Furthermore in fig. 4.3 the contrast $1 - \frac{P(\phi=0)}{P(\phi=\pi)}$ is shown. For certain values of the B field, the measured point for 0 phase is above the 180° point. An example of this can be seen in fig. 4.5. Additionally a decrease in the measured contrast is present that suppresses the measurement contrast. This is obvious in fig. 4.6, the two spin components move far apart such that the transitions only overlap slightly in the middle. As the observed transition is such that the 0 phase measurement is below the π measurement and there are no two separated transitions observed, high magnetic field gradients can be excluded. Additionally when measuring the magnetic field in the chamber the highest value was about $3\,\mu\text{T}$ with all other values smaller than that. This measurement was taken next to the motor of the linear stage for the capacitive sensors $\approx 30\,\text{cm}$ away from the neutron path. The B-field sensor averages over a length of about $3\,\text{cm}$ leading to about $\partial_z B_z = 2 \times 10^{-4}\,\text{T}\,\text{m}^{-1}$. This corresponds to $\delta\nu_0 \approx -3.44 \times 10^{-4}\,\text{Hz}$ for the central frequency of unpolarised neutrons or $\delta g \approx -1.148 \times 10^{-3}\,\text{m/s}^2$ for an unpolarised neutron beam.

However there are caveats in this discussion. If the neutron beam is 100% polarised, this discussion is invalid and very large shifts can be produced easily, in any direction. Furthermore the precise μm resolution measurement of the magnetic field gradient at the location of the neutron flight path is not
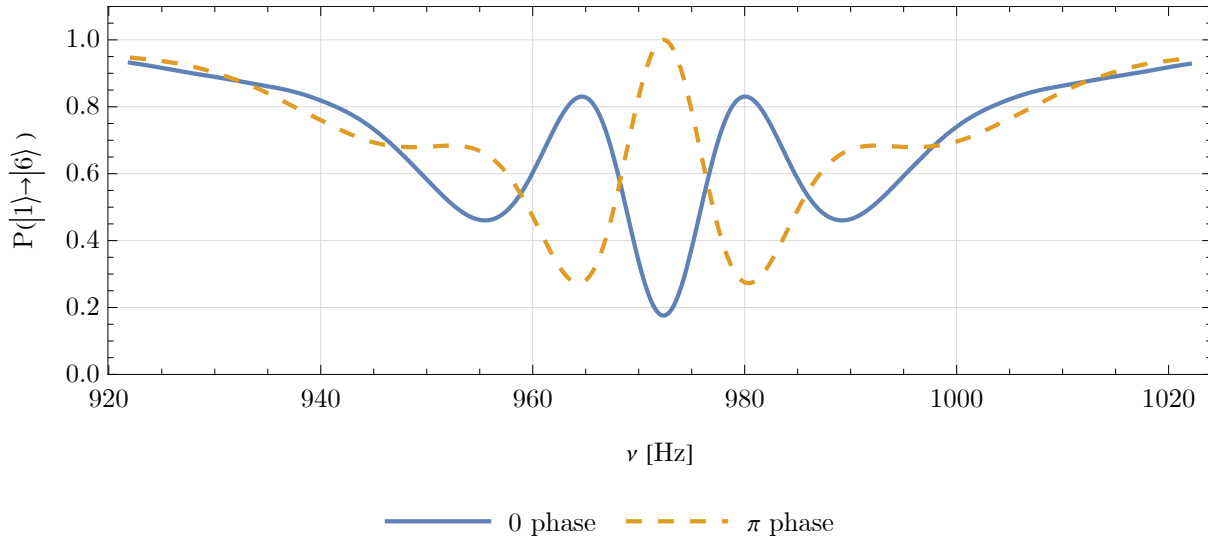
Figure 4.4: $\phi = 0$ and $\phi = \pi$ pattern for $\partial_z B_z = 0.0\,\mathrm{T\,m^{-1}}$
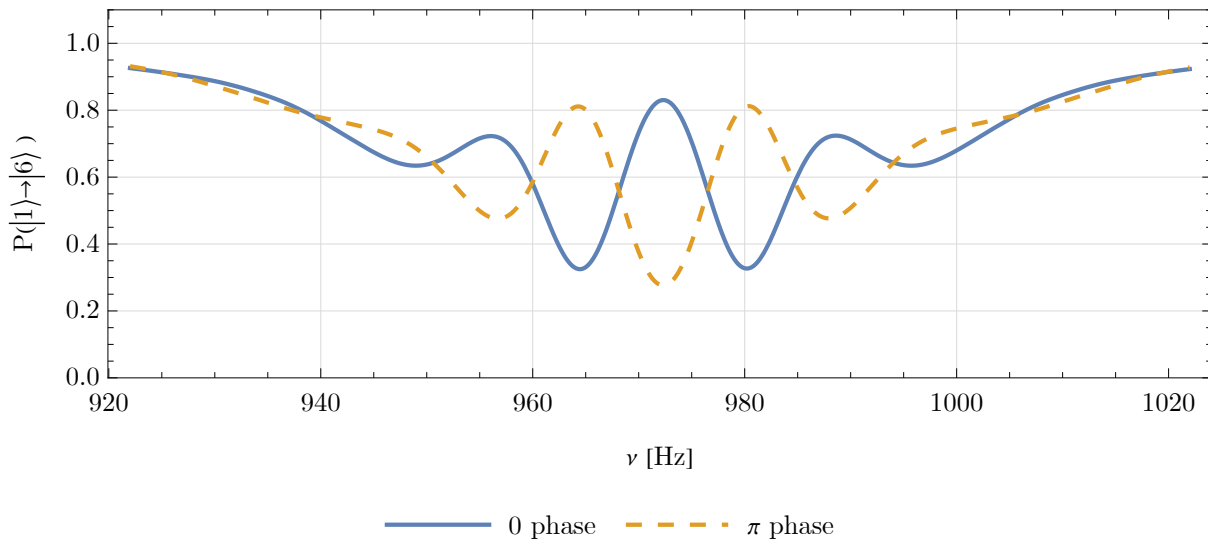
Figure 4.5: Flipped $\phi = 0$ and $\phi = \pi$ pattern for $\partial_z B_z = 0.02\,\mathrm{T\,m^{-1}}$.
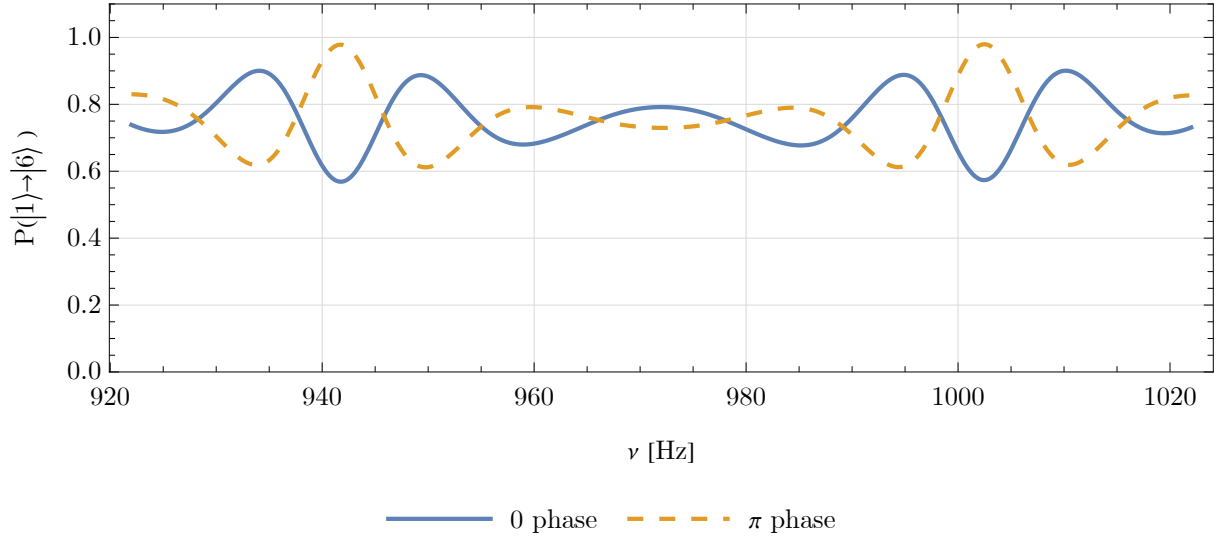
Figure 4.6: Flipped $\phi = 0$ and $\phi = \pi$ pattern for $\partial_z B_z = 0.08\,\mathrm{T\,m^{-1}}$, where the measured contrast is also decreased significantly. The two resonance curves for the different spin components are clearly visible as two independent transitions far from the original location at $\nu \approx 972.345\,\mathrm{Hz}$.

possible with the currently available equipment (at least to qBOUNCE).

4.1.4 Steps

There are two reasons why steps between mirrors cause shifts in the transition frequency. The first is that steps introduce transitions between states which causes a shift in the state distribution. Due to higher order multi-state effects this causes a frequency shift of a given transition. This is discussed in chapter 4.1.5. Another cause is due to the way the measurements are taken. From equation (2.31) and (2.34) the transition probability is symmetric when taking $a\omega$ constant. a is the displacement of the oscillating mirrors and $a \sim \omega^{-1}$ for $a\omega$ constant. This means that for lower frequencies the maximum displacement is larger and for higher frequencies is lower. This causes a geometrical reduction of the transmission. A rough sketch is shown in fig. 4.7. The neutron arrives from the left, encounters a step and is partially reflected. This causes an additional loss of transmission. Since the displacement is $\sim \nu^{-1}$ this is an additional frequency dependent loss that can shift the theoretical transmission curve. As a first estimate the worst case of a displacement by $2a$ above the stationary mirror is assumed. The transmission $\mathcal{T}$ through the step is then given by

$$\mathcal{T}(a) = 1 - \int_0^{2a} |\psi|^2 \mathrm{d}z \,\hat{=}\, 1 - \int_0^{\frac{2a\omega}{2\pi\nu}} |\psi|^2 \mathrm{d}z = \mathcal{T}(\nu) \,, \tag{4.9}$$

where the $\hat{=}$ corresponds to the case where $a\omega$ is fixed and therefore a and $\mathcal{T}$ are functions of the frequency ν. For an eigenstate ψ_n this integral can be evaluated to

$$\begin{aligned}
\mathcal{T}_n(\nu) &= z_0^3 \psi_n'^2 \left(\frac{2a\omega}{2\pi\nu} \right) - \left(\frac{2a\omega}{2\pi\nu} - \frac{E_n}{m_n g} \right) \psi_n \left(\frac{2a\omega}{2\pi\nu} \right)^2 \\
&= \frac{\mathrm{Ai}' \left(\frac{2a\omega}{2\pi\nu z_0} + \mathrm{AiZ}\,(n) \right)^2}{\mathrm{Ai}' \left(\mathrm{AiZ}\,(n) \right)^2} - \left(\frac{2a\omega}{2\pi\nu z_0} + \mathrm{AiZ}\,(n) \right) \frac{\mathrm{Ai}' \left(\frac{2a\omega}{2\pi\nu z_0} + \mathrm{AiZ}\,(n) \right)^2}{\mathrm{Ai}' \left(\mathrm{AiZ}\,(n) \right)^2}
\end{aligned} \tag{4.10}$$

from (A.7), where in the second line the normalised eigenstate from (2.13) was inserted. In fig. 4.8 $\mathcal{T}_n(\nu)$ can be seen for $a\omega = 3.6\,\mathrm{mm\,s^{-1}}$ and $n = 1, 6$. This corresponds to typical values in the experiment. Taking an idealised transition probability with
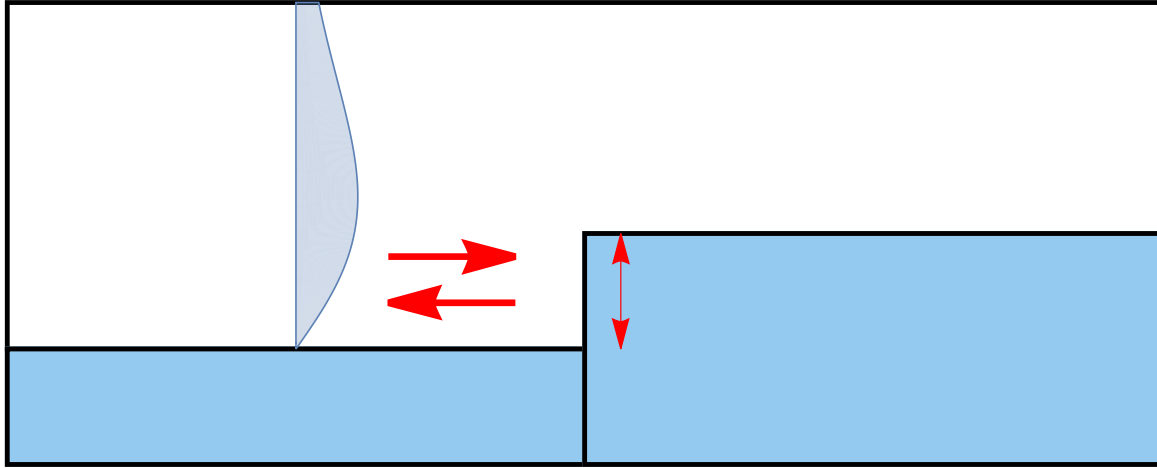
Figure 4.7: An incoming neutron from the left in a specific state (here the first) encounters a step and is partially reflected. This leads to a reduction in transmission that is dependent on the displacement of the higher mirror.
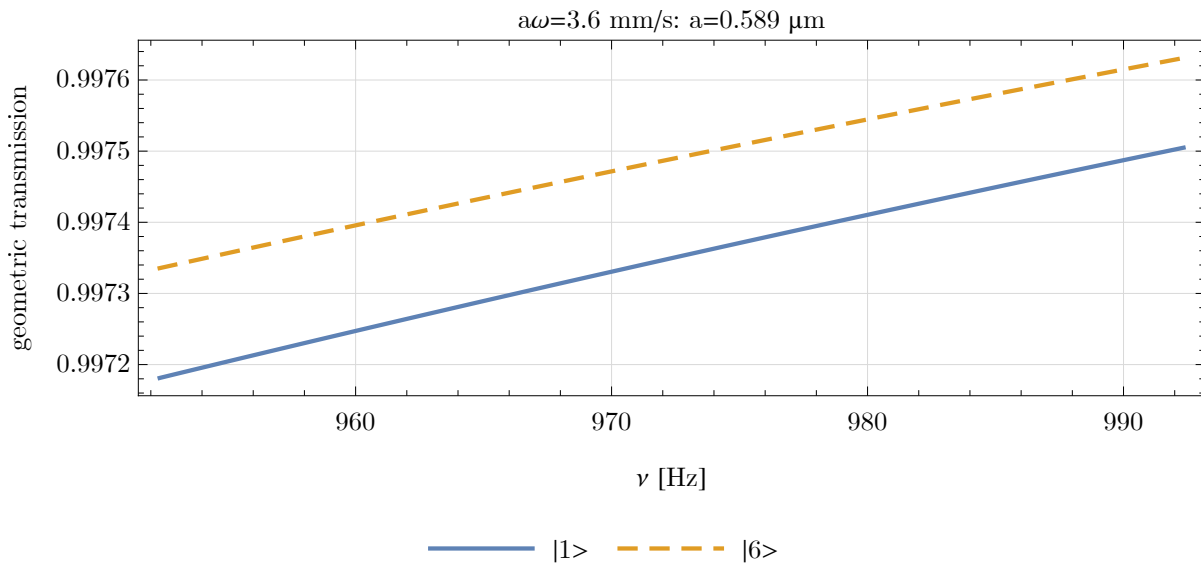

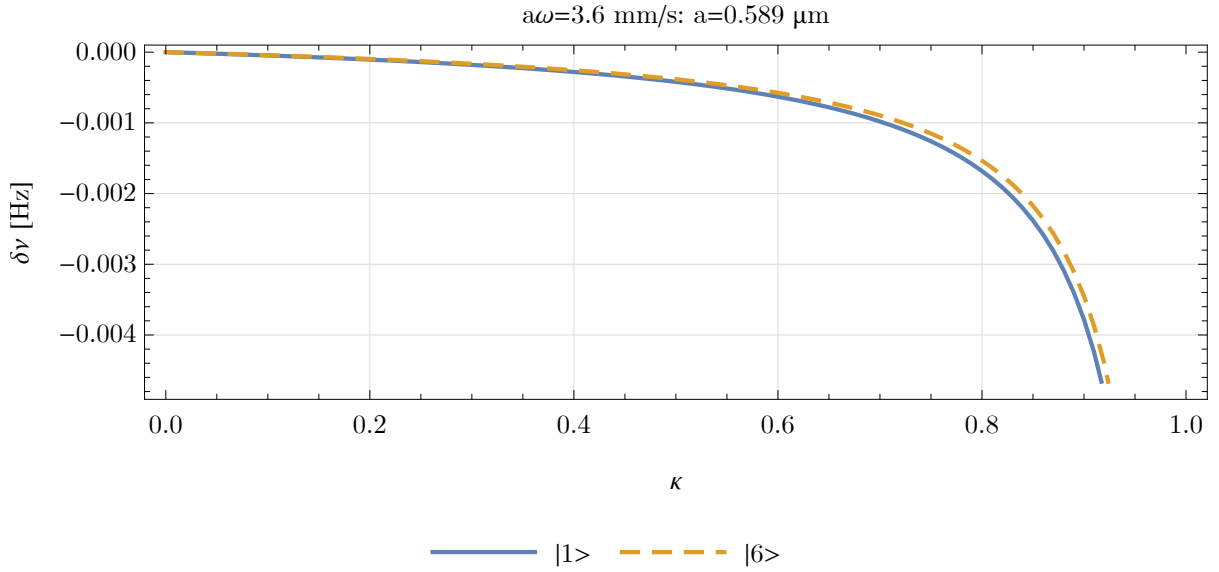Figure 4.8: Geometric transmission for parameters typically used in qBOUNCE for states $|1\rangle$ and $|6\rangle$.

Figure 4.9: Shift in the transition frequency of the transition $|1\rangle \to |6\rangle$ for typical excitation values. Typically in qBOUNCE $\kappa \in [0.4; 0.6]$.

$$P\left(\nu|\kappa\right) = \frac{\kappa+1}{2} + \frac{\kappa-1}{2}\cos\left(\frac{\pi}{8}\left(\nu - 972.345\right)\right) \tag{4.11}$$

where the transition frequency is $\nu_{61} \approx 972.345\,\mathrm{Hz}$ the width is $w_\nu = 8\,\mathrm{Hz}$ and the transition probability at the resonance frequency is given by κ. This corresponds to the measured value of $g \approx 9.805\,\mathrm{m/s^2}$. Now the total transmission probability through the experiment P' including the effect of the geometric losses can be calculated via

$$P'\left(\nu|n,\kappa\right) = \mathcal{T}_n(\nu)^4 P\left(\nu|\kappa\right) \ , \tag{4.12}$$

which depends on the parameter κ and contributing states. The power of four comes from steps between sections I&II, II&III, III&IV and finally IV&V. If all of these act on the ground state $|1\rangle$ the effect is the largest. Using this equation the shift of the resonance frequency can be numerically calculated and is shown in fig. 4.9. Typically $\kappa \in [0.4; 0.6]$, where the shift $|\delta\nu| < 5\,\mathrm{mHz}$. As a worst case $\Delta\nu = -5\,\mathrm{mHz}$ which gives a relative energy shift of $\delta E/E = -5 \times 10^{-6}$ or a relative shift of the acceleration g $\delta g/g = 3/2\delta E/E = -7.5 \times 10^{-6}$.

4.1.5 Multi state effects (and generalised Bloch-Siegert shift)

Another important effect for qBOUNCE is the fact, that there are infinitely many states present in the system. This becomes more important when the state preparation and selection at the end is not able to perfectly select the ground state of the system. As described in chapter 2.2 this is not possible, since there always is an overlap between the neutron wave function and the scattering slit for more than one state. Because of this there is always an additional contribution from additional states and transitions in the system. This effect is called spectator shift. In light of ch. 4.1.2 the Bloch Siegert shift is also included here by using the sin excitation. These two effects can neither be separated logically nor experimentally. In addition a background oscillation or magnetic field would also have to be considered here. This was not done because these effects are small compared to the multi state effects considered here. Here a numerical analysis is given, an analytical treatment can be found in [48] which gives a slowly converging series for the frequency shifts. in general this analysis is numerically expensive in any case. An in depth analysis of the series representation of the spectator shift was done by [49]. Here I will describe how the numerical integration approach was done. I will now switch notation slightly, the perturbation matrix is now represented by $\hat{V}$ and the state simply by C with all time dependences implicit. The "operator" $\hat{V}$

acts on as many states as one chooses to consider so that (2.20) is given by

$$\dot{C} = \hat{V}C \tag{4.13}$$

introducing the time evolution operator $\hat{U} = \hat{U}(t, t_0)$ such that $C(t) = \hat{U}(t, t_0)C_0$ where C_0 is the occupation number vector at time t_0 this equation can be written as

$$\left(\dot{U} - \hat{V}\hat{U}\right) C_0 = 0 \, , \tag{4.14}$$

which has to be valid for all initial state configurations C_0. The time evolution "operator" $\hat{U}$ has to satisfy

$$\left(\dot{U} - \hat{V}\hat{U}\right) = 0, \ \hat{U}(t_0, t_0) = 1 \, . \tag{4.15}$$

Here 1 is the unit matrix with appropriate dimension. This equation can be solved formally by a time ordered matrix exponential. For the case with infinitely many states this is the time ordered matrix exponential of an "infinite dimensional" matrix. In any case we hope to be only interested in the case where an approximation with finitely many states is sufficient (barring any emergent as of yet unknown phenomena). This equation is used, because all quantities in this equation can be solved numerically beforehand for all times of interest to the necessary precision. If the numerical integration converges for all times of interest, one can use any initial condition to calculate the occupation number at a later time.

There are two main effects that are physically relevant in the system: firstly the imperfect state preparation and secondly steps between mirrors. The imperfect state preparation can be dealt with as an initial condition, and the imperfect selection at the end is just the final state we choose to select. In this context it should be mentioned, that we believe the UCNs to be in a mixed ensemble before the state preparation, and also that the state selector is a non coherent state selection. In [19] experiments were performed that confirm this, the analysis results in the incoherent sum. This is implemented by "integrating" over all relative phases of the occupation number in the initial and final states. For this purpose I introduce the density matrix formalism where $\hat{\rho}_0 = C_0 C_0^\dagger$ and $\hat{\rho}_f = C_f C_f^\dagger$ are the density matrix of the initial and final state respectively. The time evolution can be inferred from $C(t) = \hat{U}C_0$, and the probability to be in the state ρ_f is given by

$$P(\rho_f) = \text{Tr}\left(\hat{\rho}_f \hat{\rho}(t)\right) = \text{Tr}\left(\hat{\rho}_f \hat{U} \hat{\rho}_0 \hat{U}^\dagger\right) \, . \tag{4.16}$$

Integrating over relative phases means that all terms in $\hat{\rho}_0$ and $\hat{\rho}_f$ with a relative phase drop out, thus leaving two diagonal matrices for $\hat{\rho}_0$ and $\hat{\rho}_f$, where the diagonal entries are given by the probability to be in the corresponding state. As a simple example consider the state $\mathbf{C} = (C_0, C_1)^T = (|C_0|e^{i\varphi}, |C_1|e^{i\chi})^T$, the density Matrix is given by

$$\hat{\rho} = \mathbf{C}\mathbf{C}^\dagger = \begin{pmatrix} |C_0|^2 & |C_0||C_1|e^{i(\varphi-\chi)} \\ |C_0||C_1|e^{-i(\varphi-\chi)} & |C_1|^2 \end{pmatrix} \tag{4.17}$$

where φ and χ are the phases of the first and the second state respectively. Non coherence means that there is no fixed relation between φ and χ and is averaged over in the density matrix. Since $\int_0^{2\pi} e^{i\phi}\mathrm{d}\phi = 0$

$$\langle\hat{\rho}\rangle_\phi = \frac{1}{2\pi}\int_0^{2\pi} \hat{\rho} \, \mathrm{d}\phi = \begin{pmatrix} |C_0|^2 & 0 \\ 0 & |C_1|^2 \end{pmatrix} \tag{4.18}$$

This can be extended to any number of states by averaging over all relative phases between the states. Thus writing out indices, this means $(\hat{\rho}_f)_{ij} = \sum_n P_f^n \delta_{ni}\delta_{nj}$ and similarly $(\hat{\rho}_0)_{ij} = \sum_n P_0^n \delta_{ni}\delta_{nj}$, where P_f^n, P_0^n are the probabilities for a state n in the final and initial state respectively. Now writing out the probability with the trace using indices leads to

$$P(\rho_f) = \text{Tr}\left(\hat{\rho}_f U \hat{\rho}_0 U^\dagger\right) = \sum_{i,j,k,l} (\hat{\rho}_f)_{ij} \left(\hat{U}\right)_{jk} (\hat{\rho}_0)_{kl} \left(\hat{U}^\dagger\right)_{li} =$$

$$\sum_{i,j,k,l} \sum_n P_f^n \delta_{ni}\delta_{nj} \left(\hat{U}\right)_{jk} \sum_m P_0^m \delta_{mk}\delta_{ml} \left(\hat{U}^\dagger\right)_{li} = \tag{4.19}$$

$$\sum_{n,m} P_f^n P_0^m \left(\hat{U}\right)_{nm} \left(\hat{U}\right)_{nm}^*$$

This equation is the basis for all numerical analysis. In case of steps between mirrors U has to modified. Steps could be included by specifying the function f in (2.20) used for the mirror surface with Heaviside Θ distributions, which would lead to δ contributions in equation (4.15). However this is numerically highly unethical, therefore a different approach is taken. Specifying the velocity $\dot{f}$ of the mirror directly and turning this perturbation "on" and "off" ignores any transitions between two mirrors at different heights. Suppose the effect of a step at time t_1 is encoded by the matrix $\hat{S}$. Thus the time evolution U' with step can be split up via

$$C(t) = \hat{U}'(t, t_0)C(t_0) = \hat{U}'(t, t_1)\hat{S}\hat{U}'(t_1, t_0)C(t_0) = \hat{U}(t, t_1)\hat{S}\hat{U}(t_1, t_0)C_0$$
$$\Rightarrow \hat{U}'(t, t_0) = \hat{U}(t, t_1)\hat{S}\hat{U}(t_1, t_0) \tag{4.20}$$

where the $\hat{U}'$ can be replaced by $\hat{U}$ since there are no steps in $t \in [t_0, t_1)$ and $t \in (t_1, t]$. In order to calculate $\hat{U}(t, t_1)$

$$C(t) = \hat{U}(t, t_0)C_0 = \hat{U}(t, t_1)C(t_1) = \hat{U}(t, t_1)\hat{U}(t_1, t_0)C_0$$
$$\Rightarrow \hat{U}(t, t_1) = \hat{U}(t, t_0)\hat{U}^{-1}(t_1, t_0) = \hat{U}(t, t_0)\hat{U}^\dagger(t_1, t_0) \tag{4.21}$$

can be used. This is the group structure of the time evolution operator. This gives

$$\hat{U}'(t, t_0) = \hat{U}(t, t_0)\hat{U}^\dagger(t_1, t_0)\hat{S}\hat{U}(t_1, t_0) \tag{4.22}$$

This derivation can be extended in the same way to an arbitrary number of steps. The transition matrix $\hat{S}$ can be determined analytically in terms of Airy functions for any step (in the case of non penetrating wave functions) as is shown in appendix A . Constructing the complete time evolution $\hat{U}'$ from $\hat{U}$ one can use eq. 4.19 to also include steps, without repeating the numerical integration. The advantage of this approach is clear when it is necessary to vary the occupation number and step heights in a fit, since only the matrices $\hat{S}$ for the steps and the P_f^n and P_0^n have to be recalculated, but the numerical integration and inversion for the insertion of the steps has to be done only once.

Using this approach the transition frequencies can be determined by numerical calculation. This is done for 30 states which shows the features present when doing this. In fig. 4.10 probability curves $P(|1\rangle \to |1\rangle)$ are shown for different neutron velocities. As discussed before the initial phase ϕ_{II} has an unpredictable nature to it and varies also significantly for different velocities. This makes it necessary to average over the initial phase as well as the velocity for an evaluation of frequency shifts. Performing the velocity integration with the measured velocity spectrum results in 4.11 where the velocity average over $v \in [4; 14]$ has been performed. This shows a residual probability variation at the percent level.

Performing the same for all six points at the positions described in 2.6 is shown in fig. 4.12. The solid lines are a fits using a cosine and the 2-state theory function giving an estimate of the observable frequency shift. The transition frequencies are given by $\nu_{cos} = 972.23(5)\,\mathrm{Hz}$ and $\nu_{2-state} = 972.20(5)\,\mathrm{Hz}$ for the two different models. The errors assume a 1% error for these measurement and shows that the two frequency results are compatible.

From this it follows that the combined Bloch-Siegert and spectator state shift for real experimental parameters gives $\approx -0.1\,\mathrm{Hz}$ when compared to the frequency expected from the energy differences. Using a simple cosine fit without any prior knowledge of the detailed theory to this transition leads to a frequency lower than the true value. This effect is highly transition dependent, here it was shown for $|1\rangle \to |6\rangle$ at $\nu \approx 972.345\,\mathrm{Hz}$ for a ground state selection, but the shift changes for different transition due to different contributions from neighbouring transitions and also due to a different contribution of the Bloch-Siegert shift. In fig 4.13 the transition probability for the state $|(0.6, 0.3, 0.1)\rangle \to |(0.6, 0.3, 0.1)\rangle$ is shown. An increase in the transition frequency can not be explained by an artefact of the fitting method when evaluating a multi state system.

4.1.6 Background vibrations

The qBOUNCE experiment is located in a noisy environment: the reactor itself uses pumps and industrial equipment generating noise. Furthermore a lot of vacuum pumps are present, within qBOUNCE , at PF2, at other experiments, and so on. This leads to a lot of background vibrations potentially present at the
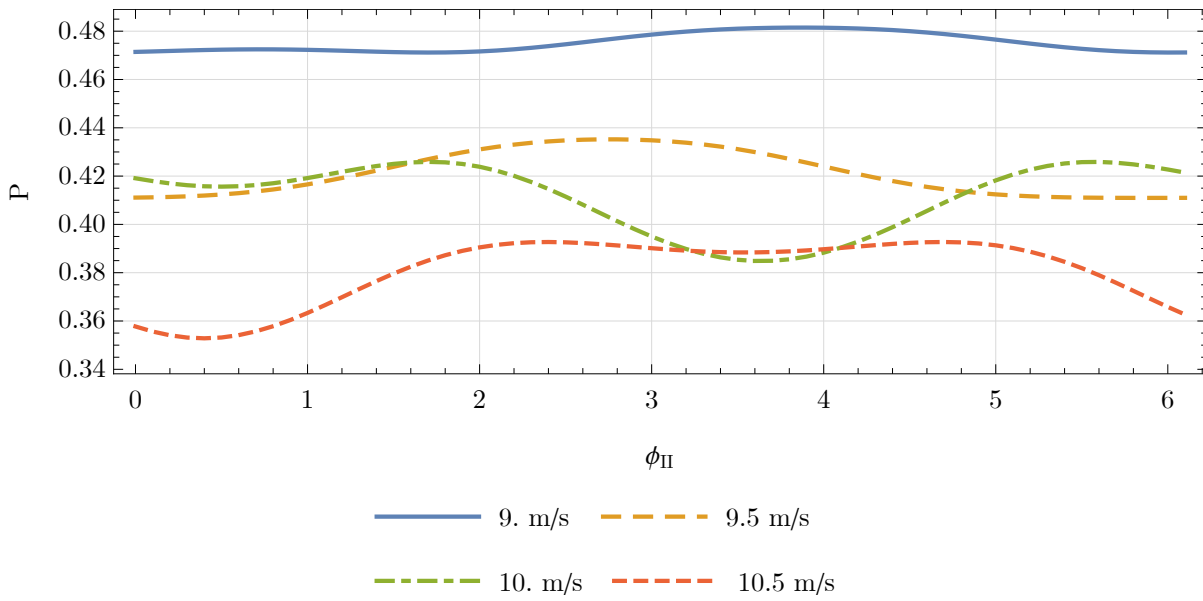
Figure 4.10: Probability $P(|1\rangle \to |1\rangle)$ over the initial phase of section II shown for different neutron velocities. In the small velocity range depicted here there is no obvious pattern visible.
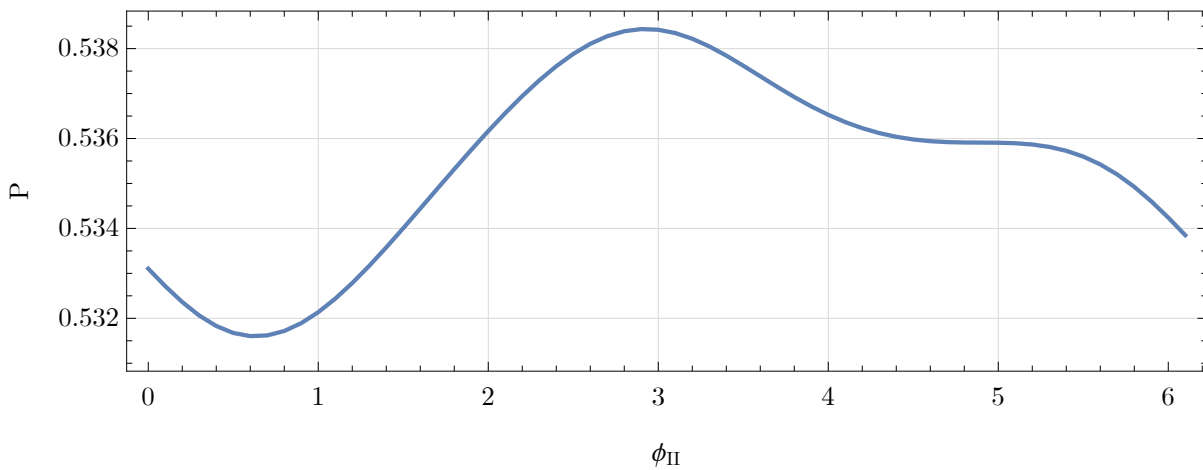

Figure 4.11: Probability $P(|1\rangle \to |1\rangle)$ over the initial phase of section II. Average over all velocities $v \in [4; 14]$m/s taken.
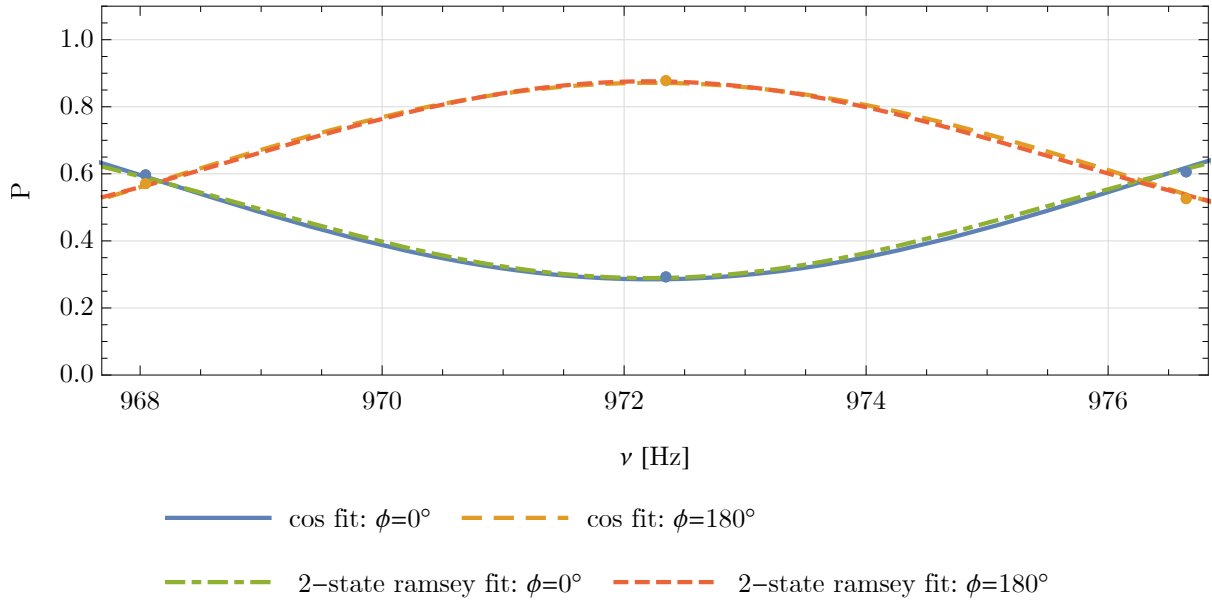
Figure 4.12: Probability $P(|(0.6, 0.3, 0.1)\rangle \rightarrow |1\rangle)$ over frequency. The points are the numerical 30 state resulting from the velocity and phase averaging. The lines are fits using a cosine or the two state Ramsey theory around a central frequency.

neutron mirrors. To limit the influence of these the experiment is located on a granite block to limit high frequency coupling of oscillations. Since the transitions addressed are in the 250 to 1000 Hz range, the whole granite mass acts as a dampener for these audible frequencies. Furthermore an effort was made to limit direct contact of any pumping equipment with the vacuum chamber and experimental platform. Numerical simulations using the measured oscillations from the interferometer were performed for the transition from the state with probabilities $\sim (0.6, 0.3, 0.1)$ to $\sim (0.6, 0.3, 0.1)$, where the final shift in the transition frequency results in $\delta\nu \approx -0.01$ Hz. The precise value depends on the distribution of states in the initial and final states. This can be seen in fig. 4.13 simulated using 30 states and the measured velocity spectrum. Changing the state distributions for the initial and final states leads to shifts between -0.0072 Hz and -0.021 Hz shown in fig. 4.14, where when the second state has a very high contribution the cosine fit does not reproduce the simulated data properly any more. The dashed box indicates the range of occupation probabilities observed in qBOUNCE .

An in depth analysis using an independently determined vibration spectrum, preferably decoupled from the whole experimental platform should be performed. This is at the moment not possible since the only vibration measurements are performed using the interferometers which are themselves mounted on the experimental platform. External vibrations influencing the whole experimental apparatus are not visible to them, whereas the neutrons would be influenced directly. A large unknown excitation at the targeted frequency could induce unknown shifts in the measured signal. Furthermore the precise state distribution can change the shape of the transmission curve and a more in-depth analysis can be performed including more effects that also describe the geometry of the experiment numerically. This is crucial for higher precision experiments.

4.2 Gravity based shifts of the transition frequency

4.2.1 Tilt of the whole experiment

As already described in chapter 3.2.2 an overall tilt of the experiment would lead to the modification of gravity orthogonal to the mirrors. The absolute alignment is accurate to within 10 μrad. The small-scale
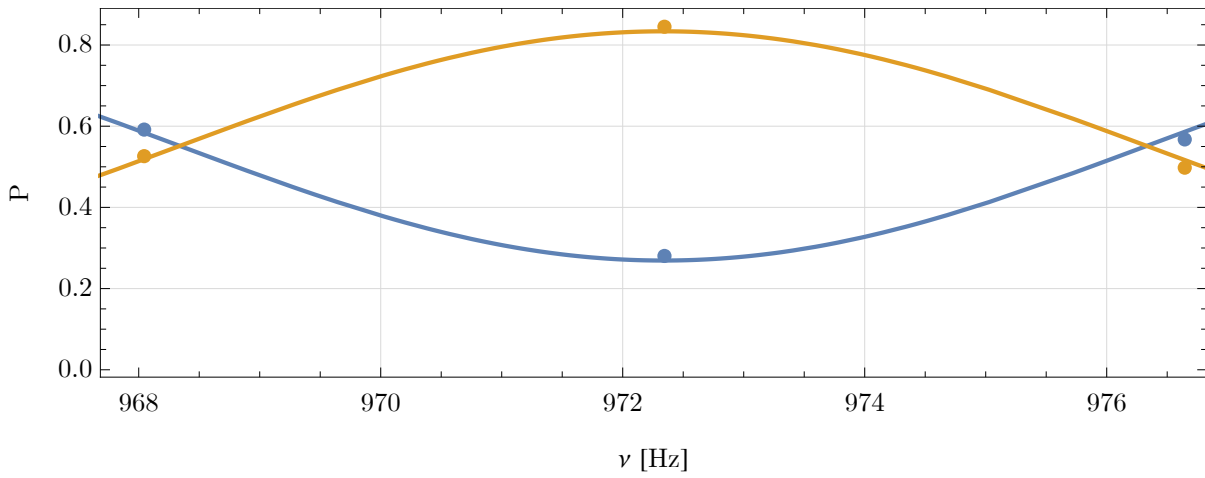
Figure 4.13: Probability $P(|(0.6, 0.3, 0.1)\rangle \to |(0.6, 0.3, 0.1)\rangle)$ over frequency. The line uses a cosine for the fit. This corresponds to realistic values in the actual experiment.
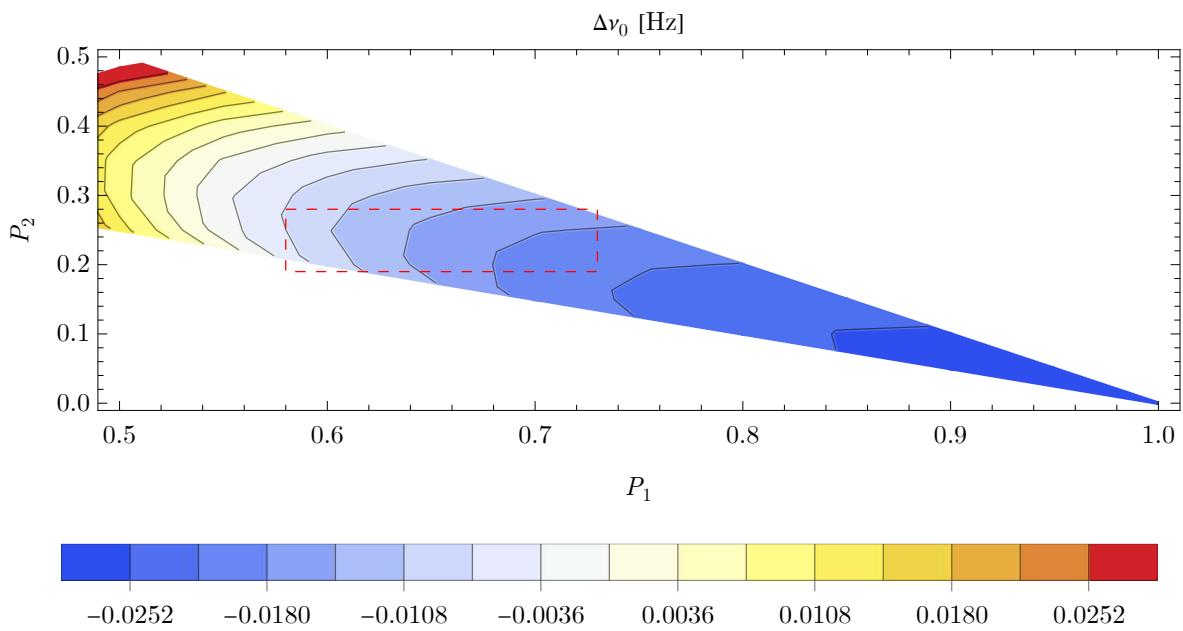
Figure 4.14: Shift of the transition frequency resulting from a cosine fit for varying state probabilities $(P_1, P_2, 1 - P_1 - P_2)$. For extreme values the symmetric cosine does not provide a good fit function any more. The dashed red line indicates the observed occupation probabilities from the final measurements observed within $q\textsc{Bounce}$.

variations are then kept small to within nrad over a whole measurement cycle, which eliminates large variations over a measurement cycle an example was shown above in fig. 3.3. The modification to g following a tilt of angle α can be calculated via

$$g' = g_0 \cos(\alpha) \approx g_0 \left(1 - \frac{\alpha^2}{2}\right), \qquad (4.23)$$

which is always smaller then the unshifted value g_0. Taking $\alpha \approx 1 \cdot 10^{-5}$ results in a worst case shift of $\delta g = -0.5 \cdot 10^{-10} g_0$.

4.2.2 Equivalence of inertial mass m_i and gravitational mass m_g

As noted by [50] in 1965, neutrons might have the same acceleration as free falling matter, but further investigation with more precise measurements is recommended. The value from Dabbs was $g_n = 9.751(29)\,\mathrm{m/s^2}$ for neutrons compared to the local acceleration of $g_{\mathrm{local}} = 9.7974\,\mathrm{m/s^2}$ where no error is given for the local value. Later measurements always perform measurements of the equivalence of the inertial and the gravitational mass of neutrons. This is represented by the ratio $\gamma = m_i/m_g g_0/g_n$ where g_0 is the gravitational acceleration of bulk matter and g_n is the gravitational acceleration of the neutron. In the literature $g_n = g_0$ by assumption. There has been no direct measurement of g confirming the classical potential of gravity for neutron waves. [51, 52]

4.2.3 The rotating Earth

The Earth is rotating with a period of $T \approx 24\,\mathrm{h}$, which introduces apparent forces like the centrifugal force and the Coriolis force. These classical forces also take part in the quantum description of the experiment. Starting with the regular Cartesian coordinate system and introducing the new coordinates r, θ and φ with a function $f(t)$ describing a rotation around the z-axis

$$\begin{pmatrix} x \\ y \\ z \end{pmatrix} = r \begin{pmatrix} \sin(\theta)\cos(f(t)+\varphi) \\ \sin(\theta)\sin(f(t)+\varphi) \\ \cos(\theta) \end{pmatrix} \qquad (4.24)$$

with this the Schrödinger equation

$$i\hbar\partial_t\psi = \left(-\frac{\hbar^2}{2m}\nabla^2 + V(x,y,z)\right)\psi \qquad (4.25)$$

can be transformed to the new coordinate system. The new coordinates are $\tilde{t} = t$, r, θ, φ. Using the standard transformation of differentials leads to the new Schrödinger equation

$$i\hbar\partial_{\tilde{t}}\psi = \left(-\frac{\hbar^2}{2m}\left(\frac{1}{r^2}\partial_r r^2 \partial_r + \frac{1}{r^2\sin\theta}\partial_\theta\sin(\theta)\partial_\theta + \frac{1}{r^2\sin^2(\theta)}\partial_\varphi^2\right) + V(x,y,z) + i\hbar\omega(\tilde{t})\partial_\varphi\right)\psi \quad (4.26)$$

The first part on the right side is the Laplacian in spherical coordinates, which is independent of $f(t)$. Therefore a coordinate system can be introduced, which is a standard Cartesian system rotating with the function $f(t)$.

$$\begin{pmatrix} \tilde{x} \\ \tilde{y} \\ \tilde{z} \end{pmatrix} = r \begin{pmatrix} \sin(\theta)\cos(\varphi) \\ \sin(\theta)\sin(\varphi) \\ \cos(\theta) \end{pmatrix} \qquad (4.27)$$

The term with $\dot{f}(t)$ encodes all contributions of apparent forces arising due to the rotation of the coordinate system. From here on out $f(t) = \omega t$ where $\omega \approx \frac{2\pi}{24\cdot3600}$ for an Earth day of 24 hours. Therefore $\dot{f}(t) = \omega$ for all times. This coordinate system can be seen in 4.15.

In order to simplify analysis this system can be aligned with the orientation of gravity. To do this a rotation seen in fig. 4.16 is applied. Introducing the angle χ around the y axis with the rotated Cartesian coordinate system leads to

$$i\hbar\partial_{\tilde{t}}\psi' = \left(-\frac{\hbar^2}{2m}\nabla^2 + V(z') + i\hbar\omega\left((x'\cos(\chi) + z'\sin\chi)\partial_{y'} - y'(\cos(\chi)\partial_{x'} + \sin(\chi)\partial_{z'})\right)\right)\psi' \quad (4.28)$$
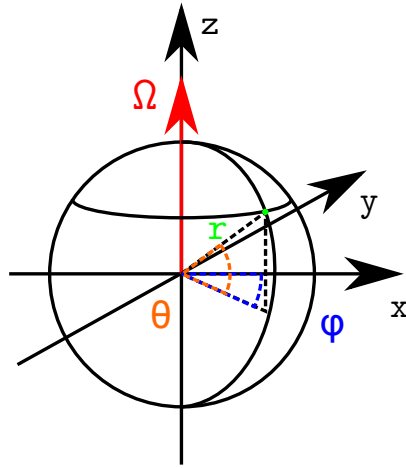
Figure 4.15: Rotating coordinate system seen from an observer at r, θ, φ
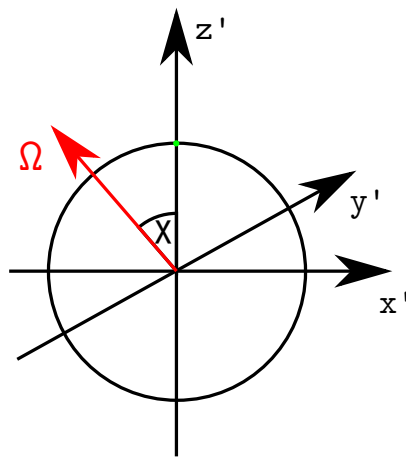

Figure 4.16: Coordinate system x', y', z' aligned with the location of the experiment. x' points from north to south, y' from west to east.

where $V(z')$ is a radial force acting on the particle and since the z' axis is aligned with the radial direction, this is purely a function of z'. Close to the surface $V(z') \approx mgz'$ which describes the classical Newtonian acceleration on the surface of the Earth. Using this potential in the case of the stationary Earth with $\dot{f}(\tilde{t}) = 0$ eq. (4.28) reduces to equation 2.1 and the solutions have been discussed in sec. 2.1.1. These solutions are now used to find the corrections to the energies of the stationary Schrödinger equation

$$E\psi' = \left(-\frac{\hbar^2}{2m}\nabla^2 + V(z') + i\hbar\omega \left((x'\cos(\chi) + z'\sin\chi)\,\partial_{y'} - y'(\cos(\chi)\,\partial_{x'} + \sin(\chi)\,\partial_{z'}) \right) \right)\psi' \quad (4.29)$$

for a state $\psi_n(x', y', z') = \psi_{x,y}(x', y')\psi_n(z')$ with energy E_n, the shift in energy due to an additional potential U can be calculated by using time independent perturbation theory $E_n = E_n^{(0)} + \Delta E_n \approx E_n^{(0)} + \Delta E_n^{(1)} = E_n^{(0)} + \int \psi_n^* U \psi_n$. In the case of the rotating Earth the potential U is given by the term including the $\dot{f}(t)$. The first order energy corrections are now given by

$$\Delta E_n^{(1)} = i\hbar\omega \left((\langle x'\rangle \cos(\chi) + \langle z'\rangle_n \sin(\chi))\,ik_{y'} - \langle y'\rangle(\cos(\chi)\,ik_{x'} + \sin(\chi)\langle\partial_{z'}\rangle) \right)$$
$$= -\hbar k_{y'}\omega\langle z'\rangle_n \sin(\chi) \quad (4.30)$$

where $\langle x'\rangle = \langle y'\rangle = 0$ at the origin and $\langle\cdot\rangle$ signifies the corresponding expectation value of the quantity in the brackets. Since the wave function in the z' direction is described by the bound state given by the real Airy functions $\langle\partial_{z'}\rangle = \int \psi\psi'\,\mathrm{d}z = \int \frac{1}{2}\partial_{z'}(\psi^2)\,\mathrm{d}z = 0$. As explained in appendix A $\langle z'\rangle_n = -z_0\frac{2}{3}\mathrm{AiZ}(n)$. With this the correction to the energy difference between two states m and n is given by

$$E_{nm} = E_n - E_m \approx E_n^{(0)} - E_m^{(0)} + \Delta E_n^{(1)} - \Delta E_m^{(1)} =$$
$$= E_n^{(0)} - E_m^{(0)} + \hbar k_y\omega\sin(\chi)\frac{2}{3}z_0\left(\mathrm{AiZ}(n) - \mathrm{AiZ}(m)\right) \quad (4.31)$$

The zeroth order energy differences are given by $E_n^{(0)} - E_m^{(0)} = -m_n g z_0\left(\mathrm{AiZ}(n) - \mathrm{AiZ}(m)\right)$. Using the fact that the neutron momentum is given by $p_y = \hbar k_y = m_i v_y$ leads to the first order transition energies

$$E_{nm} \approx \left(E_n^{(0)} - E_m^{(0)}\right)\left(1 - \frac{2p_y}{3m_g g}\omega\sin(\chi)\right) \quad (4.32)$$

where p_y is the momentum of the neutron and positive in the eastern direction. The direction of the neutron beam at the qBOUNCE experiment can be seen in fig. 4.17. Tracing the angle of the UCN beam leads to an angle of $\phi \approx 17.62(29)°$ in the westward direction. For neutrons with an average velocity of $9\,\mathrm{m\,s^{-1}}$ this leads to $v_y = -2.724(43)\,\mathrm{m\,s^{-1}}$. The location of the experiment is at a latitude such that $\chi \approx 45°10'0.01''$. This leads to corrected transition frequencies of about

$$E_{nm} \approx \left(E_n^{(0)} - E_m^{(0)}\right)\left(1 + \frac{1\cdot10^{-4} \pm 2.0\cdot10^{-6}}{g}\right) \quad (4.33)$$
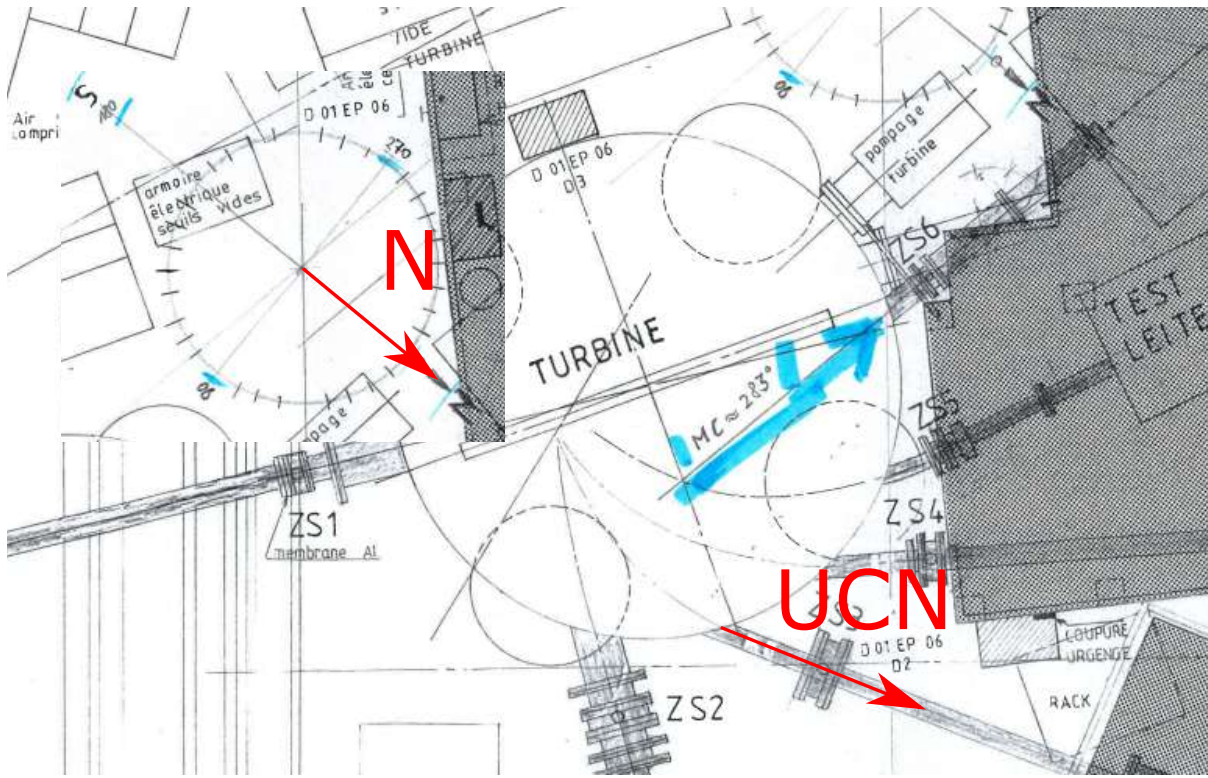
to first order.

Figure 4.17: Orientation of the neutrons beams at PF2. Direction of North and the UCN Beam marked in red. [53]

The transition energy of a neutron in a linear potential $V = m_g g' z$ is given by

$$E_{nm} = \left(\frac{\hbar^2 m_g^2 g'^2}{2m_i} \right)^{1/3} \left(\text{AiZ}(m) - \text{AiZ}(n) \right) \tag{4.34}$$

using this equation together with (4.33) and the zeroeth order energies leads to the modified local acceleration

$$g' = g \left(1 + \frac{1 \cdot 10^{-4} \pm 2.0 \cdot 10^{-6}}{g} \right)^{3/2} \tag{4.35}$$

The result in eq. (4.30) is surprising in so far as it is inconsistent with the classical expectation. The Hamiltonian in equation (4.28) can be written as [54]

$$H = \frac{p^2}{2m_i} + V(z) - \Omega \cdot L \tag{4.36}$$

where Ω is the angular velocity of the Earth, L is the angular momentum operator and p is the momentum. Now the Heisenberg equations of motion can be used to calculate the time derivatives of the

$$\dot{r}_i = \frac{1}{i\hbar} [r_i, H] = \frac{p_i}{m_i} - (\mathbf{\Omega} \times \mathbf{r})_i$$

$$\ddot{r}_i = \frac{1}{i\hbar} [\dot{r}_i, H] = 2 \left(\dot{\mathbf{r}}_i \times \mathbf{\Omega} \right) + \left(\mathbf{\Omega} \times (\mathbf{r} \times \mathbf{\Omega}) \right)_i + \frac{1}{i\hbar m_i} [p_i, V(z)] \tag{4.37}$$

where bold face letters indicate vectorial quantities and $\mathbf{\Omega}$ is the angular velocity of the Earth. This equation implicitly assumes, that $\mathbf{\Omega}$ is constant in time. Taking the expectation value of this gives the classical equation of motion for the expectation values of the position $\mathbf{r}$ and the momentum $\mathbf{p}$. In the

gravity aligned coordinate system $\mathbf{\Omega} = (-\omega \sin\theta, 0, \omega \cos\theta)^{\mathrm{T}}$. With $V(z) = -m_g\alpha/z$ the acceleration in the direction of gravity is now given by

$$\ddot{z} = 2\dot{y}\omega \sin\chi + z\omega^2 \sin^2\chi + x\omega \sin\chi \cos\chi - \frac{\alpha}{z^2} \tag{4.38}$$

Specialising to the surface of the Earth where $z = r_0$, $x = 0$ and $y = 0$ and defining $\alpha = r_0^2 g_0$ gives

$$\ddot{z}(r_0) = -g_0 + 2\dot{y}\omega \sin\chi + r_0\omega^2 \sin^2\chi$$
$$\Rightarrow \Delta g = -\left(2\dot{y}\omega \sin\chi + r_0\omega^2 \sin^2\chi\right) \tag{4.39}$$

comparing with the quantum mechanical shift of the energy to first order at the same point (here $\hbar k_y = p_y$ and $\langle x\rangle, \langle y\rangle = 0$ for convenience)

$$\Delta E_n^{(1)} = -\omega\hbar k_y\langle z'\rangle_n \sin(\chi) = -(\omega\langle z'\rangle \sin(\chi)m_i v_y + \omega^2\langle z'\rangle^2 \sin(\chi)^2 m_i$$
$$= -\frac{m_i}{m_g}(\omega \sin(\chi)v_y + \omega^2\langle z'\rangle \sin(\chi)^2)m_g\langle z'\rangle \approx \Delta g^{(1)}m_g\langle z'\rangle \tag{4.40}$$
$$\Rightarrow \Delta g^{(1)} = -\frac{m_i}{m_g}(\omega v_y \sin(\chi) + r_0\omega^2 \sin(\chi)^2)$$

shows a discrepancy. The obtained corrected energies from first order perturbation theory do not follow from a direct replacement of g in $V(z')$ for the quantum potential because the Coriolis force term is missing the factor of 2. While higher order perturbation theory might correct this deficiency there is a more convenient way to deal with this. The stationary Schrödinger equation with H as in (4.36) can be solved analytically. For this it is convenient to go back to a coordinate system where the z axis is aligned with the rotation vector $\mathbf{\Omega}$ of the Earth. Expressing the stationary Schrödinger equation in this coordinate system leads to

$$E\psi = \left(-\frac{\hbar^2}{2m_i}\frac{1}{r^2}\left(\partial_r r^2 \partial_r\right) + \frac{\mathbf{L}^2}{2m_i r^2} - \frac{\alpha}{r} - \omega L_z\right)\psi \tag{4.41}$$

Similar to the hydrogen atom in a weak magnetic field, here the wave function can be described as the product of a radial and an angular wave function $\psi(r,\theta,\phi) = \psi_n(r)\psi_{l\xi}(\theta,\phi)$, where the angular part satisfies

$$\mathbf{L}^2\psi_{l\xi}(\theta,\phi) = L_l^2\psi_{l\xi}(\theta,\phi) = \hbar^2 l(l+1)\psi_{l\xi}(\theta,\phi), l \in \mathbb{N}_0$$
$$L_z\psi_{l\xi}(\theta,\phi) = \hbar\xi\psi_{l\xi}(\theta,\phi), \xi \in \mathbb{Z} : -l \leq \xi \leq l \tag{4.42}$$

where $L_l^2 = \hbar l(l+1)$. Since both the $\mathbf{L}^2$ and L_z operators commute with the Hamiltonian, these quantum numbers are constants of the equation of motion(s) and therefore good quantum numbers. Plugging this Ansatz in the equation and dividing by the angular part results in

$$E_{nl\xi}\psi_n(r) = \left(-\frac{\hbar^2}{2m_i}\frac{1}{r^2}\left(\partial_r r^2 \partial_r\right) + \frac{L_l^2}{2m_i r^2} - \frac{\alpha}{r} - \hbar\omega\xi\right)\psi_n(r) \tag{4.43}$$

On the surface of the Earth the L^2 and potential part can be expanded around the radius of the Earth, here called r_0. Introducing a new coordinate via $r = r_0 + z$ and expanding around $z = 0$ gives

$$\frac{L_l^2}{2m_i r^2} \approx \frac{L_l^2}{2m_i r_0^2} - \frac{L_l^2}{m_i r_0^3}z$$
$$\frac{\alpha}{r} \approx \frac{\alpha}{r_0} - \frac{\alpha}{r_0^2}z \tag{4.44}$$

Additionally, introducing a new function $\tilde{R}_n(r) = r\psi_n(r)$ results in

$$E_{nl\xi}\tilde{R}_n(r) = \left(-\frac{\hbar^2}{2m_i}\partial_r^2 + \frac{L_l^2}{2m_i r^2} - \frac{\alpha}{r} - \hbar\omega\xi\right)\tilde{R}_n(r) \tag{4.45}$$

Expressing this with the new coordinate z defining $\alpha = m_g r_0^2 g_0$ and using the linear approximations gives

$$
\left(-\frac{\hbar^2}{2m_i}\partial_z^2 - \frac{L_l^2}{m_i r_0^3}z + m_g g_0 z - \xi\hbar\omega + \frac{L_l^2}{2m_i r_0^2} - m_g r_0 g_0 - E_{nl\xi} \right) R_n(z) = 0
$$
$$
\Rightarrow \left(-\frac{\hbar^2}{2m_i}\partial_z^2 + m_g g z - E'_{nlm} \right) R_n(z) = 0
\tag{4.46}
$$

where

$$
R_n(z) = \tilde{R}(r_0 + z)
$$
$$
g = g_0 - \frac{L_l^2}{m_i m_g r_0^3}
\tag{4.47}
$$
$$
E'_{nl\xi} = E_{nl\xi} + \xi\hbar\omega - \frac{L_l^2}{2m_i r_0^2} + m_g r_0 g_0
$$

This is the Airy differential equation that has been discussed previously. Imposing the boundary condition $z \geq 0$ leads to the energies

$$
E'_{nl\xi} = -\mathrm{AiZ}(n)\sqrt[3]{\frac{\hbar^2 m_g^2 g^2}{2m_i}}
$$
$$
\Rightarrow E_{nl\xi} = -\mathrm{AiZ}(n)\sqrt[3]{\frac{\hbar^2 m_g^2 \left(g_0 - \frac{L_l^2}{m_i m_g r_0^3} \right)^2}{2m_i}} - \xi\hbar\omega + \frac{L_l^2}{2m_i r_0^2} - m_g r_0 g_0
\tag{4.48}
$$

This gives the effective $g' = g_0 - \frac{L_l^2}{m_i m_g r_0^3}$. To compare to the classical acceleration (4.38) $\mathbf{L} = \mathbf{r} \times \mathbf{p}$ can be calculated at the point $\mathbf{r} = (0,0,r_0)^{\mathrm{T}}$ and using $\mathbf{p} = m_i(\dot{\mathbf{r}} + \boldsymbol{\Omega} \times \mathbf{r})$ from (4.37). Going through the calculation gives

$$
g' = g_0 - \frac{m_i}{m_g}\left(2\dot{y}\omega\sin(\chi) + r_0\omega^2\sin(\chi)^2 + \frac{v^2}{r_0} \right)
$$
$$
= g - \frac{m_i}{m_g}\left(2\dot{y}\omega\sin(\chi) + \frac{v^2}{r_0} \right)
\tag{4.49}
$$
$$
= g - \frac{m_i}{m_g}\left(2.68 \cdot 10^{-4} \pm 4 \cdot 10^{-6} \right) \mathrm{m/s^2}
$$

where g is the acceleration felt by a resting particle on the surface of the rotating Earth, $\dot{\mathbf{r}} = (\dot{x}, \dot{y}, \dot{z})^{\mathrm{T}}$ and $v = \sqrt{\dot{\mathbf{r}} \cdot \dot{\mathbf{r}}}$. In particular the shift induced by $\Delta g_{\mathrm{centrifugal}} = g - g_0 = r_0\omega^2\sin(\chi)^2 \approx 0.016\,84\,\mathrm{m/s^2}$ for $r_0 \approx 6370\,\mathrm{km}$ and $\chi \approx \pi/4$. In terms of frequency this gives a shift in $\Delta\nu_{|1\rangle\to|6\rangle} \approx 1.113\,\mathrm{Hz}$. This shift is also present in a classical measurement and needs to be excluded from any comparison with a classical measurement. Also it is a "non existent" shift since it compares a non rotating Earth with a rotating one. This result is perfectly consistent with the classical expectation including the factor of 2 for the Coriolis force in eq. (4.37). Therefore it is admissible to expect the classical value of g determined by a classical acceleration to be the term determining the transition frequencies of the Airy functions describing the neutron.

4.2.4 Tidal Forces

The gravitational environment on the surface of the Earth is subject to many perturbations. One commonly observed phenomenon is the tidal force exerted by the Moon and the Sun. These can be calculated perturbatively and there is an interplay between the effect of the Moon and the Sun over the course of a month. The tidal acceleration due to the Moon and the Sun have been shown in [8] to contribute an acceleration of about $\frac{\delta g}{g} \approx 1.5 \times 10^{-7}$, where this is the sum of the Sun and Moon contributions i.e. spring tide.

4.2.5 Relativistic effects in an accelerated frame

Due to the Dirac nature of neutrons there is a slight modification to the expected neutron energies. To calculate this effect in full, a proper treatment of Dirac particles in a rotating lab frame on the surface of the Earth is needed. The theoretical calculations for fictitious forces with the Dirac equation is highly technical and the eigensolutions for a system comparable to qBOUNCE have not been found in the literature. In [55] a simplified model is considered in great detail, where explicitly the energies of a Dirac field, a Klein-Gordon field and the non relativistic Schrödinger particle on top of a mirror are given and compared. The treatment deals with a particle in a reference frame that undergoes a constant acceleration called the Rindler frame. These gives the eigenenergies

$$E_n^D = -g\hbar \left(\sqrt[3]{\frac{m_n}{2g\hbar}} \mathrm{AiZ}\,(n) + \frac{1}{6}\sqrt[3]{\frac{g^2\hbar^2}{2m_n^2}} \mathrm{AiZ}\,(n) - \frac{1}{60}\sqrt[3]{\frac{2g\hbar}{m_n}} \mathrm{AiZ}\,(n)^2 - \frac{g\hbar}{m_n}\left(\frac{\mathrm{AiZ}\,(n)^3}{700} - \frac{1}{12} + \frac{1}{70} \right) \right) \tag{4.50}$$

Comparing the transition frequencies for $|1\rangle \to |6\rangle$ gives

$$\Delta\nu_{16} = \frac{E_6^D - E_1^D - (E_6 - E_1)}{2\pi\hbar} \approx -4.494 \times 10^{-12}\,\mathrm{Hz}\,, \tag{4.51}$$

where this does not take the spin 1/2 nature of the neutron to a rotating frame but to a constantly accelerated frame [55]. In particular it has not been investigated if the geometric factors appearing in a rotating frame influence a Dirac field fundamentally different than spin 0 particles. Whether or not the rotation induced shift of the bound GRS state energies has any large dependence on spin is not yet clear.

4.2.6 External masses

Additional masses next to the experiment induces shifts in the energy spectrum of the bound states. A mass distribution $\rho(\mathbf{r})$ gives an additional contribution as a potential in the Schrödinger equation

$$\delta V(\mathbf{r}) = -\int_{\mathbb{R}^3} \frac{Gm_g\rho(r')}{|r - r'|}\mathrm{dV}' \approx -\int_{\mathbb{R}^3} \frac{Gm_g\rho(r')}{|r'|}\mathrm{dV}' - \mathbf{r} \cdot \int_{\mathbb{R}^3} \frac{Gm_g\mathbf{r}'\rho(r')}{|r'|^3}\mathrm{dV}' + \mathcal{O}(|r'|^{-3}) \tag{4.52}$$

where the approximation is valid at the origin. Using the term linear in z and adding it to $V = m_n gz$ gives

$$V_{eff}(z) = m_g g_{eff} z = m_g \left(g - \int_{\mathbb{R}^3} \frac{Gz'\rho(r')}{|r'|^3}\mathrm{dV}' \right) z = m_g \left(g - Gm'\frac{z'}{|r'|^3} \right) z \tag{4.53}$$

where the last equality holds for a point mass m' at location r'. This shows the expected result that the acceleration g is modified by the additional acceleration caused by the added mass and in general complicated integrals appear, since the mass is not centred around the origin, but far away. As a relevant example the shift due to a mirror plane with mass m' and thickness d just below the neutron can be calculated. The shift of g is given by

$$\delta g_{eff} = -\frac{Gm'}{lwd} \int_{x=-l/2}^{l/2} \int_{y=-w/2}^{w/2} \int_{z=-d}^{0} \frac{z'}{|r'|^3}\mathrm{dV}' \approx 5.3 \times 10^{-8}\,\mathrm{m/s^2} \tag{4.54}$$

for $m' = 30\,\mathrm{kg}$, $l = 1\,\mathrm{m}$, $w = 20\,\mathrm{cm}$, $d = 5\,\mathrm{cm}$, which corresponds roughly to the geometry of qBOUNCE. Additional masses can be included in the same manner, but the weakness of gravitation and the finite density of standard matter on Earth can only provide limited shifts. A 1000 kg point mass 1 mm below the neutron gives $\delta g_{eff} \approx 6.7 \times 10^{-2}\,\mathrm{m/s^2}$ which is already hard to achieve using ordinary matter. Assuming a ball of 1 mm radius this corresponds to a density of $2.4 \times 10^8\,\mathrm{g/cm^3}$ which lies comfortably between white dwarf and neutron star densities. This shift is an over estimation, since the linearisation and description using Airy functions is not strictly accurate in this case.

4.3   Discussion

qBOUNCE uses a very simple system to perform spectroscopic measurements. The only parameters entering the Schrödinger equation describing the system 2.17 are the mass of the neutron, $\hbar$, the local gravity acceleration g and the oscillation parameters $a\omega$ and ν. Performing spectroscopic measurements should accurately determine the energy differences between states, allowing an inference of the size of g. As was shown in this chapter there are a host of systematic effects when performing the actual experiment.

The table 4.1 collects all of the systematic shifts arising either due to real shifts of g, shifts from the quantum nature of the system or from experimental limitations. The shifts are real in the sense that they shift the observed transition frequency from the expected frequency $f_{|i\rangle \to |j\rangle} = (E_j - E_i)(2\pi\hbar)^{-1}$ obtained from the energies of the eigenstates with a specific value of g to some new value. The sign is chosen such that if the measurement (which includes systematic shifts) is higher than the measurement without shift the shift is positive. It then follows that in order to extract the value for g the systematic shift has to be subtracted from the measured value.

$$g_{\text{true}} = g_{\text{measured}} - \delta g_{\text{sys.}} \tag{4.55}$$

It is important to note that some effects describe a shift in g as in the case of the Coriolis force, while others give a shift in ν like the magnetic field gradient or the clock reference. These are equivalent only when viewing a single transition frequency. A constant frequency shift for all frequencies has a different influence on g depending on the transition since $g \sim \nu_{ij}^{\frac{3}{2}}$. Since $|1\rangle \to |6\rangle$ was statistically the most observed transition in the past cycles, all effects in the table below are calculated here for this transition. When observing multiple transitions one has to take care to recalculate the correct shifts for the corresponding transition. If a shift of g is observed for one transition other transitions can be used to determine whether it is a shift of g or ν since they are not linearly dependent.

The shifts calculated here are evaluated in absolute terms for the transition $|1\rangle \to |6\rangle$. The statistical shifts $\sigma g_{sys.}$ are shifts that are statistically random. This is the phase offset and the clock accuracy as well as the uncertainty in the direction of the neutron velocity. These can be reduced by improving or changing the experimental setup.

The systematic shifts $\delta g_{sys.}$ are shifts that change the transition ν or g by a constant value. These can change with the observed transition as is the case with the spectator state shift or be constant as is the case with the centrifugal force.

The largest effect currently known to qBOUNCE is the uncertainty of the phase used for the excitation, giving clear indication that the limits of Ramsey GRS in qBOUNCE at this moment is given by the ability to control the phase of the two mirrors. As described in 5.2.3 there was a classical reference measurement of g made, directly next to qBOUNCE . The phase uncertainty is directly contributing to the difference between this classical measurement and the GRS measurement. From 4.1.1 such a phase offset is independent of the transition so it can be excluded by determining the transition frequencies of two transitions, preferably as far separated in frequency as experimentally possible.

At the current measurement precision this phase effect is still a factor of 2 smaller than the statistical error on the frequency but to make further improvements of this method this experimental parameter has to be more strictly controlled. Furthermore the spectator-state shift and the Bloch-Siegert-shift become important so an in depth numerical analysis will be important to go below a precision of $\approx 6.4 \times 10^{-4}\,\mathrm{m/s^2}$ or $\approx 4.2 \times 10^{-2}\,\mathrm{Hz}$. At that point a significant deviation from the classical value is expected.

Expectations for the measured value of g with neutrons using GRS are expected to give the same result as a classical measurement. This is true to a value of $\sigma g/g \approx 6 \cdot 10^{-5}$ of relative statistical deviation beyond which the multi state system in a Ramsey type spectrometer has to be taken into account fully. These are on the same order of magnitude as a $1°$ phase offset for the two oscillating regions which is on the same order of magnitude as the statistical precision that has been reached by qBOUNCE .

If there is an offset from the expected value, there are still measurements that can be performed. In some cases one can investigate an introduced shift in the transition frequency. This would be the case for a potential neutron charge **??**, or with spin dependent spin-gravity coupling $\propto \vec{\sigma} \cdot \vec{g}$. In these cases precision measurements can be performed regardless of the absolute value of the transition frequency, since only a relative shift is investigated.

Table 4.1: A summary of the discussed systematic effects. In the last line the expected deviation from reference measurement using a corner cube is given. This is valid only when comparing to $f_{|1\rangle \to |6\rangle} = (E_6 - E_1)(2\pi\hbar)^{-1}$, in an analysis using a multi-state system the spectator state shift and Bloch-Siegert shift marked with ***** are already included.

Effect	$\delta g_{sys.}[\mathrm{m/s^2}]$	$\sigma g_{sys.}[\mathrm{m/s^2}]$
Phase offset	$< 6.4 \cdot 10^{-4}$	$6.4 \cdot 10^{-4}$
Spectator state shift and Bloch-Siegert shift*****	$-2.1 \cdot 10^{-4}$	$1 \cdot 10^{-4}$
Coriolis & centrifugal (movement of the neutron)	$2.68 \cdot 10^{-4}$	$4. \cdot 10^{-6}$
Geometric transmission losses	$< -7.6 \cdot 10^{-5}$	0
B field gradient	$< -5.2 \cdot 10^{-6}$	0
Tidal forces	$\leq 1.5 \cdot 10^{-6}$	0
Mass of Neutron mirrors close by	$5.3 \cdot 10^{-8}$	0
Mirror penetration	$-3.62 \cdot 10^{-8}$	0
Tilt of the experiment	$-5. \cdot 10^{-10}$	0
Clock accuracy	0	$1.5 \cdot 10^{-12}$
Relativistic correction in Rindler frame	$-6.9 \cdot 10^{-14}$	0
Total	$6.1 \cdot 10^{-4}$	$6.5 \cdot 10^{-4}$
Effect	$\delta \nu_{sys.}[\mathrm{Hz}]$	$\sigma \nu_{sys.}[\mathrm{Hz}]$
Phase offset	$< 4.23 \cdot 10^{-2}$	$4.23 \cdot 10^{-2}$
Spectator state shift and Bloch-Siegert shift*****	$-1.4 \cdot 10^{-2}$	$6.8 \cdot 10^{-3}$
Coriolis & centrifugal (movement of the neutron)	$1.77 \cdot 10^{-2}$	$2.64 \cdot 10^{-4}$
Geometric transmission losses	$< -5.02 \cdot 10^{-3}$	0
B field gradient	$< -3.44 \cdot 10^{-4}$	0
Tidal forces	$\leq 9.92 \cdot 10^{-5}$	0
Mass of Neutron mirrors close by	$3.5 \cdot 10^{-6}$	0
Mirror penetration	$-2.39 \cdot 10^{-6}$	0
Tilt of the experiment	$-3.31 \cdot 10^{-8}$	0
Clock accuracy	0	$9.91 \cdot 10^{-11}$
Relativistic correction in Rindler frame	$-4.55 \cdot 10^{-12}$	
Total	$4.2 \cdot 10^{-2}$	$4.3 \cdot 10^{-2}$

Chapter 5

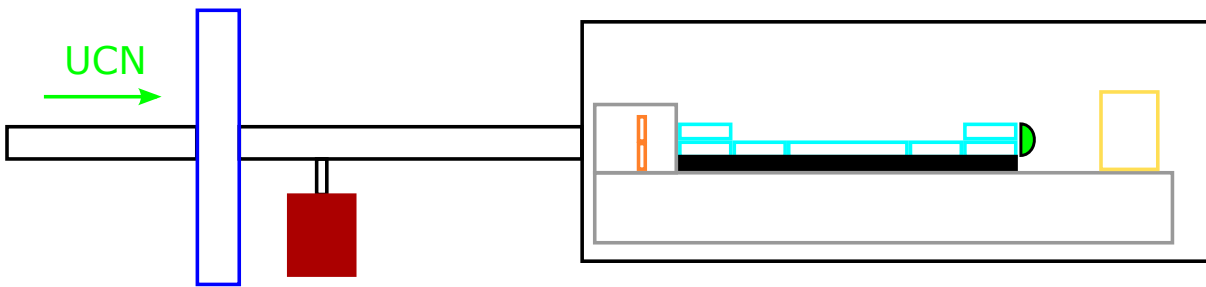# Measurements And Results

5.1 Overview

Figure 5.1: Sketch of the general layout of qBounce. The UCNs (green) enter from the left through beam guides (black). Downstream of a lead wall shielding (dark blue), the monitor detector (red) is mounted. The large box to the right represents the doubly μ-Metal shielded vacuum chamber. On the bottom is the granite and above it a BAl shielding to suppress background (grey). Inside the BAl shielding are the velocity selection blades (orange). The five sections containing mirrors and scatterers are shown in blue, they are mounted on piezo tables (black). Finally there is the detector D (green). Finnaly the location of the internal laser interferometer (yellow) is shown.

A general overview of the experiment can be seen in fig. 5.1. The UCNs are provided by the PF2 turbine and enter a beam tube connecting the turbine to the qBOUNCE experiment. Just behind the lead wall the monitor detector is mounted to a 4 mm hole in the beam tube. From the neutron flux inside the beam tube a small fraction of neutrons is able to leave the guide and enter the monitor detector. This provides a direct measurement of the neutron flux to the experiment. In case of unforeseen variations of the flux the monitor provides a direct method to correct the measured rates. This is of vital importance, since qBOUNCE measures the transmission through the experiment. If the reactor were to shut off we would think that we perform the best Ramsey ever without being able to correct it.

In addition to the monitor detector ("monitor") measuring the neutron density in the beam tube there is the main detector ("detector") at the end of the experiment measuring the transmission through the experiment. They have been described in the section 3.3.2. They both have an effective background which is reactor dependent. The background is assumed to be only weakly time dependent during one cycle, but the backgrounds in different cycles are treated as independent.

The monitor is a Helium-3 detector with a gas mixture filled at regular maintenance intervals. Over time the He-3 content changes slowly due to leakage, which changes the overall efficiency and characteristics. Furthermore the general background radiation from the reactor changes from one cycle to the next. Depending on the targeted number of days for every cycle, the reactor power is adjusted to make the fuel element last for the whole cycle. Typically the cycle times are between 40 and 60 days. The power
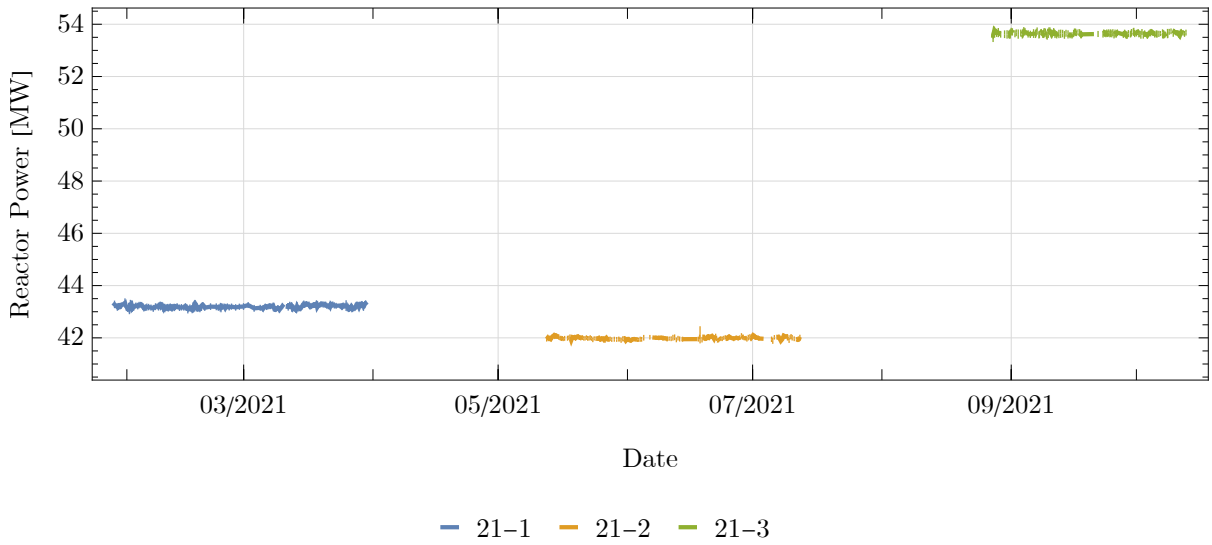
Figure 5.2: Power of the reactor for the three cycles in 2021. The supporting measurements with neutrons were chiefly done in 21-1. Dataset 1 is from cycle 21-2 and dataset 2 from 21-3.

for the three cycles in 2021 can be seen in fig. 5.2. The precise output performance and background level of the monitor is thus cycle dependent in a non trivial way. The cycles used for the supporting measurements and the datasets 1 and 2 correspond to the cycles 21-1, 21-2 and 21-3 respectively. The monitor measurements in 5.3 show that there is a time structure of the monitor rate over the whole cycle. This variation is like to be cause by geometric effects in the reactor. At the 1% level these variations are not visible in the data taken by the neutron counter in qBOUNCE .

For each reactor cycle the monitor and detector backgrounds are determined by at least one dedicated measurement. In the past the background was measured continually see [13, 21]. With this the measured rates from the detector r_d are corrected to

$$r_{corr} = \frac{r_d - r_{dbg}}{r_m - r_{mbg}} \langle r_m \rangle \tag{5.1}$$

where r_{dbg} is the background rate of the detector, r_m the monitor rate r_{mbg} the monitor background and $\langle r_m \rangle$ is the average of the monitor rate over the whole cycle. The scaling with the mean rate of the monitor is done only for ease of conversation. The subtraction is equivalent of a dark frame correction and the division to a flat field correction. This is done to maintain a constant zero rate transmission throughout the cycle. It is assumed that the behaviour of the detector and the monitor scale the same with the reactor power or delivered neutrons from the reactor. This means that choosing one specific experimental setting should yield statistically indistinguishable results even if the reactor power should vary when correcting via 5.1. The measured rates of qBOUNCE with the main detector are typically on the level of $\sim 5\%$ in precision, so the 1% variation of the monitor rate is not contributing strongly to the final result.

The first cycle in 2020 was dedicated to the investigation of influences of experimental details on the measurable Ramsey transition. At this point the transition $|1\rangle \rightarrow |6\rangle$ was established and numerical calculations suggest an absence of a large spectator state shift. Because of this the measurements were all focused around $\nu_{16} \approx 972.345$ Hz. Additionally the increase in frequency provides a decreased relative error for the same time spent determining a transition frequency compared to previous measurements in [6, 8, 13, 21].

There were mainly two effects investigated in detail: the influence of the velocity spectrum on the state distribution after section I and the influence of steps between the different mirrors. In the past qBOUNCE did investigations with CR39 track detectors to look at the change of occupation numbers for
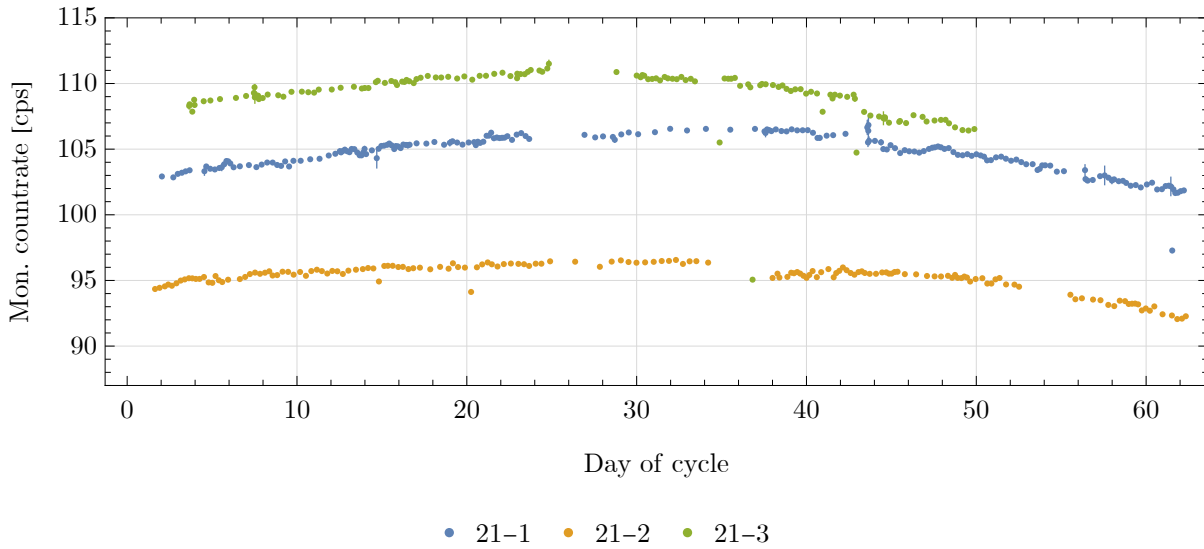
Figure 5.3: Measured rates of the monitor detector. A clear 1% variation over a cycle can be seen in all three cycles of 2021. The most probable explanation for this is the changing geometric illumination of the vertical source.

different velocities. These indicated that there is no change in state occupation when leaving the mean velocity of the neutrons the same.

For GRS measurements there is a trade off between state occupation, spectator state shift effects and width of the transitions. All of these are dependent on the velocity spectrum: the state preparations works more efficiently for slower neutrons, changing the state occupation which leads to a changed spectator state shift. From 2.38 higher velocity means usually a broader Ramsey transition curve since the interaction time gets smaller. During this cycle measurements with restricted velocity intervals were performed. As a metric in 5.3.1 the statistical error scaled to a one day reference time is used. The second effect investigated was the effect of steps between mirrors on the transition frequency. Under normal operating conditions the whole setup is aligned so that the stepsizes are $< 0.5\,\mu\mathrm{m}$ in height as explained in more datail in 3.3.7. With the zero step alignment the six ramsey points were taken. In addition two more sets of ramsey measurements were performed: one with $1\,\mu\mathrm{m}$ steps between the mirrors and one with $-1\,\mu\mathrm{m}$. This can be seen in fig. 5.7. In effect this causes a total step height of $4\,\mu\mathrm{m}$ distributed across the four moveable mirrors. The three measurements can be seen in 5.3.3. A comparison of the three step configurations can be seen in fig. 5.11.

5.1.1   Cycle 212

In this cycle the goal was to perform detailed measurements of the transition $|1\rangle \to |6\rangle$. In addition the transition $|2\rangle \to |7\rangle$ was considered but due to time constraints only looked at for a shorter time. Finally the setup was changed to enable measurements with spin polarized neutrons. This involved a replacement of the detector, implementation of the guide magnetic field and a drastic limitation of the count rate to improve the spin selection efficiency of the detector. Because of this the statistical significance of these measurements is not very high, but nevertheless provides the possibility to obtain constraints on spin gravity couplings. A general characterisation of the spin detection efficiency of the detector used in qBounce can be found in appendix C.

5.1.2   Cycle 213

During this cycle the transition $|1\rangle \to |6\rangle$ was observed in an unbiased mode. As the central frequency $\nu_{16} = 972.345\,\mathrm{Hz}$ was used, and then steps of the expected width $w_\nu \approx 4.3\,\mathrm{Hz}$ were taken, to the left and

to the right. there were no further considerations taken with respect to the locations of the measured points. To the right the transition $|2\rangle \rightarrow |8\rangle$ was included and to the left $|3\rangle \rightarrow |9\rangle$. From this the presence of $|3\rangle$ in the initial state can be inferred, as well as directly seen in fig. 5.21

5.2 Supporting measurements

As the first measurements of every cycle the rate through the setup without any applied oscillation is measured. Depending on the settings of the velocity selection, the reactor power, the detector efficiencies and the state of the mirrors the rate through the setup gives an indication of gross errors during initial setup. At this point the decision to recheck the system is made. If the rate is not high enough (meaning at approximately a value that has been seen before) the vacuum chamber has to be reopened and the error is fixed. This usually involves checking the alignment and cleanliness of the mirrors or whether or not a mirror exploded.

Special care is taken to make sure the vacuum system is still performing sufficiently well, the mirrors are aligned, the mirrors are clean and the detector gas supply is sufficient, the settings for the detector electronics (amplification voltages) is correct and that the interferometer is working.

After the initial rate measurement the system is ready for data taking. Over the course of each reactor cycle/measurement campaign the neutron rate without oscillations is checked periodically. This ensures a consistent measurement environment and detects gradual changes in the experiment like vacuum degradation [13, 21] or misalignment. Furthermore the detector background without a direct neutron beam is measured at least once every reactor cycle.

5.2.1 Determination of velocity spectrum

As described in ch. 3.3.4 the velocity of the neutrons is determined by assuming classical flight parabolas for the neutrons. Different external circumstances make it necessary to re-evaluate the velocity spectrum from time to time. First changes to PF2 and the beam guide setup from the UCN turbine to the experiment may shift the spectrum to the experiment. Second intrinsic changes to qBOUNCE can also change the velocity spectrum. Mainly this is expected when changing the geometric layout of the experiment. In 5.1 the precise positioning can change due to space limitations or an effort in optimisation, for example changing the distance of the velocity blades to the first mirror section. This was done to optimise the sensitivity with which faster neutrons can be cut off. In these cases the velocity spectrum was remeasured. This happened multiple times in 2019. At the end of 2019 the beam guides of PF2 were renewed so the velocity spectrum was retaken in the first cycle of 2020 this data was analysed in 3.3.4. This final spectrum can be seen again in 5.4.

Comparison with [13, 21] shows that the spectra within qBOUNCE lead to similar results. The characteristic quantities of the fitted Maxwell-Boltzmann spectrum give compatible results: no significant change in the velocity spectrum within qBOUNCE was observed since 2017. Improvements to the installation PF2 could result in a higher flux, where a renewed measurement of the velocities would be advised.

5.2.2 Clock Reference

The most important parameter for qBOUNCE is time, both for the frequency and the relative phase between the oscillating sections II and IV. In the past this was controlled by two different devices, the interferometer used its internal clock and the function generator its own internal clock. Due to software limitations the interferometer timebase was unstable at the $\approx 10^{-5}$ level. The reason for this is that the interferometer takes the largest multiple of its internal time base that is still smaller than the desired time base derived from the sample frequency. Depending on the sample frequency, different offsets are possible and at special frequencies the offset is 0. At a sampling rate of $\sim$ kHz and an internal base clock of ~ 10 MHz a relative shift in the frequency of $\lesssim 10^{-4}$ is expected. This was confirmed in a cross-check as the approximate offset between function generator and interferometer.

To remedy this, in the summer of 2020 the decision was taken to replace all internal frequency clocks in the experiment with a rubidium time standard. As described in 3.3.8 the device used is a SRS FS740
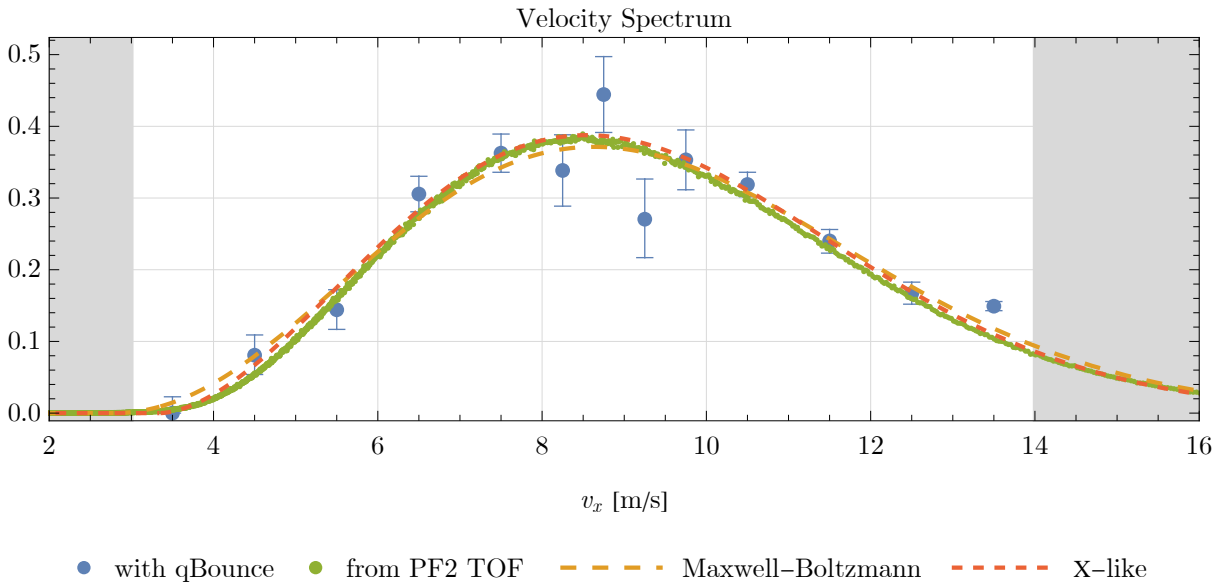
Figure 5.4: Velocity spectrum from measurements with qBOUNCE and from. Fits for a χ-distribution and from a modified TOF spectrum are shown.

10 MHz GPS Frequency Reference. The frequency of this clock was compared to another Rb clock that is synchronised to the GPS time standard. The agreement was $< 10^{-10}$ with the synchronised clock. Using the Rb clock as a time standard the AFG and the interferometer agree to the accuracy of the function generator. It generates frequencies with 1 mHz resolution that can be resolved with the interferometer. At a frequency of 1 kHz this gives a relative accuracy of $\approx 10^{-6}$. For higher relative accuracy the function generator will have to be replaced with a more accurate model. The timing accuracy of the Rb clock eliminates any need for more timing precision for the foreseeable future.

5.2.3 Determination of the local classical acceleration of the Earth

In October 2021 Ludger Timmen from the university of Hannover performed absolute gravity measurements at the ILL. These were done using the instrument FG5X-220 in one of the basements of the ILL. These absolute measurements were then transferred to various locations at the ILL using the relative meters Scintrex CG-3#4493 and CG-6#171 in August and October 2021. Of interest for qBOUNCE there were two particular points, one located in the reactor hall next to the turbine and one next to the vacuum chamber of qBOUNCE . This provides the best value to compare to the results obtained by the qBOUNCE experiment. It includes all corrections made due to the rotation of the Earth, tidal effects and the local mass distribution due to equipment around the experiment. All remaining corrections to the value obtained by this are due to the proper movement of the neutrons as explained in 4.2.3.

The last time g was measured at PF2 was in 1998 at the VCN cabin [56]. This measurement obtained a value of $g_{1998} = 9.805\,07(2)\,\mathrm{m/s^2}$. The recently measured acceleration gives These show that an approximate local acceleration of $g \approx 9.805\,\mathrm{m/s^2}$ is justified and the value from 1998 is reasonably accurate. The variations from location to location are the on the same order of magnitude as the variation from 1998 to 2021. A detailed report to these measurements with analysis and explanations can be found in [16]. For qBOUNCE this provides an accurate reference to which to compare the obtained results.

Table 5.1: Measured values of g in August and October 2021. Details in [16], ILL1 Basement is measured absolute with the falling corner cube FG5X-220, this was then transferred to the other locations using CG-3#4493 and CG-6#171.

Position	g [μm/s²]	σ_g [μm/s²]
ILL1 Basement	9804975.61	0.03
PF2 floor	9804924.69	<0.1
Next to qBOUNCE	9804916.47	<0.1

5.2.4   Countrate stability of the monitor detector

The neutron flux in the experiment is roughly linearly dependent on the reactor power. The ILL has a variable reactor power, depending on the time scheduled for one reactor cycle. The actual reactor power for each cycle is scaled to burn off one fuel element in the planned time. Because of this measurements taken in different cycles are not directly comparable.

Additionally there is a small shift in the neutron rate over the course of a reactor cycle. This can be seen in fig. 5.3. These figures show the rate of the monitor detector over time in blue and the reactor power in orange. A slight variation of about $\pm 2\%$ is visible over the course of the cycle, without being also present in the reactor power. The current explanation is an intricate geometric effect: in fig. 3.1 the vertical cold source is illuminated by the fuel element. Over time the control rod is removed to keep the neutron flux constant, changing the solid angle illuminating the deuterium volume cooling the neutrons. This leads to a percent level variation in UCN flux measured by the qBOUNCE monitor detector. In the raw detector data of the ramsey experiment this is not visible since most of the measurements have an accuracy on the 5% level. This variation is taken into account by the normalising procedure described with eq. (5.1)

5.3   Optimisation And Systematic Checks

Since the beginning of qBOUNCE there have been known sources of impediments that hamper progress. One problem plaguing qBOUNCE since its inception has been the quality of the vacuum in the experiment. Neutrons are absorbed by hydrogen present in the vacuum chamber. There are a few sources: first the air in the reactor building contains water and dust leading to a direct contamination every time the vacuum chamber is opened. The location and size of the chamber make it impossible to completely avoid contamination. The mirrors in the experiment are cleaned after every time the chamber is opened. In addition oil free equipment is used and silicon free vacuum grease is used to avoid creeping of the oil onto the mirror surfaces.

Second there were borated plastic mats in use as shielding material for the velocity blades and the detector. These are easy to use since they can be easily cut and shaped. Within qBOUNCE there has been the suspicion that these mats gas out. Initially this was dismissed because at the ILL they are in frequent use as neutron absorbing padding in the SANS machines. After discussions with C. Dewhurst from the ILL it was found out that the SANS machines operate at rough vacuum $\sim 1 \times 10^{-2}$ mbar. After this discussion their use in qBOUNCE was phased out since it is believed that the higher vacuum leads to out gassing which contaminates the vacuum. This has reduced the reduction in zero rate while the vacuum chamber is closed to a statistically unmeasurable effect.

Nevertheless a thorough cleaning of the chamber has been necessary every two to three years where all components are cleaned and the complete experiment is remounted. This involves a lot of effort, since there are over 1500 threaded inserts on the mounting granite.

The precise origin of the residual oil is not known but the best hypothesis thus far is that the air inside the reactor contains traces of machine oil. This oil is pumped through the vacuum system where it slowly accumulates: the turbo pump pushes the residual oil to the backing pump side, where the higher pressure causes it to condense. This mechanism causes the oil content on the backing side to increase and

diffusion into the main chamber increases slowly over time. Every time the chamber is returned to air pressure this remaining oil is deposited as a thin film over the complete chamber where it causes neutron absorption. Over time the vacuum degrades and the neutron rate finally drops significantly. This has been the source of major cleaning efforts over the years.

As an additional measure dust has to be limited in the experiment. To avoid the accumulation of dust from the air on the surfaces of the mirrors a flow box with a HEPA filter is mounted in a way that limits the inrush of particles when opening the chamber, which seems to help the general effort.

The final reachable accuracy of qBOUNCE gives rise to many avanues to persue when trying to improve the efficiency of every neutron during a beam time. As discussed in 4 some of these might change the observed transition frequencies while others could improve the statistical efficiency. Measurements investigating these will be described in this chapter.

5.3.1 Sensitivity Vs. Velocity Spectrum

The precise mechanism by which the neutron ground state is selected is highly dependent on the velocity of the neutrons. As was shown in 2.2 an intuitive approximation is possible, but the precise details are non trivial. Therefore the expected measurement contrast is also susceptible to variations in the velocities of the neutrons. In [13] measurements indicate that for the current qBOUNCE iteration this is not influencing the result. We have performed measurements to investigate this.

The velocity spectrum is set up to contain most of the spectrum provided by PF2. With the velocity selection the unwanted velocity components can be cut to provide a limited picture. For the Ramsey fringe with fixed velocities it was tested if the spectrum has an influence on the measured contrast. Since (in the two state approximation) this only depends on the difference in occupation numbers the measured contrast in a transition should reflect this. To evaluate the general dependence of the contrast three measurements have been performed: one form $v \in [4; 9.5] \mathrm{m\,s^{-1}}$ another from $v \in [4; 14] \mathrm{m\,s^{-1}}$ and the last from $v \in [4; 7.5] \mathrm{m\,s^{-1}}$. These velocities were chosen to reflect the full spectrum, the limited spectrum needed for magnetic field measurements and a value in between. A simple sweep of frequencies and phases (6 points) at a fixed oscillation strength has been performed. As a metric here the sensitivity per day is shown in fig. 5.5 by rescaling the obtained error for the transition frequency with $\sqrt{T}$ for a total measurement time T. This was then used to determine the optimal velocity distribution for the next cycle 212. Because of time constraints only these three points could be addressed, resulting in the minimum for the achievable sensitivity according to these measurements.
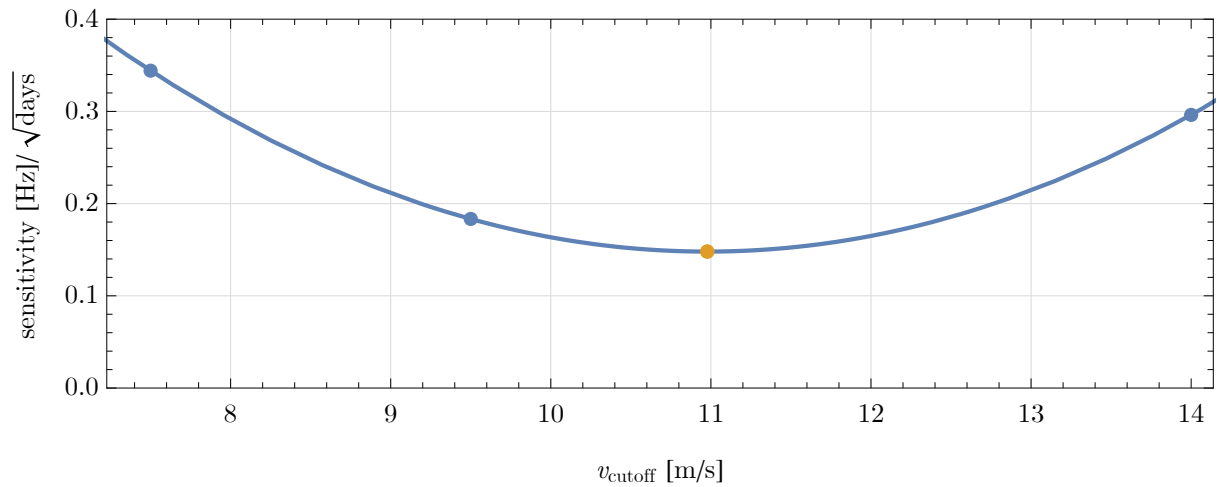
Figure 5.5: Normalised sensitivities for different cut-off velocities v_{cutoff}. The point at $14\,\text{m s}^{-1}$ represents the full spectrum, the point at $7.5\,\text{m s}^{-1}$ is the cut-off velocity for the spin dependent detector and the point at $9.5\,\text{m s}^{-1}$ includes approximately half of the neutron spectrum. From these three points the optimal velocity for the next cycle was interpolated at $\approx 11\,\text{m s}^{-1}$ in orange. Since only three points were actually measured, no statistical analysis can be performed here.

5.3.2 Zero Rate Vs. Air Quality

The cycles 211, 212 and 213 were done with minimal disturbance of the system and no significant drop in the zero count rate was observed during normal operation.

To further clarify the effect of contamination of the vacuum a few dedicated measurements were taken. The first was done by cleaning the mirrors and measuring the zero rate. After that the vacuum chamber was opened for $\approx 50\,\text{min}$ and then, without cleaning the mirror surfaces, measuring the zero rate again. The result showed a drop in the zero rate but here only from a non repeatable, non controlled opening.

To properly investigate the effect another set of measurements was performed where the chamber was vented but the lid of the vacuum chamber was not opened. To vent the chamber there is a valve which has a dust and oil filter on the inlet. Through this valve the chamber was vented and then pumped to vacuum again four times, where the zero rate was measured after each pumping cycle. Then for the fifth venting event the oil and particle filter was removed and one more venting and pumping cycle was performed. This can be seen in fig. 5.6, which shows a significant drop for the last cycle.

A χ^2 analysis for the null hypothesis of a constant rate can be exluded with 95% confidence. Removing the last point gives a P-value of 24% for the constancy of the rate and no variation can be inferred. Therefore the air coming in from the reactor leads to a contamination of the mirror surfaces. This provides a general feature of qBOUNCE: the mirror surfaces have to be cleaned when opening the chamber.

During normal operation where the experiment remains closed and in vacuum the vacuum is not contaminated. This has been observed in all closed chamber datasets since the removal of the borated plastic in 2019 described in the introduction to this chapter.
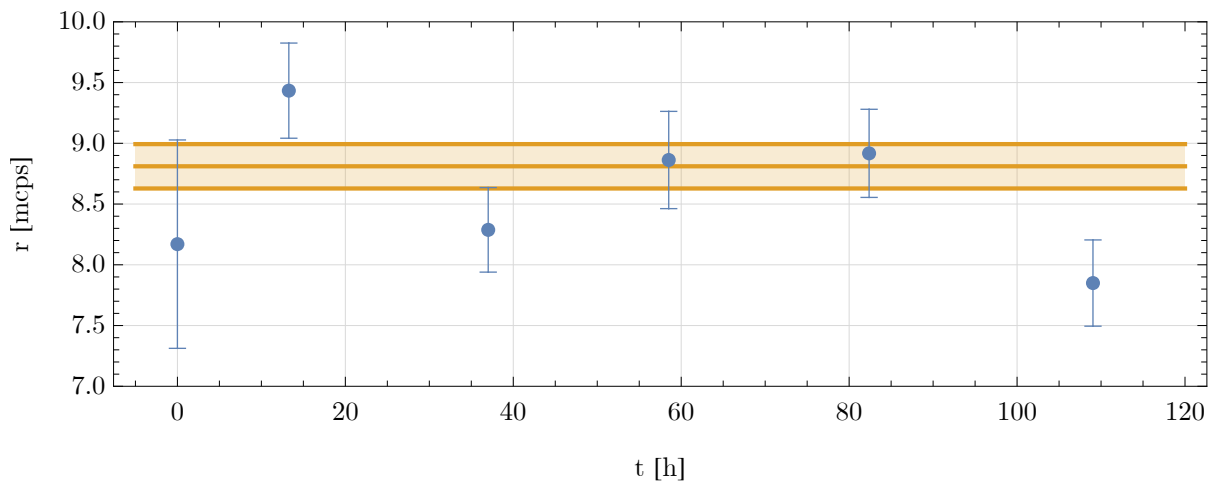
Figure 5.6: Measurement to determine the effect of opening the vacuum chamber. Rhe first measurement was after cleaning, the next four with vent and pump cycles in between with an oil filter in place, and the last was after a vent cycle without oil filter in place. All of these were taken in vacuum.
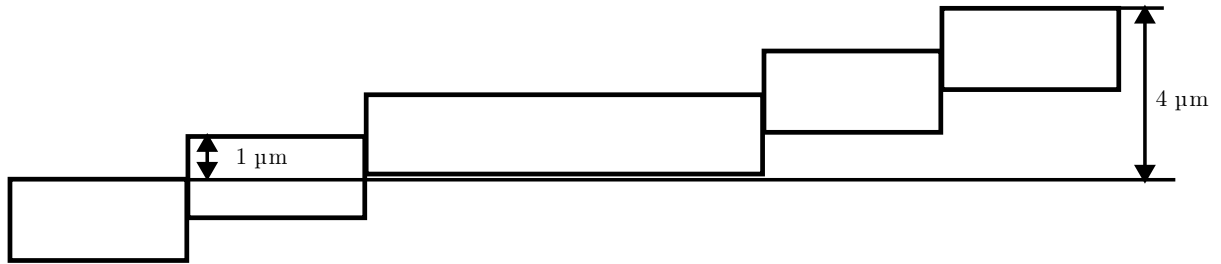
Figure 5.7: Four steps over the whole setup. Here into the neutron path. Another set with steps going the other way was also performed.
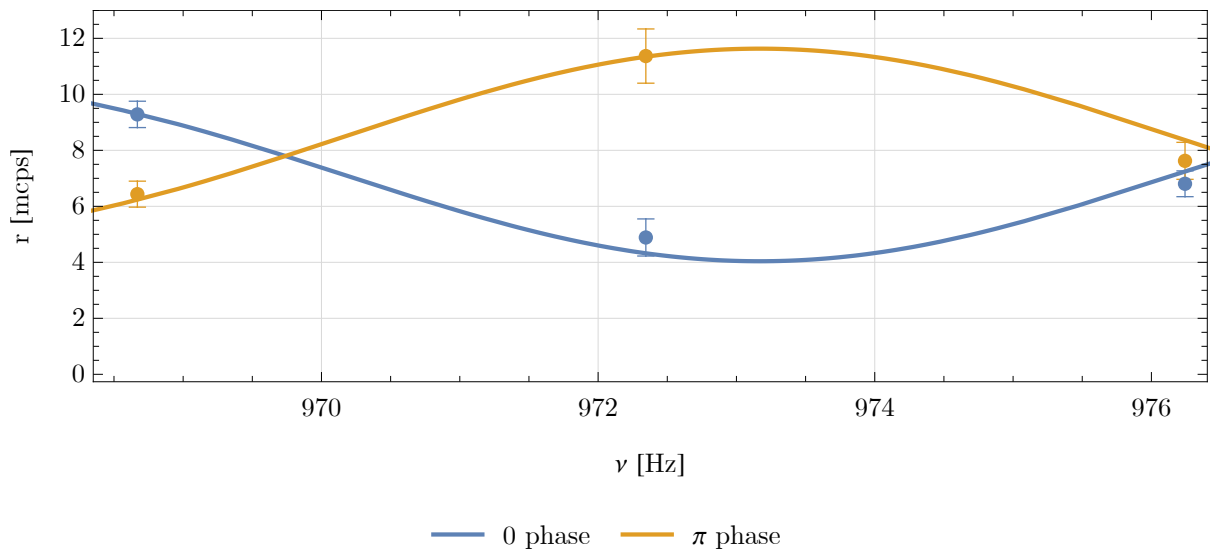

Figure 5.8: Transmission over frequency for induced $+1\,\mu m$ steps.

5.3.3 Injected steps

To determine if there is a dependency of the tranisiton frequency with respect to steps between the mirrors, a series of measurements with induced steps was performed. To this end an intentional step of $\pm\,1\,\mu m$ was induced and the transition frequencies were measured. This can be seen in fig. 5.7. As mentioned in 4.1.4 these were introduced at all mirror boundaries. The overall height difference between sec I and V was $4\,\mu m$. The data can be seen in fig. 5.8, 5.9, 5.10. This resulted in a significantly reduced rate for the $+1\,\mu m$ measurement. The results for the transition frequency can be seen in fig. 5.11 and the resulting parameters in tab. 5.2.

Table 5.2: Fitresult for a constant transition frequency ν_0. There is no significant variation of the transitionfrequency detected by these measurements.

ν_0 [Hz]	σ_{ν_0} [Hz]	P-Value
972.86	0.086	0.155

This shows a variation of the transition frequency of the step in the up direction, but a variation of this transition frequency was not significant. Further measurements of this type are necessary to eliminate a possible contribution of this effect. Furthermore the effect of alternating or more complicated
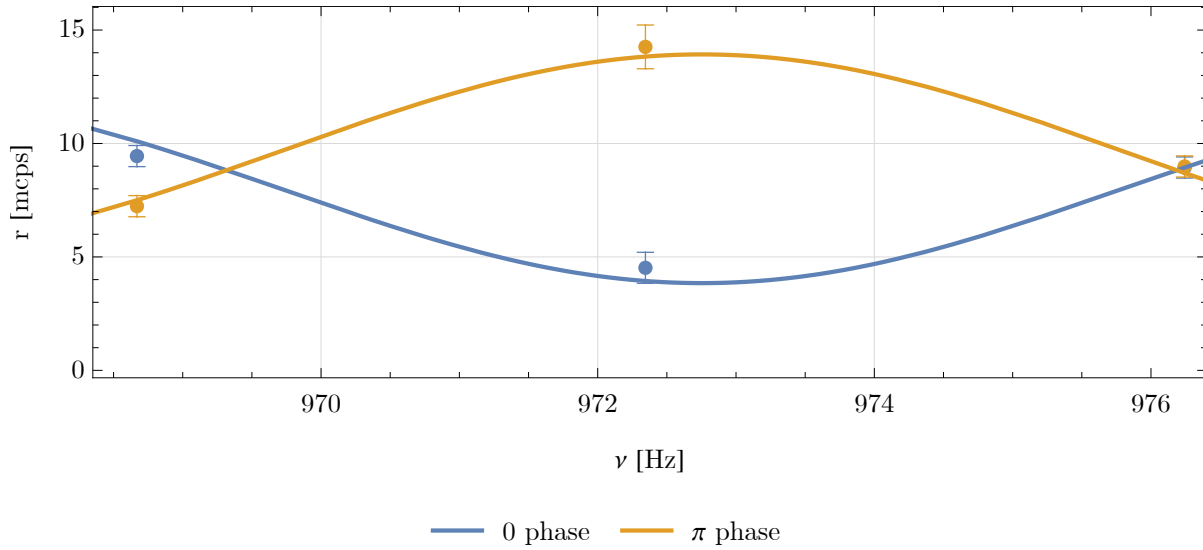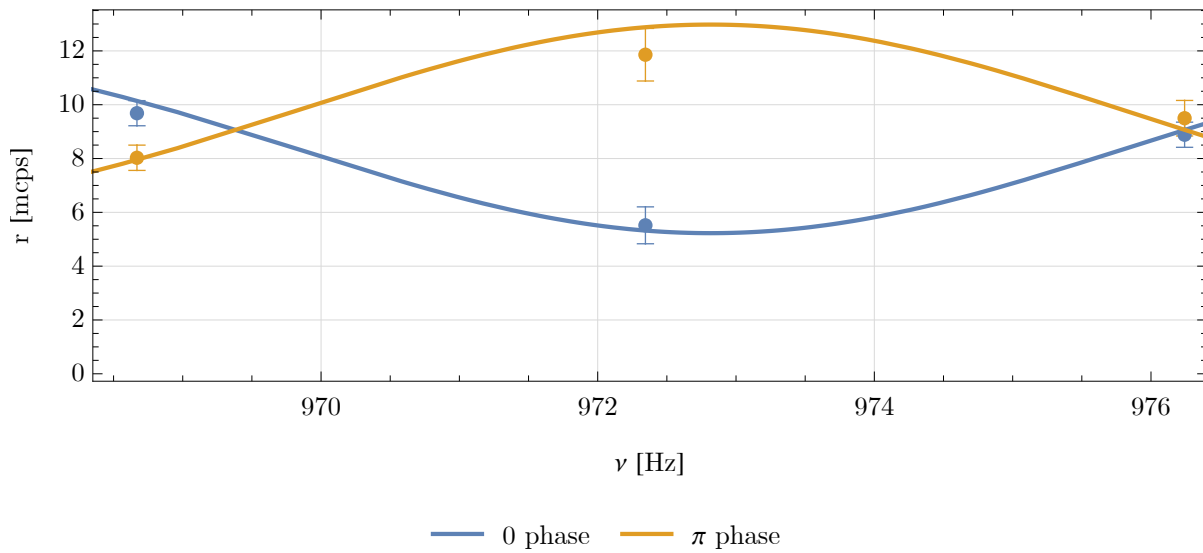
Figure 5.9: Transmission over frequency for no induced steps.

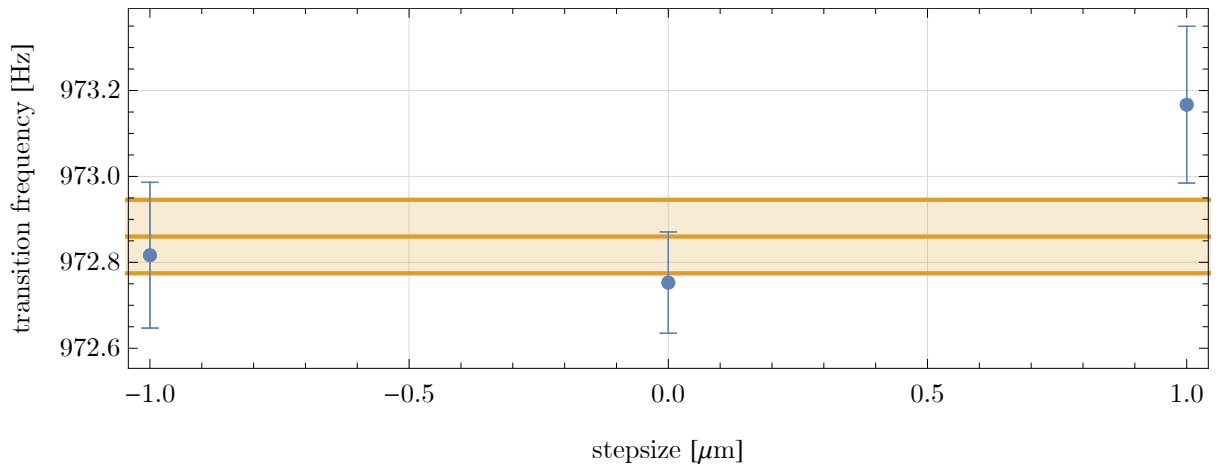Figure 5.10: Transmission over frequency for induced -1 μm steps.

Figure 5.11: Transition frequecy with induced steps between sections. The total change in height of the last section is therefore four times this stepsize.

steps along the mirror can be investigated.

5.4 Main measurements

The measurements presented here represent runs where the goal was to measure the transition frequency to the highest precision possible without modifications to the experiment. The main focus was the transition $|1\rangle \to |6\rangle$ and to provide a frequency panorama similar to [? ?]. Limiting to the six qBOUNCE points can further improve the sensitivity once the system is sufficiently well studied.

5.4.1 Dataset 1

The first high precision measurement of Ramsey fringes was performed in the cycle 212. The observed transitions were mainly $|1\rangle \to |6\rangle$ and $|2\rangle \to |7\rangle$. It was also attempted to observe the transition $|1\rangle \to |3\rangle$, which was not possible. From the results of chapter 5.3.1 the velocities of the neutrons was set to $v \in [4.5, 11]\mathrm{m\,s^{-1}}$ where the neutron measurement time is highest.

Initial amplitude sweep for $|1\rangle \to |3\rangle$

The transition should be located at $\nu \approx 462.925\,\mathrm{Hz}$ and $a\omega \approx 1.5\,\mathrm{mm\,s^{-1}}$ for a $\pi/2$-flip. To determine the optimal vibration amplitude $a\omega$ it is increased from 0. This is done because the precise value is dependent on the velocity spectrum and the state distribution. Mechanical stability is checked via the SIOS interferometer and the π-phase measurement. While performing the $a\omega$-sweep, the measurements for the $\phi = \pi$ measurements did not return to the zero rate, but also showed a clear frequency dependent decrease as shown in fig. 5.12.

There are multiple possible reasons for this. There is the possibility that the simple two state secular aproximation is not valid, such that either the Bloch-Siegert shift or multi state effects or an arbitrary combination of these two causes the drop of the π phase rate. The second possibility is the mechanical nature of the system. As shown in equation 2.33 the 0-phase measurement is $\propto \cos\left(\frac{a\omega_{II} + a\omega_{IV}}{2}\right)^2$, whereas the π phase measurement $\propto \cos\left(\frac{a\omega_{II} - a\omega_{IV}}{2}\right)^2$. If the difference of the system is not 0 because of a mechanical resonance of section IV at the transition the dip of the π measurement could be explained. This could be excluded by observing the measured oscillation strength using the interferometer. Also the reverse could be the case: there is a mechanical resonance of the interferometer mount that is sharp enough to couple to the oscillating mirrors. The calibration measurements when setting up the oscillations would then be incorrect. This happens with the internal interferometer, and has not been observed in test measurements using the external interferometer.

Because of the failed $a\omega$ sweep and the goal to get high precision data for the transition $|1\rangle \to |6\rangle$ the decision was taken to forego further measurements at this frequency and to focus on the other transition. This serves to highlight the importance of the $a\omega$-sweep as a self consistency check of the experiment.

$|1\rangle \to |6\rangle$

This transition is located at $\nu \approx 972.345\,\mathrm{Hz}$ with an expected $a\omega \approx 3.3\,\mathrm{mm\,s^{-1}}$. The $a\omega$ sweep can be seen in fig. 5.13.

Here the recovery in the π phase branch is present, and a deviation from the zero rate is not present. The minimum is located at $\approx 3\,\mathrm{mm}$ from the fit. To limit the mechanical stress on the system a oscillation velocity of $a\omega \approx 2.5\,\mathrm{mm\,s^{-1}}$ was chosen, the increase in contrast by going to $3\,\mathrm{mm\,s^{-1}}$ is lost in the statistical uncertainty. The frequency sweep at this oscillation strength can be seen in fig 5.14.

$|2\rangle \to |7\rangle$

This transition was addressed for a short time before changing the setup to the magnetic setup. The transition is at $\nu \approx 865.82\,\mathrm{Hz}$. As the experimental $a\omega$ the value from the $|1\rangle \to |6\rangle$ was chosen using the relation $a\omega \propto \nu$, resulting in $a\omega \approx 2.5\frac{865.82}{972.345} \approx 2.2\,\mathrm{mm\,s^{-1}}$, since there was not enough time for a proper sweep in this case. Only at the scaled a single test measurement at a lower $a\omega$ was taken to check wheter or not the 0 phase rate increases (and if the π phase would stay up). This can be seen in fig. **??**. In general this measurement also showed the expected behaviour and the ν sweep was performed, resulting in fig. **??**.
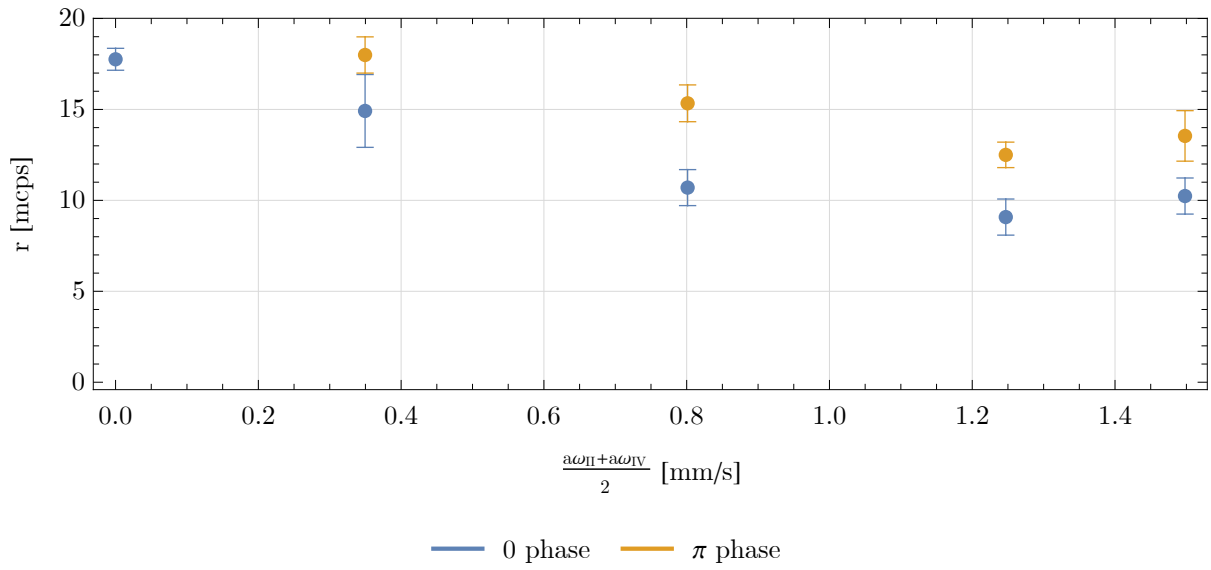
Figure 5.12: $a\omega$ sweep at $\nu = 472.925\,\text{Hz}$. The π phase measurements drop in rate with increasing $a\omega$. The expected beahaviour is that the π phase measurements stay at $r \approx 18\,\text{mcps}$.
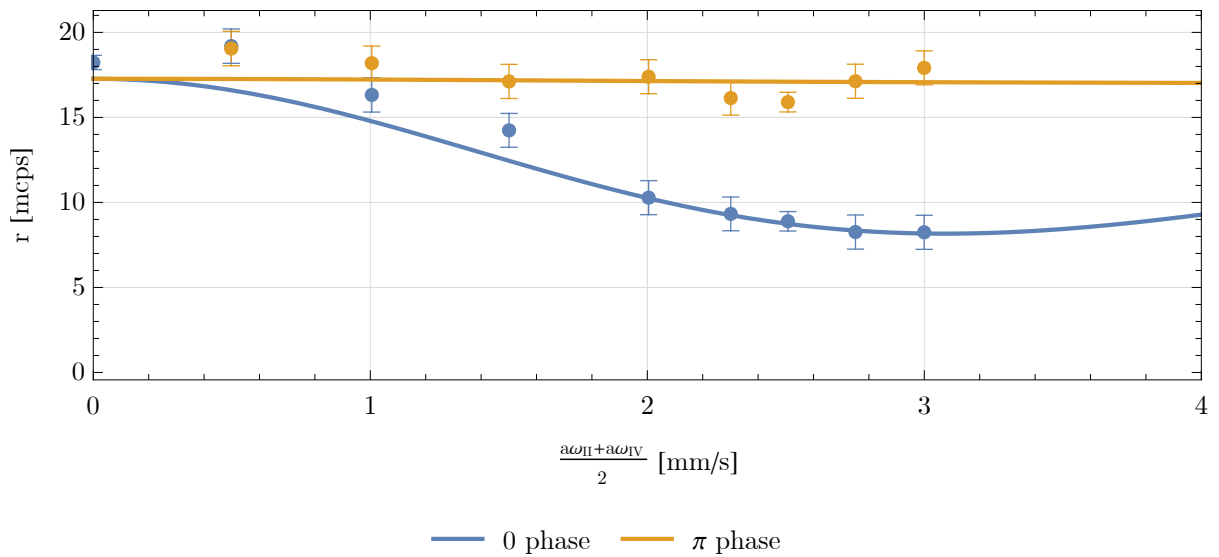

Figure 5.13: $a\omega$ sweep at $\nu = 972.345\,\text{Hz}$. The π phase measurements recover to the zero rate. This is consistent with the expectation.

Combined Analysis

Using these data to perform a global fit results in 5.17 with fit result in tab. 5.3. The fit has a $\chi^2 \approx 74.4$ with $n_{eff} = 73$. It is consistent with no third state present. A background of 15 % is present in the data. The most probable cause of this are neutrons entering the detector without going through the exitation regions. This is to be expected to a certain degree, since the neutron beam has an inherent divergence given by the beamguide geometry. Any neutron that falls off the mirror while propagating through the vacuum chamber can potentially reenter the detector. Care has been taken to reduce this as much as possible with shielding, but a complete elimination of this has not been achieved.
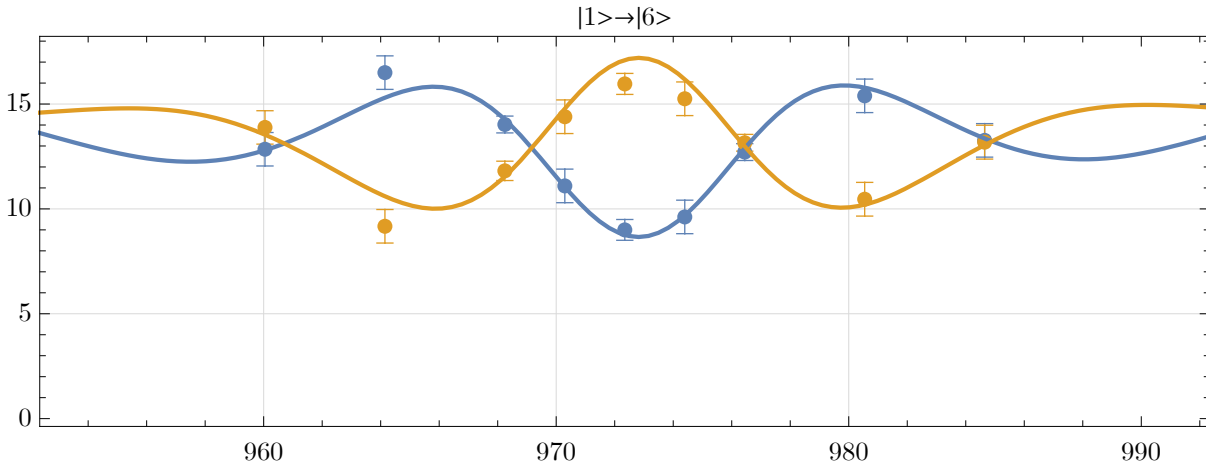
Figure 5.14: ν sweep at $a\omega = 2.5\,\mathrm{mm\,s^{-1}}$. The transition $|1\rangle \to |6\rangle$ is expected to be at $\nu = 972.345\,\mathrm{Hz}$.
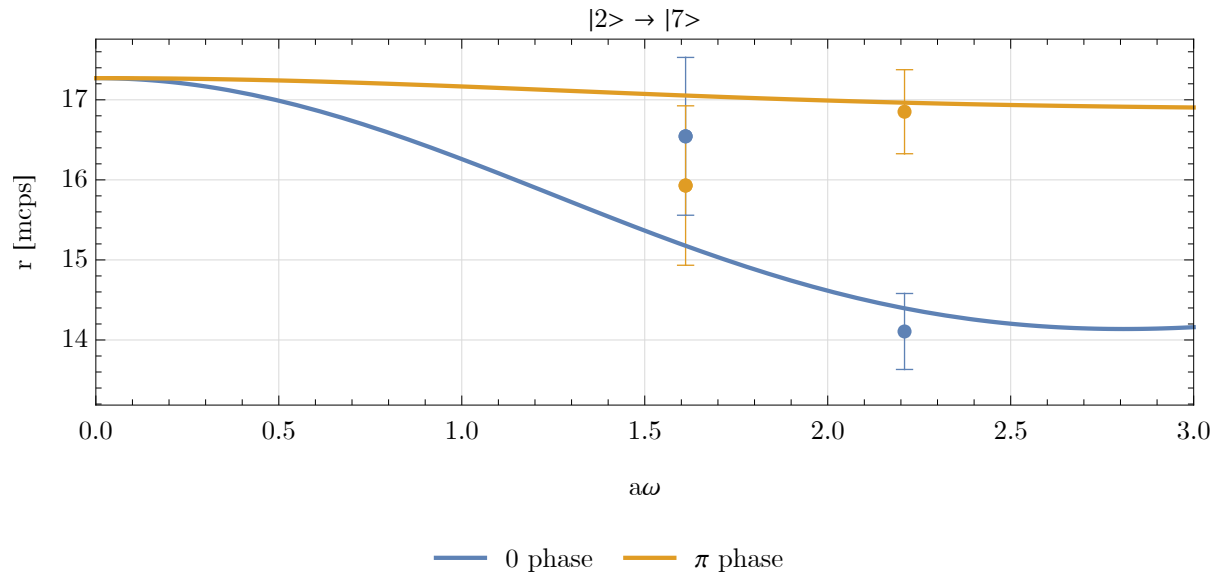

Figure 5.15: $a\omega$ sweep at $\nu = 865.82\,\mathrm{Hz}$. Measurement time did not allow higher statistics in the measurement point or a detailed sweep, so the theoretical value for $a\omega = 2.2\,\mathrm{mm\,s^{-1}}$ was used in the frequency sweep.

Fundamentally these data can be limited to varying degrees, for example only the points closest to the transition frequency of $|1\rangle \to |6\rangle$ could be used, or only $|2\rangle \to |7\rangle$, the velocity spectrum can be changed. All these have the effect of changing the resulting value of g less than the error in the combined fit.

Using g from 5.3 gives $\nu_{|1\rangle \to |6\rangle} = 972.819(117)\,\mathrm{Hz}$ and the whole data was a total measurement time of $t = 18.65\,\mathrm{d}$. This gives a sensitivity of $\sigma = 0.5\,\mathrm{Hz}/\sqrt{\mathrm{days}}$ for this measurement. This is significantly higher than expected from the measurements done in 5.3.1. One reason for this is that the sensitivity measurements used only the 6 optimal points of the qBOUNCE scheme but here many more datapoints at "less" advantageous positions were taken. This is of course only from the viewpoint of pure frequency determination: The additional points provide consistency for the theory model. Another reason is that the drop in the rate for the sensitivity measurements was $\Delta r_{\mathrm{sensitivity}} \approx 65\%$ whereas in this instance it was
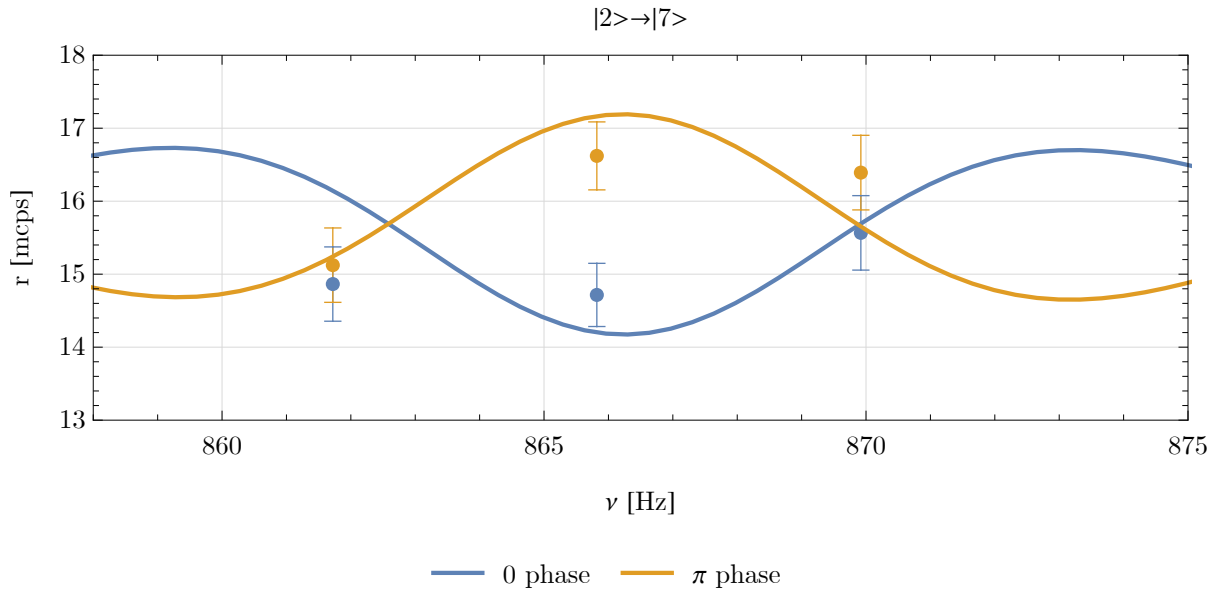
Figure 5.16: ν sweep at $a\omega = 2.2\,\mathrm{mm\,s^{-1}}$. The transition $|2\rangle \to |7\rangle$ is expected to be at $\nu = 865.82\,\mathrm{Hz}$.

Table 5.3: Fit results for the data of transitions $|1\rangle \to |6\rangle$ and $|2\rangle \to |7\rangle$. p1, p2 and p3 are the occupation numbers, pb a frequency independent background, r0 the rate without oscillations and g the value for the gravitational acceleration.

Parameter	Estimate	Error
p1	0.608	0.02
p2	0.216	0.027
p3	0.036	0.042
pb	0.14	0.
r0	17.271	0.165
g	9.812	0.002

only $\Delta r \approx 50\%$, which results in an additional increase of the sensitivity. Lastly the two measurements were taken in different reactor cycles with different reactor powers, where the setup was changed in between (to facilitate the "optimum" velocity) so the exact comparability of the two cycles is not given.

From the combination fit of $|1\rangle \to |6\rangle$ and $|2\rangle \to |7\rangle$ the relative precision comes out as $\sigma_g/g \approx 0.002/9.812 \approx 2 \cdot 10^{-4}$, the highest precision GRS measurement up to that point.

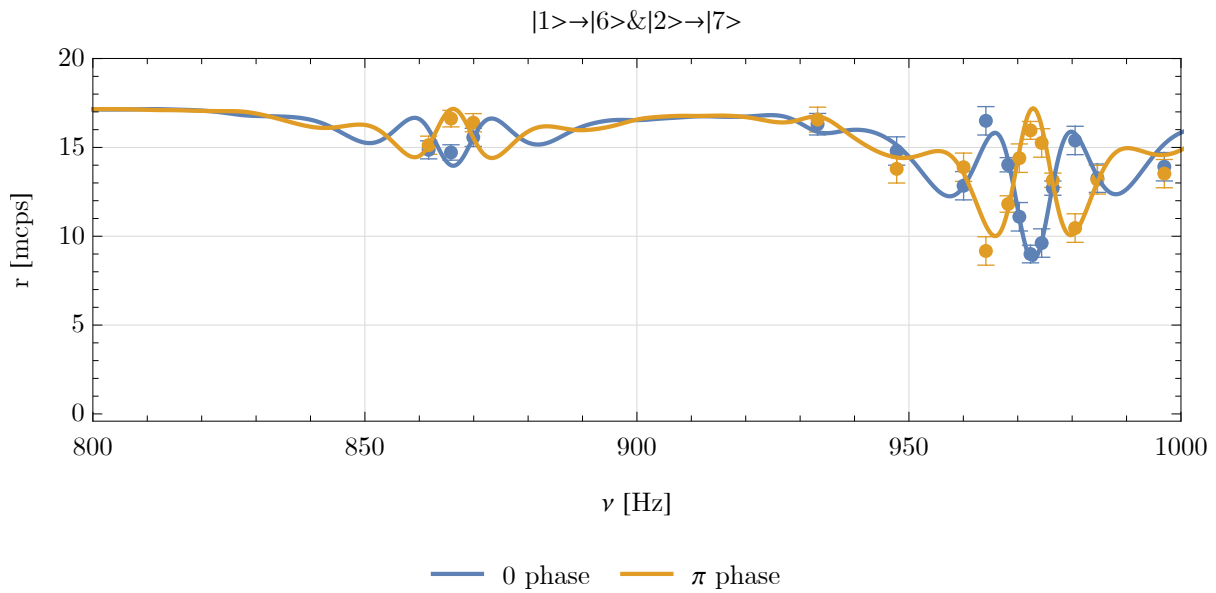Figure 5.17: Both frequency sweeps from $|1\rangle \rightarrow |6\rangle$ and $|2\rangle \rightarrow |7\rangle$ combined. $|1\rangle \rightarrow |6\rangle$ is found to be at $\nu_{|1\rangle \rightarrow |6\rangle} = 972.819(117)\,\text{Hz}$ and $|2\rangle \rightarrow |7\rangle$ at $\nu_{|2\rangle \rightarrow |7\rangle} = 866.23(12)\,\text{Hz}$ when calculating the transition frequencies from g in 5.3.

5.4.2 Magnetic Field

At the end of the cycle the setup was changed in order to perform spin dependent measurements. This made it necessary to change the detector. As shown in appendix C the velocity of the neutrons had to be limited to $v \leq 7.5\,\mathrm{m\,s^{-1}}$ since the polarisation efficiency of the detector drops off. A background magnetic field of $B_0 \approx 120\,\mu\mathrm{T}$ was induced parallel to the detector polarisation. This was then switched from parallel to antiparallel with respect to gravity. The first measurement was performed without background field and without active polarisation of the detector. Then the fields were put anti parallel to g then parallel to g and then anti parallel again. The resulting frequency sweeps are shown in 5.18 with resulting transition frequencies shown in fig. 5.19. Using as a hypothesis a constant transition frequency gives as a fit result $\nu_0 = 972.4(4)\,\mathrm{Hz}$ with a P-value of 74%. Calculating the value of g for this transition results in $g = 9.807(6)\,\mathrm{m/s^2}$. This is consistent with both the classically measured value, and the value obtained from the unpolarized measurement. There is no significant shift of the transition frequency observable when switching the direction of the neutron spin relative to gravity at this level of precision. The relative precision for the constancy of g is given by $\delta g/g = \frac{3}{2}\delta\nu/\nu \approx 6.3 \cdot 10^{-4}$.

The statistics provided by these data is not as strong as for the other Ramsey measurements. Due to time constraints the measurements could not be taken for enough time to reach a higher precision with the low count rates. A dedicated beamtime for these measurements can provide a significant improvement for these results.
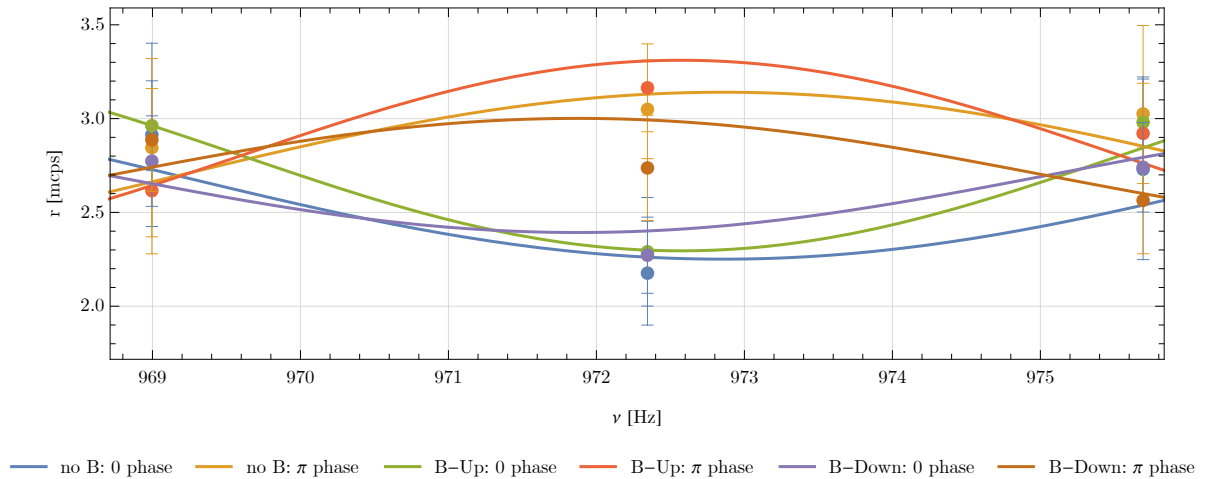

Figure 5.18: GRS measurements with the different B field configurations. The observed transition frequencies are all statistically compatible with a constant transition frequency.

5.4.3 Dataset 2

During the cycle 213 the goal was to concentrate on spin independent measurements and map the space around transition $|1\rangle \to |6\rangle$. This was done for the whole cycle where the actually measured transitions were $|1\rangle \to |6\rangle$ and $|2\rangle \to |8\rangle$. The transition $|2\rangle \to |8\rangle$ was observed for the first time and a clear asymmetry in the transmission curves could be seen. The details of this complete system show the necessity for a multi state analysis, which can only be roughly approximated by a two state approach.

The decision was made to increase the velocity again to $v \in [4.5; 14]\mathrm{m\,s^{-1}}$, since in the previous cycle the anticipated increase of sensitivity was not observed.

As can be seen in 2.2, the transition $|2\rangle \to |8\rangle$ and $|3\rangle \to |9\rangle$ are located approximately $30\,\mathrm{Hz}$ above and below the transition $|1\rangle \to |6\rangle$. It was therefore decided to investigate this frequency range to get high precision data for these transitions. Furthermore it is possible to see a direct contribution of state $|3\rangle$. If transition $|3\rangle \to |9\rangle$ is present this means that the initial state preparation at a cutoff velocity of $14\,\mathrm{m\,s^{-1}}$ still permitts a significant amount of the third state through the system.
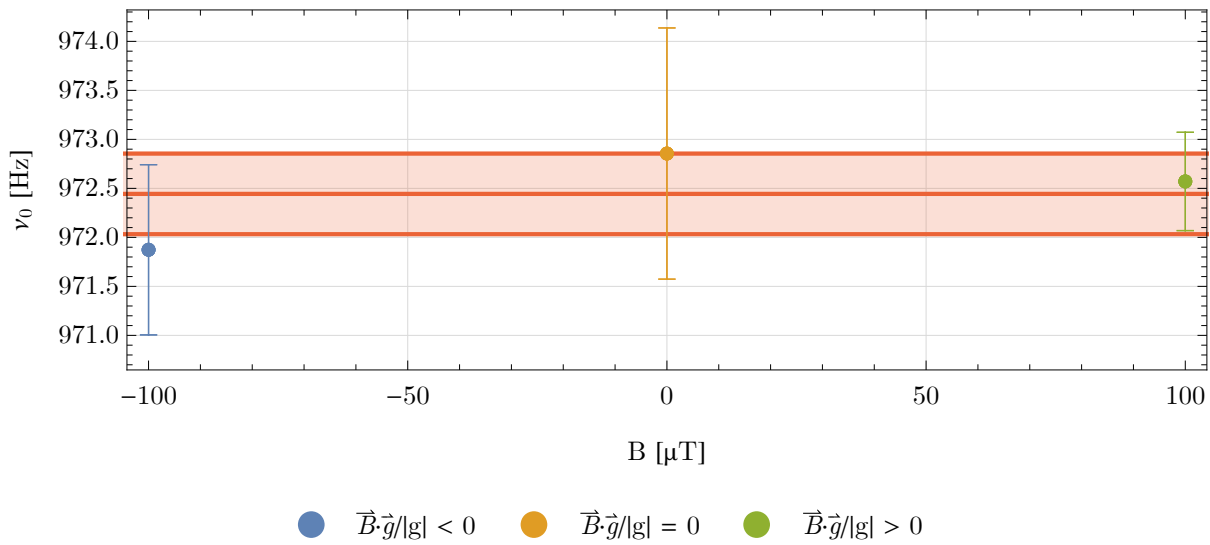
Figure 5.19: Resulting transition frequencies for different B field configurations

In order to adress the offset transitions a modification of $a\omega$ would be necessary. Because $a\omega \propto \nu$

$$
\frac{a\omega_{|2\rangle \to |8\rangle}}{a\omega_{|1\rangle \to |6\rangle}} \approx 1.035 \ ,
$$
$$
\frac{a\omega_{|3\rangle \to |9\rangle}}{a\omega_{|1\rangle \to |6\rangle}} \approx 0.960 \ ,
$$

(5.2)

compared to the ideal $|1\rangle \to |6\rangle$ excitation. Since the ideal excitation with $a\omega = a\omega_0 + \epsilon$ is $\sim \sin{(\epsilon)}^2 \approx \epsilon^2$ the adjustment of the vibration velocity is not strictly necessary to show the existance of the transition, furthermore measuring $a\omega$ to this precision is not possible. The $a\omega$ sweep at $972.345\,\mathrm{Hz}$ is shown in fig. 5.20, with the final used oscillation strength being $a\omega = 3.6\,\mathrm{mm\,s^{-1}}$ which agrees very well with the theoretical value of $a\omega \approx 3.68\,\mathrm{mm\,s^{-1}}$. The frequency sweep at this oscillation strength can be seen in fig. 5.21, with fit results shown in table 5.4.

The whole panorama shows a few interesting features which can not be explained by the two state approximation. Using only a two state system the asymmetry caused by the $|2\rangle \to |8\rangle$ transition cannot be explained. Therefore this system is inherently a multi state system. The $|2\rangle \to |8\rangle$ transition is highly dependent on the state preparation: as can be seen in the fit results, the system is almost entirely comprised of states $|1\rangle$ and $|2\rangle$. The transition $|3\rangle \to |9\rangle$ is not present in this data. This raises questions with the results from previous cycles. The state preparation was not changed (the absorber mirror system used in sections I and V), only the velocity interval was varied. In reality these measurements are not directly comparable since the vacuum chamber was opened to change the velocities of the neutrons. In the future an automated aperture system should be implemented to be able to change the velocity interval without opening the vacuum chamber. This would provide multiple significant improvements. First the velocity spectrum could be mapped using various methods without disturbing the vacuum. Second the measured precision could be optimised each reactor cycle with respect to the velocities, as was tried in 5.3.1, with much less induced uncertainties.

Furthermore $|2\rangle \to |8\rangle$ has a large influence on the general shape of the interference pattern, the side fringes of the $|1\rangle \to |6\rangle$ transition are asymmetric around the resonance frequency. This shows clearly the existence of the transition $|2\rangle \to |8\rangle$ for the first time. The overall reached precision $\sigma_g/g \approx 0.001/9.814 \approx 1 \cdot 10^{-4}$ pushes the achieved precision for a single measurement campaign again further to a new low.
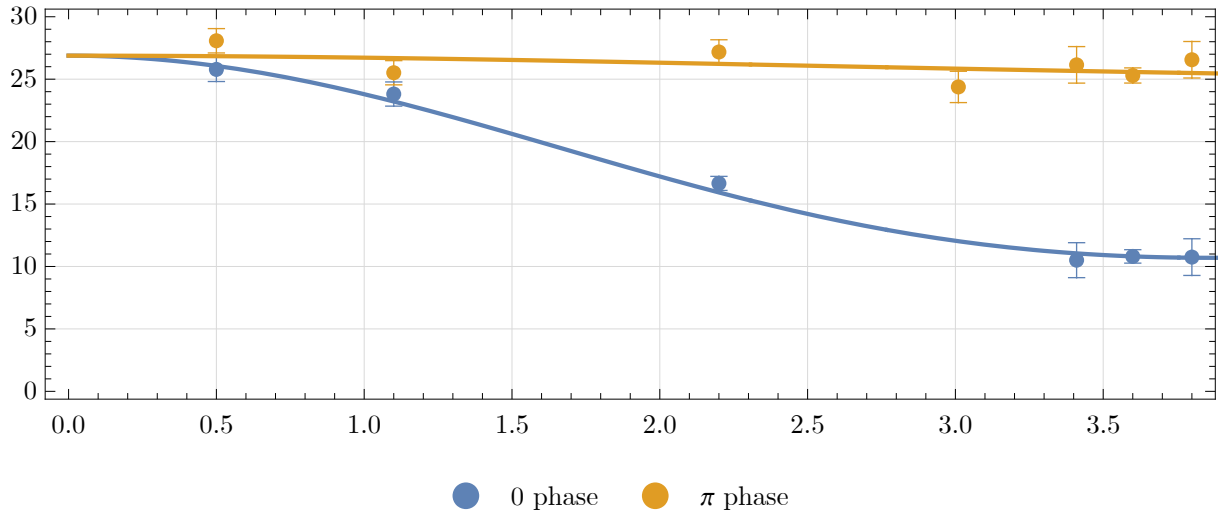
Figure 5.20: $a\omega$ sweep at $\nu = 972.345\,\text{Hz}$. The recovery for the π phase is present and the contrast is slightly larger than 0.5.
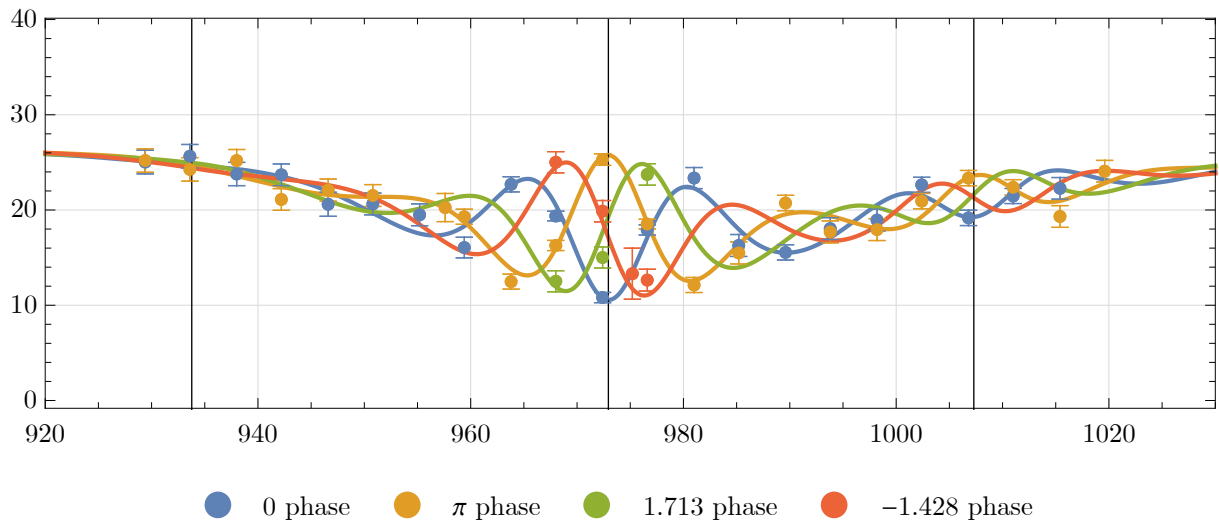
Figure 5.21: Frequency sweep with transitions $|3\rangle \to |9\rangle$, $|1\rangle \to |6\rangle$ and $|2\rangle \to |8\rangle$ indicated with black lines from left to right.

Table 5.4: Fit results for the data of transitions $|1\rangle \to |6\rangle$, $|2\rangle \to |8\rangle$ and $|3\rangle \to |9\rangle$. p1, p2 and p3 are the occupation numbers, pb a frequency independent background, r0 the rate without oscillations and g the value for the gravitational acceleration and f the scaling in the fit function to $a\omega$.

Parameter	Estimate	Error
p1	0.715	0.018
p2	0.254	0.027
p3	0.003	0.035
pb	0.027	0.
r0	26.883	0.252
gg	9.814	0.001
f	0.862	0.033

5.5 Results

Combining all measurements of g derived from the determination of the transition frequency into one gives fig. 5.22 with the best estimate

$$g_{qBounce} = 9.812\,53(69)\,\text{m/s}^2 \tag{5.3}$$

giving

$$\frac{\sigma_{g_{qBounce}}}{g_{qBounce}} \approx \frac{0.00069}{9.81253} \approx 7 \cdot 10^{-5} \tag{5.4}$$

as the relative precision. This is the most accurate measurement of the local acceleration due to gravity using a system whose quantum energy eigenstates are solely determined by gravity. This value $g_{qBounce}$ is what is obtained directly from the experiment. The implications of this value with consideration of the systematic effects will be discussed in the following chapter 6.

Using a spin dependent detector a potential shift of the transition frequency with the alignment of the neutron spin relative to gravity has been investigated. At the relative precision of

$$\frac{\delta g_{\text{spin}}}{g_{\text{spin}}} = 6.3 \cdot 10^{-4} \, , \tag{5.5}$$

no significant dependency of the transition frequency on the direction of spin could be observed.
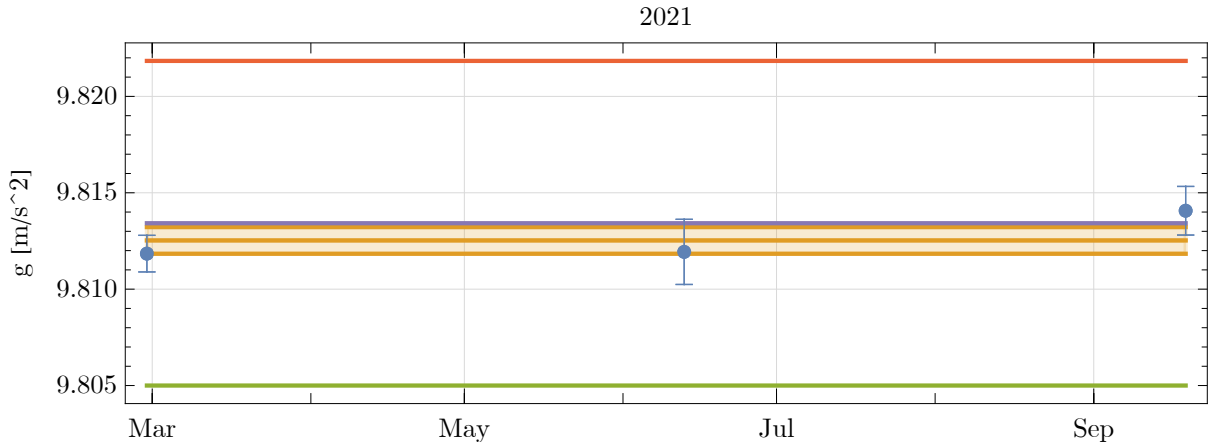

Figure 5.22: Combination of all measured values for g in the year 2021. Indicated in orange the combined fit for all three values giving $g_{qBounce}$. Green shows the classically measured value, red the value when adding back the effect of the rotating Earth and finally violet shows the exact middle position between the rotating and non rotating Earth.

Chapter 6

Conclusion & Outlook

Over the last few years qBOUNCE was able to commission and optimise the spectrometer implementing Ramseys method of separated oscillating fields. During this thesis the experiment was improved to a point where stable measurements could be taken. As described in section 3 a lot of experimental details were investigated. The mechanical stability of the mirror system was investigated 3.3.1 with clear indication of the mechanical behaviour of the whole system. Furthermore the alignment system 3.3.7 was improved to perform repeatable and stable experiments. These were all done before the summer of 2020.

One of the main improvements was the introduction of the Rb-Clock reference to eliminate all experimental uncertainty in both the phase and the frequency measurement 3.3.8. Now the generation of the oscillation frequency agrees with the measured values from a decoupled laser interferometer within the measurement precision. The datasets used for the determination of $g_{qBounce}$ all used the Rb-Clock as a timebase and the frequency determination for the fits comes from the measurements of the interferometer. A final result for the value of g can be obtained by subtracting the systematic offset: qBOUNCE measures the value of $g_{qBounce} = g_{measured} = g_{true} + \delta g_{sys.}$ as was described in chapter 4 in eq. (4.55). To obtain the final value for g_{true} the systematic shift $\delta g_{sys.}$ is subtracted via

$$g_{qBounce} \pm \sigma g_{qBounce} - \delta g_{sys.} \pm \sigma g_{sys.} = 9.81253 \pm 6.9 \cdot 10^{-4} - 6.1 \cdot 10^{-4} \pm 6.5 \cdot 10^{-4} \mathrm{m/s^2} \ . \tag{6.1}$$

This is to be compared to classical value determined by a falling corner cube measurement 5.2.3 which resulted in

$$g_{cornercube} = 9.804\,924\,69(10)\,\mathrm{m/s^2} ;\, . \tag{6.2}$$

Comparing this with 6.1 gives

$$\frac{(g_{qBounce} - \delta g_{sys.}) - g_{cornercube}}{\sqrt{\sigma g_{qBounce}^2 + \sigma g_{sys.}^2}} = 7.43 \ , \tag{6.3}$$

as a deviation of 7.43σ from the classical expectation. This is statistically unlikely to be a coincidence. A detailed discussion and analysis of possible systematic shifts was done in 4.

The transition $|1\rangle \to |6\rangle$ has been measured with a spin polarized detector in a $120\,\mu$T magnetic field. Checking for an observable shift in the transition frequency by observing the two spin polarisations did not produce a significant shift. This measurement was done at a relative precision of $\delta g/g \approx 6.3 \cdot 10^{-4}$.

The in depth analysis of systematic shifts during the course of this thesis identified the largest systematic shift coming from a possible phase offset. This phase offset is monitored by a laser interferometer that is decoupled from the mechanical oscillations of the neutron mirrors. The phase between the two oscillating mirrors is created by a frequency generator and then directly applied to the mirrors. The agreement is on the order of 1° which is the error considered in 4.1. A phase shift leads to a direct shift of the transition frequency as was described in 4.1.2. This shift can be eliminated by an improved monitoring of the mechanical system. With the current monitoring the phase varies from positive to negative during measurements.

The second biggest effect is a quantum effect arising from the bound states of the neutron. There are in principle infinitely many, a single excitation frequency can always induce higher order transitions.

This introduces the so called spectator-state shift where there is an additional component from the excitation with a sinusoidal mirror movement called the Bloch-Siegert shift. This is described in 4.1.5 and has to be evaluated numerically. In a multi transition system these shifts have complicated state occupation dependent magnitudes, so they have to be investigated for every transition. This shift can not be eliminated it has to be taken into account for every frequency range addressed. For higher precision measurements these effects need to be taken into account and a framework for dealing with these calculations efficiently should be implemented.

The third largest effect is from the Coriolis force acting on the moving neutron. As shown in 4.2.3 in detail the classical corrections to the acceleration in a rotating frame are also valid for the quantum mechanical system. The centrifugal force for a resting particle is included in the measurement of 6.2, only the proper motion of the neutron in the lab frame is observed. This shift can be calculated precisely by determining the neutron velocity and can therefore also be changed with an adjustment of the velocity interval. This opens up another degree of freedom in the experiment once the measurement precision is increased to a level where this is observable. As shown in 3.3.4 the neutron velocities range approximately from 4 to 14 $\mathrm{m\,s^{-1}}$ allowing for a relatively large adjustment of the Coriolis force of a factor of at least two if necessary.

Further effects are discussed in 4 but are smaller than these three. In general the current systematic effects are too small to explain the observed offset from the classical value. One possible explanation is an unobserved phase shift not visible in the interferometer and function generator by coincidence. This can be checked in the future by observing different transition, as far apart in frequency as possible. A phase shift would result in a constant shift of the transition frequency, which is not a constant shift in g. Since precision data was only taken around $|1\rangle \to |6\rangle$ no conclusive analysis for this can be performed without additional data. Repeating a high precision measurement of $|1\rangle \to |3\rangle$ is a plausible candidate, it was measured before using the Rabi setup and is $500\,\mathrm{Hz}$ separated from $|1\rangle \to |6\rangle$. Adding a new independent way of measuring the phases of the mirror surfaces can also improve the confidence in the accuracy of the measurement. Another line of investigation should be the effect of geometric adjustments of the mirror surfaces. These have been performed under time constraints and should be repeated more accurately to exclude large contributions to the system. One more aspect has been neglected completely so far: neutrons are spin $\frac{1}{2}$ particles. The eigenstates of Dirac particles on a gravitating rotating sphere with oscillating mirrors has not been investigated in detail, especially the implications considering the Bloch-Siegert-Spectator-State shift. The possibility of a large modification to the spectator state shift in this system is quite unlikely but not zero. The geometric effects associated with spin $\frac{1}{2}$ on a rotating sphere need to be fully included. Proper treatment of a quantised theory with boundary conditions for this situation was not feasible here, a dedicated effort should be made to investigate this further. Further possibilities of large shifts are unknown to me at the current time. Except if in the first line of (4.49) $\frac{m_i}{m_g} = \frac{1}{2}$.

In the coming reactor cycles further measurements within qBOUNCE will undoubtedly improve the understanding of the mechanical system in combination with the complicated many state quantum system. Building a catalogue of high precision transition frequency data can help shed a light on unknown unknowns. The fundamental explanation for the shift in the measured g within qBOUNCE is not certain at this time, but will be obvious once found.

Appendix A

Expectation values from Airy functions

In this appendix I will calculate various identities and transition matrix elements by first deriving identities of Airy functions mainly following [23, 57].

Suppose there are two functions ψ and χ both satisfying a shifted Airy function for different E and E'

$$\partial_z^2 \psi = (z - E)\,\psi\,, \tag{A.1}$$

$$\partial_z^2 \chi = (z - E')\,\chi\,, \tag{A.2}$$

where the z dependence of both functions is implicit. These are Airy differential equations equivalent to solutions of the first line in eq. (2.8). It can now be seen that

$$
\begin{aligned}
\chi\partial_z^2\psi =& \partial_z\left(\chi\partial_z\psi\right) - (\partial_z\chi)\left(\partial_z\psi\right) = \partial_z\left(\chi\partial_z\psi - (\partial_z\chi)\,\psi\right) + \left(\partial_z^2\chi\right)\psi = \\
& \partial_z\left(\chi\partial_z\psi - (\partial_z\chi)\,\psi\right) + (z - E')\,\chi\psi = (z - E)\,\chi\psi\,, \\
\Rightarrow \chi\psi =& \frac{\partial_z\left(\chi\partial_z\psi - (\partial_z\chi)\,\psi\right)}{E' - E}\,.
\end{aligned}
\tag{A.3}
$$

This equation can be used to evaluate arbitrary overlap integrals of Airy functions. Furthermore by taking the derivative of (A.1) one arrives at

$$\partial_z^3\psi = (z - E)\,\partial_z\psi + \psi\,, \tag{A.4}$$

$$
\begin{aligned}
\chi\partial_z^3\psi =& \partial_z\left(\chi\partial_z^2\psi\right) - (\partial_z\chi)(\partial_z^2\psi) = \partial_z\left(\chi\partial_z^2\psi - (\partial_z\chi)(\partial_z\psi)\right) + (\partial_z^2\chi)(\partial_z\psi) = \\
& \partial_z\left((z - E)\chi\psi - (\partial_z\chi)(\partial_z\psi)\right) + (z - E')\chi\partial_z\psi = (z - E)\chi\partial_z\psi + \chi\psi
\end{aligned}
\tag{A.5}
$$

$$\Rightarrow \chi\partial_z\psi = \frac{1}{E' - E}\partial_z\left((z - E)\chi\psi - (\partial_z\chi)(\partial_z\psi) - \frac{1}{E' - E}\left(\chi\partial_z\psi - (\partial_z\chi)\,\psi\right)\right) \tag{A.6}$$

where in the last line equation (A.3) was inserted. Now it will be useful to also consider the special case $\chi = \psi$ of equation (A.5)

$$\psi^2 = \partial_z\left((z - E)\psi^2 - (\partial_z\psi)^2\right)\,. \tag{A.7}$$

These identities follow from the Airy equation itself. A generalisation of this can be done by following the same steps for

$$\partial_z^2\psi = (U(z) - E)\,\psi\,, \tag{A.8}$$

$$\partial_z^2\chi = (U(z) - E')\,\chi\,, \tag{A.9}$$

where U(z) is now an arbitrary z dependent potential. This results in

$$\Rightarrow \chi(\partial_z\psi) = \frac{1}{E' - E}\partial_z\left((U(z) - E)\chi\psi - (\partial_z\chi)(\partial_z\psi)\right) - (\partial_z U(z))\chi\psi \tag{A.10}$$

Now considering the time independent Schrödinger equation for the neutron on top of a mirror. It has been argued in chapter 2.8 that the Schrödinger equation can be written as

$$\partial_{z'}^2 \psi(z') = (z' - E')\,\psi(z') \tag{A.11}$$

where $z = z_0 z'$ and $E = E_0 E'$. The solutions to this equation are the shifted Airy functions $\mathrm{Ai}(z' - E')$ and $\mathrm{Bi}(z' - E')$. The general solution to the Schrödinger equation is then given by

$$\psi(z') = \frac{1}{N}\left(a\mathrm{Ai}(z' - E') + b\mathrm{Bi}(z' - E')\right) \tag{A.12}$$

For $z \to \infty$ Ai converges and Bi diverges. So for a physical neutron on top of a mirror $b = 0$. If it is assumed that the neutron does not enter the mirror $\psi(0)\,\hat{=}\,\mathrm{Ai}(-E') = 0$ so the $-E'$ coincide with the zeroes of the Airy function, where the n-th zero is called $\mathrm{AiZ}(n)$ in this thesis. From this the n-th energy eigenstate of the neutron can be written as

$$\psi_n(z') = \frac{1}{N_n}\mathrm{Ai}(z' + \mathrm{AiZ}(n)) \tag{A.13}$$

where the normalisation constant N_n depends on the quantum number n. It is determined by the requirement

$$\int_0^\infty |\psi_n(z)|^2 \mathrm{d}z = 1\,\hat{=} $$
$$\frac{z_0}{|N_n|^2}\int_0^\infty \mathrm{Ai}(z' + \mathrm{AiZ}(n))^2 \mathrm{d}z' \tag{A.14}$$

since the Airy functions are real. Utilising equation (A.7) with $E = -\mathrm{AiZ}(n)$ for the square of an arbitrary shifted Airy function this can be evaluated to

$$1 = \frac{z_0}{|N_n|^2}\left.\left((z' + \mathrm{AiZ}(n))\,\mathrm{Ai}\,(z' + \mathrm{AiZ}(n))^2 - \mathrm{Ai}'\,(z' + \mathrm{AiZ}(n))^2\right)\right|_0^\infty . \tag{A.15}$$

where $\mathrm{Ai}'(z) = \partial_z \mathrm{Ai}(z)$. Since $\mathrm{Ai}(\infty) = \mathrm{Ai}'(\infty) = 0$ most terms drop out and the remaining term results in

$$|N_n|^2 = z_0 \mathrm{Ai}'\,(\mathrm{AiZ}(n))^2 ,$$
$$\to N_n = \sqrt{z_0}\mathrm{Ai}'(\mathrm{AiZ}(n)) , \tag{A.16}$$

such that the fully normalised wavefuntion is given by

$$\psi_n(z') = \frac{1}{\sqrt{z_0}}\frac{\mathrm{Ai}(z' + \mathrm{AiZ}(n))}{\mathrm{Ai}'(\mathrm{AiZ}(n))} . \tag{A.17}$$

This is one choice for the normalisation constant but it could, in general, be multiplied by an arbitrary $e^{i\phi}$ without changing the physics content. This choice is the most "convenient" as no additional signs or phases appear in the following formulas.

Now the transition matrix elements V_{mn} quoted in chapter 2.3 can be easily calculated. They are given by

$$V_{mn} = \int_0^\infty \psi_m(z)\partial_z\psi_n(z)\mathrm{d}z = \int_0^\infty \psi_m(z')\partial_{z'}\psi_n(z')\mathrm{d}z' . \tag{A.18}$$

Using equation (A.10) with $E' = -\mathrm{AiZ}(m)$ and $E = -\mathrm{AiZ}(n)$ and vanishing wavefunctions at the boundaries leads to

$$V_{mn} = \frac{\left(\mathrm{Ai}'\,(\mathrm{AiZ}(m))\,\mathrm{Ai}'\,(\mathrm{AiZ}(n))\right)}{z_0\mathrm{Ai}'\,(\mathrm{AiZ}(m))\,\mathrm{Ai}'\,(\mathrm{AiZ}(n))\,(\mathrm{AiZ}(n) - \mathrm{AiZ}(m))} = \frac{1}{z_0\,(\mathrm{AiZ}(n) - \mathrm{AiZ}(m))}$$
$$= \frac{m_g g}{E_m - E_n} . \tag{A.19}$$

In the literature there are sometimes different sign conventions used, resulting from a different choice of sign in the normalisation constant of the normalized eigenstates (A.17).

Another useful relation is the overlap integral between two shifted wave functions, where the wave functions and the derivatives vanish at infinity. Utilising equation (A.3) and integrating from s/z_0 to infinity results in

$$\int_{s/z_0}^\infty \chi(z)\psi(z)\mathrm{d}z = \frac{z_0}{N_\chi N_\psi\,(E'-E)}\left(\mathrm{Ai}'\left(\frac{s}{z_0}-E'\right)\mathrm{Ai}\left(\frac{s}{z_0}-E\right)-\mathrm{Ai}\left(\frac{s}{z_0}-E'\right)\mathrm{Ai}'\left(\frac{s}{z_0}-E\right)\right).$$
(A.20)

where s is the height in SI units therefore has to be made dimensionless when using the characteristic quantities to express the results. This is valid for all wave functions that vanish at infinity sufficiently fast. Now there are two physically distinct situations. suppose that the state χ is the initial state of the neutron. It then encounters a mirror shifted in height.

$$\chi_m(z') = \frac{\mathrm{Ai}\left(z+\mathrm{AiZ}(m)\right)}{z_0\mathrm{Ai}'(\mathrm{AiZ}(m))}\Theta(z)\,,$$

$$\psi_n(z') = \frac{\mathrm{Ai}(z-s+\mathrm{AiZ}(n))}{z_0\mathrm{Ai}'(\mathrm{AiZ}(n))}\Theta(z-s)\,.$$
(A.21)

First we consider the case where the second mirror is lower than the first one. In this case $s < 0$ and it follows that $E_n = s/z_0 - \mathrm{AiZ}(n)$, $N_\psi = \sqrt{z_0}\mathrm{Ai}'(\mathrm{AiZ}(n))$, $E'_m = -\mathrm{AiZ}(m)$ and finally $N_\chi = \sqrt{z_0}\mathrm{Ai}'(\mathrm{AiZ}(m))$. The overlap integral is evaluated from 0 to infinity

$$\int_0^\infty \chi_m(z)\psi_n(z)\mathrm{d}z = \frac{\mathrm{Ai}\left(\mathrm{AiZ}(n)-\frac{s}{z_0}\right)}{\mathrm{Ai}'(\mathrm{AiZ}(n))(\mathrm{AiZ}(n)-\mathrm{AiZ}(m)-s/z_0)}\,.$$
(A.22)

For the case that $s > 0$ the lower bound of the integral becomes s and

$$\int_s^\infty \chi_m(z)\psi_n(z)\mathrm{d}z = -\frac{\mathrm{Ai}\left(\frac{s}{z_0}+\mathrm{AiZ}(m)\right)}{\mathrm{Ai}'(\mathrm{AiZ}(m)(\mathrm{AiZ}(n)-\mathrm{AiZ}(m)-s/z_0)}\,.$$
(A.23)

Now finally I will derive a useful identity for integrals of Airy functions. Let's start out with a general second order differential equation

$$\psi'' = g\psi$$
(A.24)

where ψ and g both are functions of z which is suppressed. Using an arbitrary function f (also dependent on z) we now have

$$\psi'f\psi'' = fg\psi'\psi$$
$$\Rightarrow \psi'f\psi'' = \partial_z\left(\psi'f\psi'\right) - \psi''f\psi' - \psi'f'\psi' = fg\psi'\psi$$
$$\Rightarrow \partial_z\left(\psi'f\psi'\right) - \psi'f'\psi' = 2fg\psi'\psi$$
$$= fg\psi'\psi + \partial_z\left(fg\psi\psi\right) - f'g\psi\psi - fg'\psi\psi - fg\psi\psi' = \partial_z\left(fg\psi\psi\right) - f'g\psi\psi - fg'\psi\psi$$
$$\Rightarrow \partial_z\left(\psi'f\psi'\right) - \psi'f'\psi' = \partial_z\left(fg\psi\psi\right) - f'g\psi\psi - fg'\psi\psi$$
$$\Rightarrow \partial_z\left(\psi'f\psi' - \psi'f'\psi\right) + \psi''f'\psi + \psi'f''\psi =$$
$$\partial_z\left(\psi'f\psi' - \psi'f'\psi\right) + g\psi f'\psi + \psi'f''\psi =$$
$$\partial_z\left(\psi'f\psi' - \psi'f'\psi + \psi f''\psi\right) + g\psi f'\psi - \psi f'''\psi - \psi f''\psi' =$$
$$\partial_z\left(fg\psi\psi\right) - f'g\psi\psi - fg'\psi\psi$$
$$\Rightarrow \partial_z\left(2\psi'f\psi' - 2\psi'f'\psi + \psi f''\psi\right) + 2g\psi f'\psi - \psi f'''\psi =$$
$$\partial_z\left(2fg\psi\psi\right) - 2f'g\psi\psi - 2fg'\psi\psi$$
$$\Rightarrow \psi\left(f''' - 4f'g - 2fg'\right)\psi = \partial_z\left(2\psi'f\psi' - 2\psi'f'\psi + \psi f''\psi - 2fg\psi\psi\right)$$
(A.25)

Integrating this equation from one zero z_0 of ψ to another zero z_1 (assuming also all terms involving ψ times some other function vanishes at these points) gives

$$\int_{z_0}^{z_1}\psi\left(f''' - 4f'g - 2fg'\right)\psi = 2\left(\psi'(z_1)f(z_1)\psi'(z_1) - \psi'(z_0)f(z_0)\psi'(z_0)\right)$$
(A.26)

Using the Airy differential equation (A.1) with $g = (z - E)$

$$\int_{z_0}^{z_1} \psi \left(f''' - 4f'(z - E) - 2f \right) \psi = 2 \left(\psi'(z_1)f(z_1)\psi'(z_1) - \psi'(z_0)f(z_0)\psi'(z_0) \right) \tag{A.27}$$

This relation can be used to derive a recursion relation to determine the expectation values of z. Using $f = z^k$ gives

$$\int_{z_0}^{z_1} \psi \left(z^{k-3}k(k-1)(k-2) - 4kz^{k-1}(z - E) - 2z^k \right) \psi \, \mathrm{d}z = 2 \left(\psi'(z_1)z_1^k\psi'(z_1) - \psi'(z_0)z_0^k\psi'(z_0) \right) \tag{A.28}$$

which leads to the simple relation

$$-2\left(2k + 1\right)Z_k + 4kEZ_{k-1} + k(k-1)(k-2)Z_{k-3} = 2 \left(\psi'(z_1)z_1^k\psi'(z_1) - \psi'(z_0)z_0^k\psi'(z_0) \right) \tag{A.29}$$

where $Z_k = \int_{z_0}^{z_1} \psi z^k \psi \, \mathrm{d}z$. Specialising now to ψ as in (A.17), $z_0 = 0$ and $z_1 = \infty$

$$
\begin{aligned}
Z_0 &= \frac{1}{z_0}, \\
Z_1 &= -\frac{2}{3}\frac{\mathrm{AiZ}(n)}{z_0}, \\
Z_2 &= \frac{8}{15}\frac{\mathrm{AiZ}(n)^2}{z_0}, \\
-2\left(2k + 1\right)Z_k &- 4k\mathrm{AiZ}(n)Z_{k-1} + k(k-1)(k-2)Z_{k-3} = 0, \, k > 2,
\end{aligned}
\tag{A.30}
$$

with the first three directly evaluated from (A.28). This recursion relation can be used to determine the higher order expectation values of the height z. This agrees with [23]. For the real location in SI units $\langle z^k \rangle = z_0^{k+1}Z_k$ when reintroducing the characteristic length. This also follows directly from dimensional arguments.

Appendix B

Penetration depth

Here I will consider the effects of a finite penetration depth on the energy levels of the neutron and in particular the shift in energy differences of different states. In the main text it was argued, that if the neutron does not enter the neutron mirror all wave functions have the same slope close to the mirror. In particular any surface effects much smaller than the characteristic length scale of the wavefunction on top of the mirror should not influence the eigenstates hugely differently, with the characteristic length $z_0 \approx 5.9\,\mu\text{m}$. Considering the time independent Schrödinger equation for a neutron on top of the mirror similar to (2.6), where $V(z)$ now includes all potentials.

$$\tilde{E}\psi(z) = \left(-z_0^2 \frac{\partial^2}{\partial z^2} + \frac{V(z)}{E_0}\right)\psi(z)\,, \tag{B.1}$$

where $\tilde{E} = \frac{E}{E_0}$, $z_0 \approx 5.869\,\mu\text{m}$ and $E_0 \approx 0.602\,\text{peV}$. To investigate the effect of a final penetration depth into the mirror the following potential is used

$$V(z) = \begin{cases} \frac{E_0}{z_0}z, z > 0\,, \\ E_0\tilde{V}, z < 0\,, \end{cases} \tag{B.2}$$

where $E_0\tilde{V}$ is the pseudo optical potential of the mirror and $\frac{E_0}{z_0}$ is the force acting on the neutron due to gravity. The wavefunction now follows two equations

$$\begin{aligned} I : \ &\partial_{z'}^2\psi(z') = \left(\tilde{V} - \tilde{E}\right)\psi(z')\,, z' < 0 \\ II : \ &\partial_{z'}^2\psi(z') = \left(z' - \tilde{E}\right)\psi(z')\,, z' > 0 \end{aligned} \tag{B.3}$$

with $z' = z/z_0$ a dimensionless spatial variable as in the main text. The general solution is given by

$$\begin{aligned} I : \ &\psi(z') = a_I e^{(z'/l)} + b_I e^{(-z'/l)}\,, z' < 0 \\ II : \ &\psi(z') = a_{II}\text{Ai}(z' - \tilde{E}) + b_{II}\text{Bi}(z' - \tilde{E})\,, z' > 0 \end{aligned} \tag{B.4}$$

where $l = 1/\sqrt{\tilde{V} - \tilde{E}}$ is the reduced penetration depth in units of z_0 into the mirror and a_I, a_{II}, b_I and b_{II} are general coefficients. Now the wavefunction has to vanish for $z \to \pm\infty$, which requires that $b_I = 0 = b_{II}$, and in addition, for the Schrödinger equation to be valid at all points in space, the equations of continuity $\psi(0^-) = \psi(0^+)$ and $\partial_{z'}\psi(0^-) = \partial_{z'}\psi(0^+)$ have to be satisfied. The shifted energy $\tilde{E}$ has to be chosen such that a_I and a_{II} satisfy

$$\begin{aligned} a_I &= a_{II}\text{Ai}(-\tilde{E})\,, \\ \frac{a_I}{l} &= a_{II}\text{Ai}'(-\tilde{E})\,. \end{aligned} \tag{B.5}$$

Thus

$$\text{Ai}(-\tilde{E}) = l\text{Ai}'(-\tilde{E}) = \frac{\text{Ai}'(-\tilde{E})}{\sqrt{\tilde{V} - \tilde{E}}}\,, \tag{B.6}$$

where it is clear, that if the penetration depth $l \to 0$ the eigenenergies are just the zeroes of the Airy function Ai. This equation has to be solved numerically for a specific l. In the case of qBOUNCE , the neutron mirrors are made of $\approx 3\,\mathrm{cm}$ borosilika glass, which has an optical potential of $V \approx 100\,\mathrm{neV} \approx 1.66 \cdot 10^5 E_0$. In figure 2.5 the penetration depths of the first 10^4 states are shown. In figure 2.4 the energy shift is shown for the first 10^4 states. This absolute shift of the levels in the feV level is not observable, only differences between states. From the plot the relative shift of the transition frequencies is at the 10^{-8} level, so not yet experimentally in reach.

Now to calculate the normalisation constant for the wave function. Thus far the wave function is given by

$$
\begin{aligned}
I &: \psi(z') = a_{II}\mathrm{Ai}(-\tilde{E})e^{(z'/l)} \,, z' < 0 \\
II &: \psi(z') = a_{II}\mathrm{Ai}(z' - \tilde{E}) \,, z' > 0
\end{aligned}
\tag{B.7}
$$

with the requirement

$$
1 = \int_{-\infty}^{\infty} |\psi(z)|^2 \mathrm{d}z = z_0 \int_{-\infty}^{\infty} |\psi(z')|^2 \mathrm{d}z' =
$$
$$
|a_{II}|^2 z_0 \left(\mathrm{Ai}(-\tilde{E})^2 \int_{-\infty}^{0} e^{(2z'/l)} \mathrm{d}z' + \int_{0}^{\infty} \mathrm{Ai}(z' - \tilde{E})^2 \mathrm{d}z' \right) =
\tag{B.8}
$$
$$
|a_{II}|^2 z_0 \left(\mathrm{Ai}(-\tilde{E})^2 \frac{l}{2} + \tilde{E}\mathrm{Ai}'(-\tilde{E})\mathrm{Ai}(\tilde{E}) + \mathrm{Ai}'(\tilde{E})^2 \right) = 1 \,,
$$

where the last equality was obtained by applying equation (A.7) to the shifted $\mathrm{Ai}(z' - \tilde{E})$. With this the normalised wavefunction for the whole space is given by

$$
\psi(z') = \begin{cases}
\dfrac{\mathrm{Ai}(-\tilde{E})}{\sqrt{z_0\left(\mathrm{Ai}(-\tilde{E})^2 \frac{l}{2} + \tilde{E}\mathrm{Ai}'(-\tilde{E})\mathrm{Ai}(\tilde{E}) + \mathrm{Ai}'(\tilde{E})^2\right)}} e^{\frac{z'}{l}} \,, z' < 0 \\[4mm]
\dfrac{\mathrm{Ai}(z' - \tilde{E})}{\sqrt{z_0\left(\mathrm{Ai}(-\tilde{E})^2 \frac{l}{2} + \tilde{E}\mathrm{Ai}'(-\tilde{E})\mathrm{Ai}(\tilde{E}) + \mathrm{Ai}'(\tilde{E})^2\right)}} \,, z' > 0
\end{cases}
\tag{B.9}
$$

or in terms of real spacial and energy variables in SI units

$$
\psi(z) = \begin{cases}
\dfrac{\mathrm{Ai}(-E/E_0)}{\sqrt{z_0\left(\mathrm{Ai}(-E/E_0)^2 \frac{l_0}{2z_0} + E/E_0\mathrm{Ai}'(-E/E_0)\mathrm{Ai}(E/E_0) + \mathrm{Ai}'(E/E_0)^2\right)}} e^{\frac{z}{l_0}} \,, z < 0 \\[4mm]
\dfrac{\mathrm{Ai}(z/z_0 - E/E_0)}{\sqrt{z_0\left(\mathrm{Ai}(-E/E_0)^2 \frac{l_0}{2z_0} + E/E_0\mathrm{Ai}'(-E/E_0)\mathrm{Ai}(E/E_0) + \mathrm{Ai}'(E/E_0)^2\right)}} \,, z > 0
\end{cases}
\tag{B.10}
$$

with $l_0 = z_0 l = z_0\sqrt{E_0/(V-E)}$. As a final remark it is noted that this equation itself is only an approximation. First in order to keep stable states on top of the mirror gravity is not present inside the mirror. This is necessary in order for stable states to exist at all additionally the finite thickness of the neutron mirror was completely ignored. Lifting a neutron by $100\,\mathrm{nm}$ requires an energy of about $100\,\mathrm{feV}$, which is still many orders of magnitude bigger than the shift introduced by the neutron mirrors. It is therefore completely justified to ignore these effects for the time beeing. Considering the resonance states on thin film neutron mirrors from the point of view of scattering theory might be necessary once the thickness of the neutron mirrors gets "small" and the lifetime of the states gets "large" for appropriate values of "small" and "large".

Appendix C

Spin dependent measurements

Here I will give an outline of the measurements performed to characterise the spin dependent detector and the characterisation of the detector foil. The experiment is described in great detail in [37]. The UCNs from the test beam arrive at a chopper, to enable a time of flight measurement, gets polarized by a foil, passes a spin flipper and enters the detector. From [58] this whole process can be described by

$$
\begin{aligned}
r = & \frac{dn}{2} \begin{pmatrix} 1 & 1 \end{pmatrix} \begin{pmatrix} 1+D & 0 \\ 0 & 1-D \end{pmatrix} \begin{pmatrix} 1-F & F \\ F & 1-F \end{pmatrix} \begin{pmatrix} 1+P & 0 \\ 0 & 1-P \end{pmatrix} \begin{pmatrix} 1 \\ 1 \end{pmatrix} \\
= & dn \left(1 + \left(PD \left(1 - 2F \right) \right) \right)
\end{aligned}
\tag{C.1}
$$

where r is the measured rate, P and D are the polarisation efficiency of the polarising foil and the detector respectively, n is the total number of neutrons, d is the detector efficiency and F is the spin flip efficiency of the spin flipper. The quantity D is the efficiency of the neutron detector that is to be characterised.

In particular the velocity range in which this detector can be used to select spins of a specific orientation was determined. To do this a chopper for a time of flight measurement was placed in front of the first polariser and the arrival time was measured. There were two main measurements following eq. C.1, one with no spin flipper, $F = 0$ resulting in the rate $r_\uparrow$ and one with spin flipper on $F > 0$ resulting in $r_\downarrow$. Since this spin flipper is an adiabatic spin flipper and the UCNs are quite slow, the efficiency should be close to 1. The precise value is not known so the result

$$
P_T = \frac{r_\uparrow - r_\downarrow}{r_\uparrow + r_\downarrow} = \frac{DPF}{1 + DP \left(1 - F \right)} \stackrel{DP \geq 0}{\leq} D
\tag{C.2}
$$

represents the lower limit of the spin selection efficiency of the detector. The measurements were performed with two polarisers that were available. The quantity C.2 can be seen in fig. C.1 with the velocity on the x axis. The cutoff velocity can be seen to be around $7.5\,\mathrm{m\,s^{-1}}$ which was used in qBOUNCE for spin dependent measurements. Because of this efficiency measurement the velocity interval in 5.4.2 was set to $v \leq 7.5\,\mathrm{m\,s^{-1}}$.
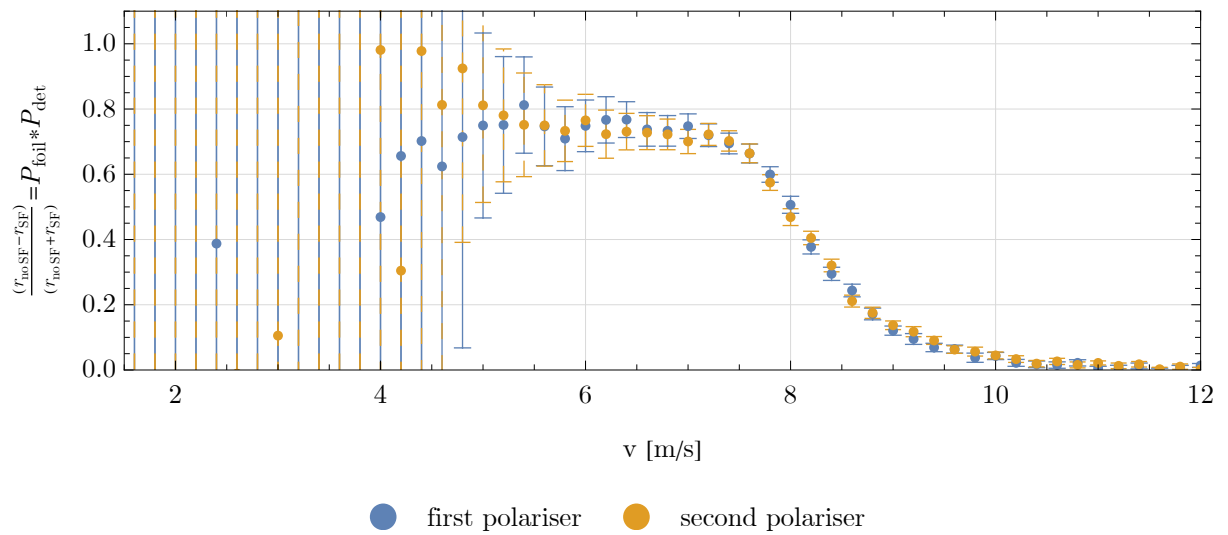
Figure C.1: Measured product of polariser and detector spin polarisation efficiencies. This represents the lower limit of the detector spin polarisation efficiency.

Bibliography

[1] R. Golub, D. Richardson, and S.K. Lamoreaux. *Ultra-Cold Neutrons*. Taylor & Francis, 1991.

[2] A. Steyerl. *Ultracold Neutrons*. World Scientific Publishing Company, 2020.

[3] R. L. Workman et al. Review of Particle Physics. *PTEP*, 2022:083C01, 2022.

[4] Valery V. Nesvizhevsky, Hans G. Börner, Alexander K. Petukhov, Hartmut Abele, Stefan Baeßler, Frank J. Rueß, Thilo Stöferle, Alexander Westphal, Alexei M. Gagarski, Guennady A. Petrov, and Alexander V. Strelkov. Quantum states of neutrons in the earth's gravitational field. *Nature*, 415(6869):297–299, 2002.

[5] Tobias Jenke, Peter Geltenbort, Hartmut Lemmel, and Hartmut Abele. Realization of a gravity-resonance-spectroscopy technique. *Nature Physics*, 7(6):468–472, 2011.

[6] Tobias Jenke. *qBounce - vom Quantum Bouncer zur Gravitationsresonanzspektroskopie*. 2011.

[7] T. Jenke, G. Cronenberg, J. Burgdörfer, L. A. Chizhova, P. Geltenbort, A. N. Ivanov, T. Lauer, T. Lins, S. Rotter, H. Saul, U. Schmidt, and H. Abele. Gravity resonance spectroscopy constrains dark energy and dark matter scenarios. *Phys. Rev. Lett.*, 112:151105, Apr 2014.

[8] Gunther Cronenberg. *Frequency measurements testing Newton's Gravity Law with the Rabi-qBounce experiment*. Wien, 2015.

[9] Gunther Cronenberg, Philippe Brax, Hanno Filter, Peter Geltenbort, Tobias Jenke, Guillaume Pignol, Mario Pitschmann, Martin Thalhammer, and Hartmut Abele. Acoustic rabi oscillations between gravitational quantum states and impact on symmetron dark energy. *Nature Physics*, 14(10):1022–1026, 2018.

[10] Norman F. Ramsey. A molecular beam resonance method with separated oscillating fields. *Phys. Rev.*, 78:695–699, Jun 1950.

[11] H. Abele, T. Jenke, H. Leeb, and J. Schmiedmayer. Ramsey's method of separated oscillating fields and its application to gravitationally induced quantum phase shifts. *Phys. Rev. D*, 81:065019, Mar 2010.

[12] Gunther Cronenberg, K Durstberger-Rennhofer, P Geltenbort, T. Jenke, Hartmut Lemmel, and H Abele. Methods and applications of gravity resonance spectroscopy within the qbounce experiment. *Journal of Physics: Conference Series*, 340, 02 2012.

[13] Tobias Rechberger. *Ramsey spectroscopy of gravitationally bound quantum states of ultracold neutrons*. Wien, 2018.

[14] Sedmik, René I.P., Bosina, Joachim, Achatz, Lukas, Geltenbort, Peter, Heiß, Manuel, Ivanov, Andrey N., Jenke, Tobias, Micko, Jakob, Pitschmann, Mario, Rechberger, Tobias, Schmidt, Patrick, Thalhammer, Martin, and Abele, Hartmut. Proof of principle for ramsey-type gravity resonance spectroscopy with qbounce. *EPJ Web Conf.*, 219:05004, 2019.

[15] Katharina Durstberger-Rennhofer, Tobias Jenke, and Hartmut Abele. Probing the neutron's electric neutrality with ramsey spectroscopy of gravitational quantum states of ultracold neutrons. *Phys. Rev. D*, 84:036004, Aug 2011.

[16] Ludger Timmen. Measurement of g at ill in grenoble [tbp], private communication, October 2021.

[17] Eite Tiesinga, Peter J. Mohr, David B. Newell, and Barry N. Taylor. Codata recommended values of the fundamental physical constants: 2018. *Journal of Physical and Chemical Reference Data*, 50(3):033105, 2021.

[18] A. Westphal, H. Abele, S. Baeßler, V. V. Nesvizhevsky, K. V. Protasov, and A. Y. Voronin. A quantum mechanical description of the experiment on the observation of gravitationally bound states. *The European Physical Journal C*, 51(2):367–375, 2007.

[19] Martin Thalhammer. Diss. tbp. 2021.

[20] L. A. Chizhova, S. Rotter, T. Jenke, G. Cronenberg, P. Geltenbort, G. Wautischer, H. Filter, H. Abele, and J. Burgdörfer. Vectorial velocity filter for ultracold neutrons based on a surface-disordered mirror system. *Phys. Rev. E*, 89:032907, Mar 2014.

[21] Joachim Bosina. *Diss. TBP*. PhD thesis, 2023.

[22] P. Güttinger. Das verhalten von atomen im magnetischen drehfeld. *Zeitschrift für Physik*, 73(3):169–184, 1932.

[23] Guillaume Pignol. *Préparation de l'expérience GRANIT et recherche de nouvelles interactions avec les neutrons*. PhD thesis, 2009. Thèse de doctorat dirigée par Nesvizhevsky, Valery et Protassov, Konstantin Physique des particules Grenoble 1 2009.

[24] Lev Davidovič Landau and Evgenij M Lifšic. *Lehrbuch der theoretischen Physik : 3. Quantenmechanik*. Edition Harri Deutsch. Verlag Europa-Lehrmittel, Haan-Gruiten, unveränderter nachdruck der 9. auflage 1986. edition, 2021.

[25] Jon H. Shirley. Some causes of resonant frequency shifts in atomic beam machines. i. shifts due to other frequencies of excitation. *Journal of Applied Physics*, 34(4):783–788, 1963.

[26] R. F. Code and N. F. Ramsey. Molecular-Beam Magnetic Resonance Studies of HD and D_2. *PRA*, 4(5):1945–1959, November 1971.

[27] P. Bevington and D.K. Robinson. *Data Reduction and Error Analysis for the Physical Sciences*. McGraw-Hill Education, 2003.

[28] ILL. Pf2. https://www.ill.eu/users/instruments/instruments-list/pf2/description/instrument-layout, November 2021. 10:46.

[29] A. Steyerl. A "neutron turbine" as an efficient source of ultracold neutrons. *Nuclear Instruments and Methods*, 125(3):461–469, 1975.

[30] Tobias Jenke. private communication, February 2020.

[31] Carina Killian. *qBounce: systematic analysis of the Ramsey setup*. Wien, 2020.

[32] Veronika Kraus. Systematic testings of the oscillating region's mechanical resonances for the ramsey-qbounce experiment. *Bachelor Thesis*, 2020.

[33] Frederic Thomas. private communication. Technical report, Projects and Calculations Office ILL, November 2022.

[34] Heiko Saul. Weiterentwicklung des detektor- und auslesekonzepts für das gravitationsexperiment qbounce. Master's thesis, TUM, 2011.

[35] Martin Thalhammer. *Optimierung der Detektorsignalverarbeitung des Gravitationsexperiments qBounce.* 2013.

[36] Anselm Balthasar. Minimierung des untergrundes eine sneutronendetektors. *Bachelor Thesis*, 2018.

[37] Hugo Wetter. *Characterisation of the spin-dependent detector for the Ramsey GRS.* Wien, 2022.

[38] Jakob Micko. *q Bounce - gravity resonance and ramsey spectroscopy.* Wien, 2018.

[39] meusburger. Elastomer compression spring, 70 shore a. https://ecom.meusburger.com/files/pdf/e/e1556.pdf, September 2022. 11:05.

[40] meusburger. Elastomer compression spring, 90 shore a. https://ecom.meusburger.com/files/pdf/e/e1558.pdf, September 2022. 11:05.

[41] Physik Instrumente. Piseca capacitive sensors d510. https://www.physikinstrumente.com/fileadmin/user_upload/physik_510-Datasheet.pdf, September 2022. 11:00.

[42] Physik Instrumente. High-precision linear stage for heavy loads hps-170. https://www.physikinstrumente.com/fileadmin/user_upload/physik_instrumente/files/datasheets/HPS-170-Datasheet.pdf, September 2022. 11:00.

[43] Stanford Research Systems. Fs740 - 10mhz gps frequency reference. https://www.thinksrs.com/products/fs740.html, November 2021. 12:25.

[44] Alice Jardel. Study of the mechanical oscillations of a quantum bouncer. Technical report, ILL/phelma, 2017.

[45] Tektronix. Arbitrary/function generators. https://download.tek.com/datasheet/AFG3000_Series_Arbitrary-Function_Generators_Datasheet_76W-18656-5.pdf, November 2022. 11:55.

[46] F. Bloch and A. Siegert. Magnetic resonance for nonrotating fields. *Phys. Rev.*, 57:522–527, Mar 1940.

[47] D. J. R. May. *A high precision comparison of the gyromagnetic ratios of the 199Hg atom and the neutron.* PhD thesis, 1999.

[48] S. Baeßler, V. V. Nesvizhevsky, G. Pignol, K. V. Protasov, D. Rebreyend, E. A. Kupriyanova, and A. Yu. Voronin. Frequency shifts in gravitational resonance spectroscopy. *Phys. Rev. D*, 91:042006, Feb 2015.

[49] René Sedmik. Private communication, 2021.

[50] J. W. T. Dabbs, J. A. Harvey, D. Paya, and H. Horstmann. Gravitational acceleration of free neutrons. *Phys. Rev.*, 139:B756–B760, Aug 1965.

[51] S.A. Werner, H. Kaiser, M. Arif, and R. Clothier. Neutron interference induced by gravity: New results and interpretations. *Physica B+C*, 151(1):22–35, 1988.

[52] G. M. Tino, L. Cacciapuoti, S. Capozziello, G. Lambiase, and F. Sorrentino. Precision gravity tests and the einstein equivalence principle. *Progress in Particle and Nuclear Physics*, 112:103772, 2020.

[53] P. Geltenbort and T. Jenke. private communication. Technical report, ILL, 2021.

[54] Jeeva Anandan and Jun Suzuki. *Quantum Mechanics in a Rotating Frame*, pages 361–370. Springer Netherlands, Dordrecht, 2004.

[55] Ar Rohim, Kazushige Ueda, Kazuhiro Yamamoto, and Shih-Yuin Lin. Relativistic quantum bouncing particles in a homogeneous gravitational field. *International Journal of Modern Physics D*, 30(13), sep 2021.

[56] M. Weber. *Gravitation in interferometry with cold neutrons*. PhD thesis, 1998.

[57] Mario Pitschmann. qbounce working notes, private communication.

[58] Thorsten Soldner. Neutron polarization. In *Fundamental Neutron Physics Summer School*, 2015.